8-2-2017

Enhanced Piezoelectric Performance of Printed PZT Films on Low Temperature Substrates

Jing Ouyang
jxo7115@rit.edu

R·I·T

Enhanced Piezoelectric Performance of Printed PZT Films on Low Temperature Substrates

by

Jing Ouyang

A dissertation submitted in partial fulfillment of the requirements
for the degree of Doctorate of Philosophy in Microsystems Engineering

Microsystems Engineering Program
Kate Gleason College of Engineering

Rochester Institute of Technology
Rochester, New York
August 02, 2017

Enhanced Piezoelectric Performance of Printed PZT Films
on Low Temperature Substrates
by
Jing Ouyang

Committee Approval:

We, the undersigned committee members, certify that we have advised and/or supervised the candidate on the work described in this dissertation. We further certify that we have reviewed the dissertation manuscript and approve it in partial fulfillment of the requirements of the degree of Doctor of Philosophy in Microsystems Engineering.

_____

David A. Borkholder Date
Bausch and Lomb Professor, Microsystems Engineering

_____

Denis R. Cormier Date
Earl W. Brinkman Professor, AMPrint Center Director, Industrial and Systems Engineering

_____

Scott A. Williams Date
Professor, Chemistry and Materials Science

_____

Santosh K. Kurinec Date
Professor, Microelectronic Engineering

Certified by:

_____

Bruce W. Smith Date
Director, Microsystems Engineering Program

ABSTRACT

Kate Gleason College of Engineering
Rochester Institute of Technology

Degree: Doctor of Philosophy **Program**: Microsystems Engineering

Authors Name: Jing Ouyang

Advisors Name: David A. Borkholder

Dissertation Title: Enhanced Piezoelectric Performance of Printed PZT Films on Low Temperature Substrates

Since piezoelectric effect was discovered in 1880, it has been widely used in micro-actuators, sensors, and energy harvesters. Lead Zirconate Titanate (PZT) is a commonly used piezoelectric material due to the high piezoelectric response. The basic PZT film fabrication process includes deposition, sintering, and poling. However, due to the high sintering temperature (> 800 °C) of PZT, only high melting point material can be served as the substrate. Otherwise, complex film transfer approach is needed to achieve flexible and foldable PZT devices. The exploration is accordingly necessary to realize direct fabrication of PZT films on low melting point substrates without affecting the piezoelectric performance. In order to lower the PZT film sintering temperature, in this work, the effect of the powder size and sintering aid on the sintering temperature was studied. A maskless, CAD driven, non-contact direct printing system, aerosol jet printer, was used to deposit PZT thick films on the substrate. This technique allows creating features without masking and etching processes that are generally required for realizing designed features via conventional deposition approaches. Broadband, sub-millisecond, high intensity flash pulses were used to sinter the PZT films. The role of all sintering parameters was investigated to regulate the sintering quality of the PZT thick films. The photonically sintered films showed much lower substrate temperature increase mainly due to the extremely short pulse duration and temperature gradient through the film thickness. The superior piezoelectric property to thermally sintered group was also obtained. This process significantly shortens the processing duration and dramatically expands the possible substrate materials. It accordingly opens the possibility of processing PZT film directly on low melting point materials. A PZT energy harvester based on this process was directly fabricated on the polyethylene terephthalate (PET) substrate to demonstrate the capability. The relation between the load and the generated power was investigated to obtain the highest output power. Up to 0.1 μW was generated from this flexible energy harvester when connected with 10 MΩ resistive load. Photonic sintering of PZT film also creates the opportunity of processing poling during sintering. Different combinations of the sintering and poling techniques were studied. It was observed that the best piezoelectric property was obtained while performing poling during photonic sintering. Consequently, a new method of printing, sintering, and poling of micro-scaled PZT films was demonstrated in this work resulting in high performance films. This process provides the capability of realizing PZT devices on low temperature substrate, facilitates the fabrication of flexible piezoelectric devices, and enhances the piezoelectric property.

ACKNOWLEDGMENTS

I would like to express my sincere gratitude to my adviser, Dr. Borkholder. I would definitely not be where I am today without your guidance and support. Thank you so much for providing the academic expertise, timely advice, and meticulous scrutiny on the research. The skills and knowledges I have learned from our debate, discussion, and brainstorm over these 5 years would certainly help me to overcome many problems I would face in future. I could not have imagined having a better adviser and mentor for my Ph.D. study.

Thank you, Dr. Cormier, the expert of additive manufacturing technique. Thank you for spending time with me at very beginning of this research on exploring the possibility of PZT sintering using photonic approach. Thank you for those suggestions and advices on aerosol jet printing and photonic sintering, without which, my research would be severely lacking and prolonged.

Dr. Williams, I would like to appreciate your support on providing the chemical and material expertise to this research. A lack of chemical background would definitely make this project hardly progress. Besides, thank you for always keeping things light hearted in no matter what kind of situation. This inspires me to make my way through some hard time during research.

I would also like to thank Dr. Kurinec for being my committee member. Thank you for those advices on dielectrics and piezoelectrics. Much of the knowledge I learned on MEMS and microsystems came from the class you taught. You certainly leveraged my love for this field. Thank you!

I thank my lab mates: Dr. Dean Johnson, Dr. Jirachai Getpreechasawas, Dr. Nicholas Conn, Farzad Forouzandeh, Meng-Chun Hsu, and Dr. Ahmed Alfadhel for those stimulating discussions, for those sleepless nights we were working together before deadlines, and for all the fun we have had in the last five years. I thank my fellow students: Anuj Datar, Chaitanya Mahajan, Arjun Wadhwa, Sourav Das, Pritam Poddar, Manoj Meda, Robert Ichiyama, and Khushbo Zope who made working in the Brinkman lab and Amprint Center such a wonderful experience. I would like to thank Dr. Richard Hailstone for the help on SEM, Dr. Surendra Gupta for the help on XRD measurements, Dr. Anju Gupta for the help on powder size distribution measurements, Dr. Mark Irving for the help on the ink formulation discussion, Dr. Bruce Kahn for the help on the required instrumental supporting in Amprint Center.

Last but not the least, I want to thank my parents for the constant support, love and faith. Without you, I would never have chance to do this. Thank you for everything you have done for me. Special thanks to Lanyi for your support and encouragement throughout the whole research period.

CONTENTS

Chapter 1 Introduction to Piezo- and Ferro-electricity ____ 1

1.1. Theory of Piezoelectricity ____ 1

1.1.1. Crystal Structure ____ 1

1.1.2. Elasticity and Dielectricity ____ 3

1.1.3. Piezoelectricity ____ 8

1.2. Theory of Ferroelectricity ____ 10

1.2.1. Perovskite Ferroelectrics ____ 11

1.2.2. Domain and Domain Walls ____ 12

1.2.3. Polarization – Electric Field Hysteresis Loop ____ 14

1.2.4. Several Ferroelectric Materials and Properties ____ 16

1.3. Lead Zirconate Titanate (PZT) ____ 17

1.3.1. Crystal Structure of PZT ____ 17

1.3.2. Dielectric, Elastic and Piezoelectric Properties of PZT ____ 18

1.3.3. Hard and Soft PZT ____ 19

1.4. Overview of the Thesis ____ 20

1.4.1. Literature Review on Piezoelectric Transducers (Chapter 2) ____ 20

1.4.2. Photonic Sintering of Printed PZT Thick Films (Chapter 3) ____ 20

1.4.3. Photonic Sintered Flexible Energy Harvester (Chapter 4) ____ 21

1.4.4. Piezoelectric Properties Manipulation (Chapter 5) ____ 21

Chapter 2 Piezoelectric Transducers ____ 27

2.1. Introduction ____ 27

2.2. Piezoelectric Actuators ____ 28

2.2.1. Cantilever-Shaped Actuators ____ 28

2.2.2. Membrane-Shaped Actuators ____ 32

2.3. Piezoelectric Sensors ____ 34

2.3.1. Pressure sensors 34
2.3.2. Accelerometers 36
2.3.3. Gyroscopes 38
2.3.4. Strain Gauges 39
2.4. Piezoelectric Energy Harvesters 40
2.4.1. d_{31} and d_{33} Modes 40
2.4.2. Flexible Energy Harvesters 42
2.5. Conclusions 44
Chapter 3 Fabrication of PZT Film 51
3.1. Introduction 51
3.2. Established Fabrication Methods 52
3.2.1. PZT Film Deposition 52
3.2.2. PZT Film Sintering 58
3.2.3. PZT Film Poling 61
3.3. Photonic Sintering of Aerosol-Jet Printed PZT Film 63
3.3.1. PZT Ink Preparation 64
3.3.2. Film Sintering 66
3.3.3. Piezoelectric Testing Methods 68
3.3.4. Heat Transfer Simulation 70
3.3.5. Experimental Results and Discussions 73
3.4. Further Enhancement of Piezoelectric Properties via Quality Sintering throughout the Entire Film Thickness 78
3.4.1 PZT Sintering Temperature Reduction 78
3.4.2 Photonic Sintering Optimization 82
3.4.3 Piezoelectric Characterization 84
3.5. Conclusions 86
Chapter 4 Photonically Sintered PZT Flexible Energy Harvester 90
4.1. Introduction 90
4.2. PZT Photonic Sintering on PET Substrate 91
4.3. Flexible Energy Harvester Fabrication 92
4.4. Deforming Stress Simulation 93
4.5. Piezoelectric Experimental Results 95

4.6. Conclusions 97

Chapter 5 Pulsed Flash Manipulation of Piezoelectric Properties of PZT Films 101

5.1. Introduction 101

5.2. Experiment 102

5.3. Results and Discussions 106

5.4. Conclusions 110

Chapter 6 Conclusions and Future Work 112

6.1. Conclusions 112

6.2. Future Opportunity 114

Appendix A Process Description of Aerosol Jet Printer 118

Appendix B Elimination of the Pyrochlore Phase for Photonically Sintered PZT 122

Appendix C Design of Experiment for Fully Sintered PZT Thick Films 125

Appendix D Design of Experiment for Photonic Sintering of PZT Thick Films with ITO Glass 130

LIST OF FIGURES

Figure 1-1. The crystal structure is formed by repetition of the unit cell at every lattice point location. ___*1*

Figure 1-2. The diagram of a parallelepiped shaped lattice cell with six lattice parameters. _____*2*

Figure 1-3. The diagram of normal strain and shear strain. _____*4*

Figure 1-4. The diagram of the stress tensor components on a cubic structure. _____*5*

Figure 1-5. The principle of piezoelectric effect. _____*8*

Figure 1-6. The principle of inverse piezoelectric effect. _____*8*

Figure 1-7. Schematic of elementary cell of perovskite ferroelectrics above and below Curie temperature. _____*11*

Figure 1-8. The paraelectric cubic lattes structure is changing to ferroelectric tetragonal structure due to the movement of the center ion during the temperature reduction through Curie temperature (T_c). _____*12*

Figure 1-9. 180°and 90° domain walls in tetragonal perovskite ferroelectrics. _____*13*

Figure 1-10. The formation mechanisms of 180° (a) and 90° (b) domain walls. _____*13*

Figure 1-11. A typical PE hysteresis loop of a ferroelectric material and corresponded domain transition. _____*15*

Figure 1-12. Sawyer-Tower circuit is designed to experimentally measure P-E hysteresis loop _____*16*

Figure 1-13. Above Curie temperature, PZT is presenting a cubic lattice structure with Pb, Oxygen and Titanium/Zirconium at the corners, face centers and body center of a lattice, respectively. _____*17*

Figure 1-14. (a). Phase diagram of PZT with respect to the mole percentage of $PbTiO_3$. (b). Lattice parameters of PZT below Curie temperature with respect to the mole percentage of $PbTiO_3$. _____*18*

Figure 1-15. Dielectric, elastic and piezoelectric coefficients are highly depending upon the ratio of Zr/Ti. _____*19*

Figure 1-16. (a) Aerosol-Jet printer and (b) PulseForge photonic sintering system. _____*20*

Figure 2-1. Diagram of a unimorph cantilever-shaped actuator. _____*28*

Figure 2-2. Two configurations of the bimorph cantilever-shaped actuator. _____*29*

Figure 2-3. A micromirror with four cantilever-shaped piezoelectric actuator groups. _____*30*

Figure 2-4. SEM image of a single AFM cantilever actuated by piezoelectric material and the morphology measured using this device. _____*30*

Figure 2-5. When the diaphragm is deformed up or down, the fluid is sucked in to or pushed out from the chamber, respectively. This realizes the fluidic pumping function. _____*31*

*Figure 2-6. A cantilever-shaped PZT actuator was built on top of the micropump to deflect the chamber and to realize the fluid flows from inlet to outlet.*_____*31*

Figure 2-7. The diagram of the micropump with a circular shaped piezoelectric actuator. _____*32*

Figure 2-8. Piezoelectric membrane is deflected up and down due to the directional alternation of applied electric field. And this causes fluid sucked in and pumped out through the chamber. _____*32*

*Figure 2-9. Two ink ejection modes used in ink-jet printing technology.*_____*33*

*Figure 2-10. A wave of mechanical deformation with ultrasonic frequency is generated in the piezoelectric material to deform the stator.*_____*33*

Figure 2-11. Diagram of a basic piezoelectric sensing element. _____*35*

Figure 2-12. Diagrams of top and cross-sectional view of the differential pressure flow rate sensor. ____*35*

Figure 2-13. (a) The diagram of a PVDF foil pressure sensor. (b) The output signal was amplified by connecting with an amplifying circuit. _____*36*

Figure 2-14. SEM image of Wong et al designed accelerometer, which is used to measure the acceleration perpendicular to the planar surface of the cantilever. _____*36*

Figure 2-15. (a) The diagram of accelerometer for multi-directional accelerations sensing purpose. (b) The inertia of the mass results from acceleration will lead to deflection occurred in corresponded cantilevers and induces the electric signal. _____*37*

Figure 2-16. Roll, pitch, and yaw are the rotations along X, Y, and Z axis, respectively. _____*38*

Figure 2-17. Simulation results of 3-axis Coriolis Vibrating Micro-Gyros. _____*38*

Figure 2-18. Simulation performed in COMSOL for different device positions. _____*39*

Figure 2-19. A ZnO nanowire piezoelectric surface strain sensor on the PDMS substrate. _____ *39*

Figure 2-20. Two commonly used mode in piezoelectric energy harvesters. _____ *40*

Figure 2-21. A d_{31} piezoelectric cantilever-shaped energy harvester. _____ *41*

Figure 2-22. A d_{33} piezoelectric cantilever-shaped energy harvester. _____ *41*

Figure 2-23. The output voltage and effective power with resistive load of Lee et al. designed (a) d31 and (b) d33 piezoelectric energy harvester. _____ *42*

Figure 2-24. Both substrate and piezoelectric material are required to be flexible to achieve flexible energy harvester. _____ *43*

Figure 2-25. Flexible piezoelectric energy harvesters used for biomedical applications. _____ *44*

Figure 3-1. The procedure of spin coating step. _____ *52*

Figure 3-2. The thickness of a PZT film as a function of the number of spin coated layers on a stainless steel substrate. _____ *52*

Figure 3-3. The diagram of sputtering process. _____ *53*

Figure 3-4. The pulsed laser deposition setup. _____ *54*

Figure 3-5. The diagram of screen printing process. _____ *55*

Figure 3-6. The sintering further dries the film and burns the organic products out. Particles fuse and merge together at high sintering temperature. _____ *58*

Figure 3-7. Piezoelectric coefficient (d_{33}) of a PZT film as a function of the applied poling field in dark and photoinduced poling conditions. _____ *62*

Figure 3-8. X-Ray Diffraction spectrum of the commercially available PZT powders shows peaks characteristic of a highly crystalline perovskite structure. _____ *64*

Figure 3-9. After stirring by a homogenizer, the PZT powders were de-agglomerated to separated particles (a). The inset of (a) is an example of one of five figures used to measure the powder size distribution. PZT particle size distribution was measured after de-agglomeration by a homogenizer (b). Over 70 % of the particles were smaller than 1.5 μm. The largest measured particle size was 3.54 μm. _____ *65*

Figure 3-10. The light intensity spectrum of the Novacentrix bulb generated at 250 V level pulse setting (black), with a peak emission in the violet regime. The dried PZT film light absorbance spectral curve

(blue) has significant overlap with bulb emission, with the greatest absorbance in the ultraviolet (< 400 nm), but significant absorbance at all wavelength levels due to the material thickness (> 30 μm). _____66

Figure 3-11. RC bridge circuit diagram for PZT film capacitance measurement. The bridge can be balanced by adjusting the resistance of R_2. The capacitance of the PZT device (C_X) is equal to the ratio $R_1 \times C_1$ to R_2 _____68

Figure 3-12. The picture (a) and schematic (b) of self-built cylinder system for piezoelectric voltage coefficient (g_{33}) measurement. _____69

Figure 3-13. A signal generator provided a desired input signal to the gas pressure regulator to move the piston and accordingly to apply force to the PZT device. (a) The regulator was at off state when applied signal was zero, and no force was applied on the device ((1) and (3)). The regulator was at on state when the applied signal was at the desired drive voltage with a force was applied to the device (2). (b) The input signal magnitude has a linear relation with the force generated by the cylinder. _____70

Figure 3-14. Device model (zoomed in) used in COMSOL heat transfer simulation. A, B and C are three study points for examining temperature change at the PZT layer, interface of PZT and SS, and position of thermocouple during photonic sintering, respectively. _____70

Figure 3-15. Simulated temperature change at A, B, and C points for all 15 flashes. _____72

Figure 3-16. SEM images of PZT films prior to sintering, after thermal sintering, and after photonic sintering. _____73

Figure 3-17. EDS (Energy-dispersive X-ray spectroscopy) results of unsintered and sintered PZT films. _73

Figure 3-18. EDS of Carbon content of thermally sintered, and photonically sintered films through the film thickness. _____74

Figure 3-19. XRD results for thermally and photonically sintered PZT films. A pyrochlore phase (marked as "Py") was observed in both PZT films due to Pb lost during high temperature sintering. However, in photonically sintered film, this phase was much weaker _____75

Figure 3-20. Low frequency hysteresis loop shows photonically sintered (green) PZT film has superior remanent polarization (32.4 μC/cm2) than the thermally sintered (red) film (17.1 μC/cm2). In both cases, the ferroelectric properties are improved over the unsintered (black) film (0.03 μC/cm2). Applied electric field in the ferroelectric measurement is 20 kV/cm, and frequency is 10 Hz. _____76

Figure 3-21. The particle size distribution of nano-scaled PZT powders. _____ *79*

Figure 3-22. The measured density change with temperature for micro-scaled PZT particles, nano-scaled PZT particles, and nano-scaled PZT particles with sintering aid. _____ *80*

Figure 3-23. The phase equilibrium diagram of the Cu_2O-PbO system. _____ *81*

Figure 3-24. Prior to sintering, the nano-sized particles were uniformly distributed to form a high density PZT film. _____ *82*

Figure 3-25. The SEM images of under-exposed (a), well-exposed (b), and over-exposed (c) films for DOE qualitative investigation. The sintering quality number of 0.2, 0.5, and 0.8, respectively, were given. ____ *82*

Figure 3-26. The light intensity spectrum of the Novacentrix bulb generated at 400 V level pulse setting (black), with a peak emission in the violet regime. The dried PZT film light absorbance spectral curve (blue) has significant overlap with bulb emission, with the greatest absorbance in the ultraviolet (< 400 nm). (Light intensity spectrum of the Novacentrix bulb courtesy from Novacentrix Corporation) _____ *83*

Figure 3-27. Simulated temperature change at the top surface of the PZT film and the film-substrate interface for 2 cycles of flashes. The temperature, after 2 cycles, is sufficiently high to sinter throughout the whole thickness. _____ *84*

Figure 3-28. Cross-sectional view of the well-sintered PZT film. _____ *84*

Figure 3-29. Polarization-electric field hysteresis loop of thermally and photonically sintered nano-scaled PZT powder based film. _____ *85*

Figure 4-1. (a) The SEM image showing that the sintered particles are merged together as observed on the SS substrate. (b) The EDS spectrum shows the photonic sintered PZT film on an Al electrode and PET substrate. _____ *91*

Figure 4-2. Schematic of top and cross-sectional views of the PZT energy harvester. The interdigitated electrode structure results in a poling direction parallel to the PZT surface. _____ *93*

Figure 4-3. Optical image of the fabricated device (without coating PDMS layer). _____ *93*

Figure 4-4. Mechanical finite element simulation results. _____ *94*

Figure 4-5. Photographs of the PZT energy harvester in the flat and bended states. _____ *95*

Figure 4-6. Open-circuit output signal in response to the reciprocated bending-unbending device deformation. Drive frequency was approximately 2.5 Hz. _____ *95*

Figure 4-7. Open-circuit output voltage increases linearly with induced stress in the PZT film. _____96

Figure 4-8. (A) Rectifying circuit used for determination of power delivered to different load resistors. (B) The measured output power delivered to different load resistances ranging from 10 kΩ to 50 MΩ with a peak stress of approximately 145 MPa. The output power is gradually building up with resistance increase. Up to 0.1 μW was generated when the energy harvester was connected to a 10 MΩ load. _____97

Figure 5-1. The light intensity spectrum of the Novacentrix bulb generated at 600 V level pulse setting (black), with a peak emission in the violet regime. The dried PZT film light absorbance spectral curve (blue) has significant overlap with bulb emission, with the greatest absorbance in the ultraviolet (< 400 nm). However, the ITO glass slide has the greatest absorbance in the ultraviolet region. This could affect the effective energy transferred to the PZT film. _____102

Figure 5-2. The setup for photonic sintering the PZT film with poling. The PZT film was sandwiched between top and bottom electrodes. Photonic flashes were transferred through the transparent top ITO glass electrode to create a rapid temperature transient in the film. Simultaneously, the electric field is continuously applied to the sample to reorient the electric dipoles in the PZT film. _____103

Figure 5-3. The COMSOL simulation to estimate the temperature change in the PZT film and substrate during the photonic sintering. The top surface of the PZT film reached ~ 950 °C, which is high enough to sinter the PZT powders. However, the film-substrate interface increased up to ~ 720 °C, which is lower than the required sintering temperature (~ 800 °C). _____106

Figure 5-4. Before and after sintering with electric field poling. An approximately 6 μm thick PZT film was achieved prior to sintering. After the photonic sintering, a well sintered PZT thick film was obtained. Notice the particles size was increased due to the thermal expansion and powders merging. _____107

Figure 6-1. SimPulse modeling result of the temperature change for the simulation of 6 μm PZT film on the 20 μm Kapton substrate under the sintering condition: voltage = 400 V; pulse duration = 650 μs; frequency = 2 Hz; number of pulses = 20. _____116

Figure 6-2. A SimPulse simulation on a μPulse mode setting (a) that results in a (b) up to 29k W/cm^2 power density for each pulse. The temperature change (c) in the PZT film and substrate indicates up to 1010 °C temperature can be generated at the film surface to obtain a well sintered PZT film. On the other hand, the substrate temperature is expected as low as 650 °C. This could melt the substrate slightly to enhance the

film-substrate adhesion without damage it. This setting could allow that the PZT film directly sintered on the low temperature substrate. _____ *117*

Figure A-1. The section view of the pneumatic atomization system to illustrate the working process of atomization. _____ *118*

*Figure A-2. The aerosol jet printed single PZT line. The over-sprayed splatters negatively affect printing resolution.*_____ *119*

Figure A-3. Working principle of virtual impactor. _____ *119*

Figure A-4. The sectional view of the ceramic nozzle during printing. _____ *120*

Figure B-1. XRD results for thermally and photonically sintered PZT films. _____ *123*

Figure B-2. SEM images of PZT films after thermal sintering, and after photonic sintering. _____ *123*

Figure C-1. The main effects plots of the response. _____ *128*

Figure C-2. Residual plots for response. _____ *129*

Figure D-1. The main effects plots of the response. _____ *131*

Figure D-2. Residual plots for response. _____ *132*

LIST OF TABLES

Table 1-1. Seven lattice systems. _____ *2*

Table 1-2. The symbols and characterizations of 32 crystallographic point groups. _____ *3*

Table 1-3. The conversion between s_λ and e_{ik}. _____ *5*

Table 1-4. The conversion between T_λ and σ_{ik}. _____ *5*

Table 1-5. Several commonly used piezoelectric (not ferroelectric) materials and piezoelectric, elastic and dielectric parameters compared with PZT-855. _____ *10*

Table 1-6. Several commonly used ferroelectric materials and piezoelectric, elastic and dielectric parameters compared with PZT-855. _____ *16*

Table 3-1. Deposition methods with the strengths and weaknesses. _____ *56*

Table 3-2. Sintering methods with the strengths and weaknesses. _____ *60*

Table 3-3. PZT ink composition _____ *64*

Table 3-4. Material properties used in the finite element simulation _____ *71*

Table 3-5. The electrical properties of PZT films sintered using different methods _____ *77*

Table 3-6. Low sintering temperature nano-sized PZT powder based ink composition _____ *81*

Table 3-7. The electrical properties of micro-sized and nano-sized particle based PZT films. _____ *86*

Table 4-1. Material parameters used in COMSOL simulation. _____ *94*

Table 5-1. The piezoelectric property of six groups. _____ *110*

Table B-1. Updated PZT ink composition _____ *122*

Table C-1. Factor table and experimental response results for photonic sintering parameter optimization. _____ *126*

Table C-2. ANOVA (analysis of variance) table for all five factors and two-factor interactions. _____ *128*

Table D-1. Factor table and experimental response results for photonic sintering parameter optimization. _____*131*

Table D-2. ANOVA table for all three factors and two-factor interactions. _____*132*

Chapter 1 Introduction to Piezo- and Ferro-electricity

1.1. Theory of Piezoelectricity

Since piezoelectric effect was discovered in 1880 by French physicists Jacques and Pierre Curie, it has been widely used in pressure sensors [1-4], accelerometers [5-8], flow rate sensors [9-11], and energy generators [12-15]. "Piezo" is originated from Greek, which means "push". Piezoelectric effect is the ability that linearly accumulates electric charge in response to mechanical stress. The same material can also be strained when an electric field is applied, which is called inverse piezoelectric effect discovered by Gabriel Lippmann in 1881. In this section, the background of the piezoelectric effect is introduced starting from the basic crystal structure knowledge through elasticity and dielectricity, and to the principle of piezoelectric and inverse piezoelectric effect. Finally, the mathematical expression of piezoelectric effect and several commonly used piezoelectric materials are presented.

1.1.1. Crystal Structure

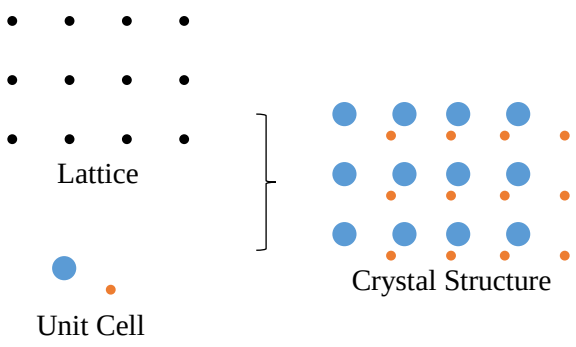

Figure 1-1. The crystal structure is formed by repetition of the unit cell at every lattice point location.

The properties of the piezoelectric materials are strongly depending upon the direction. Significant differences of elastic and dielectric properties can be detected in a piezoelectric material

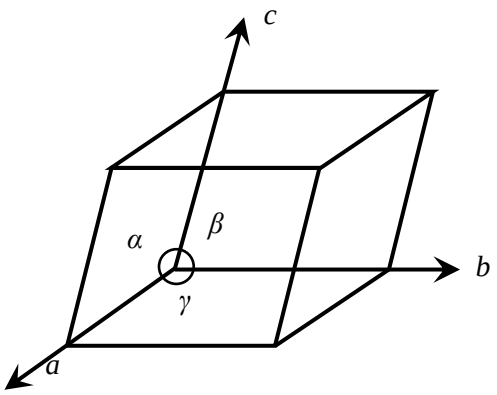

Figure 1-2. The diagram of a parallelepiped shaped lattice cell with six lattice parameters. a, b, and c are three intersected sides and α, β, and γ are three angles formed by three sides.

along different directions. Therefore, introducing the structure and symmetry of the crystal is necessary.

A crystal is constructed by a group of atoms or molecules patterned in an ordered way and repeated three-dimensionally (Fig. 1-1). This basic repetitive atomic group is called unit cell. The repetitive patterns where the unit cell located are the lattice. Generally, for most crystals, three-dimensional primitive lattice cells are parallelepipeds or prisms having three sets of parallel faces. The shape of a lattice can be determined by the length of cell edges (a, b, c) and the angles between them (α, β, γ) as shown in Fig. 1-2 [16]. These six parameters are called lattice parameters. All crystals can be classified into seven lattice systems according to the lattice parameters as listed in Table 1-1.

Table 1-1. Seven lattice systems. Adapted from [17]

Lattice system	Axes	Angles
Cubic	$a = b = c$	$\alpha = \beta = \gamma = 90°$
Rhombohedral	$a = b = c$	$\alpha = \beta = \gamma \neq 90°$
Hexagonal	$a = b \neq c$	$\alpha = \beta = 90°, \gamma = 120°$
Tetragonal	$a = b \neq c$	$\alpha = \beta = \gamma = 90°$
Orthorhombic	$a \neq b \neq c$	$\alpha = \beta = \gamma = 90°$
Monoclinic	$a \neq b \neq c$	$\alpha = \gamma = 90°, \beta \neq 90°$
Triclinic	$a \neq b \neq c$	$\alpha \neq \beta \neq \gamma \neq 90°$

These seven lattice systems are further divided into 32 crystallographic point groups according to the symmetric axis or face as listed in Table 1-2.

Table 1-2. The symbols and characterizations of 32 crystallographic point groups.

Lattice systems	Characterizations of symmetry	Hermann–Mauguin notation
Triclinic	Only 1-fold rotation (or rotoinversion) axes.	1, $\bar{1}$
Monoclinic	2-fold rotation (or rotoinversion) axes that are only along one direction.	2, $\bar{2}$ = m, 2/m
Orthorhombic	2-fold rotation (or rotoinversion) axes that are along three orthogonal directions.	222, mm2, mmm
Rhombohedral	One 3-fold rotation (or rotoinversion) axes.	3, $\bar{3}$, 32, 3m, $\bar{3}$m
Tetragonal	One 4-fold rotation (or rotoinversion) axes.	4, $\bar{4}$, 4/m, 422, 4mm, $\bar{4}$2m, 4/mmm
Hexagonal	One 6-fold rotation (or rotoinversion) axes.	6, $\bar{6}$, 6/m, 622, 6mm, $\bar{6}$m2, 6/mmm
Cubic	Four 3-fold rotation axes.	23, m3, 432, $\bar{4}$3m, m3m

1.1.2. Elasticity and Dielectricity

Piezoelectric property is a coupling of mechanical and dielectric properties. Therefore, it is difficult to understand piezoelectricity without regard to the knowledge of elasticity and dielectricity. Consequently, in order to well investigate piezoelectricity, elasticity and dielectricity are introduced in this section.

1.1.2.1. Elasticity

Elasticity is the capability that a material can recover its original shape after deformed by a small external force when this force is relieved. The piezoelectric material is elastic material and thus has all elastic properties. Several fundamental elastic properties are introduced in this section.

I. Strain

When a solid body is in an equilibrium state under an external force, the ratio of the deformation to the original length is called strain. Strain is a second rank tensor, denoted as e_{ik} ($i, k = x, y, z$).

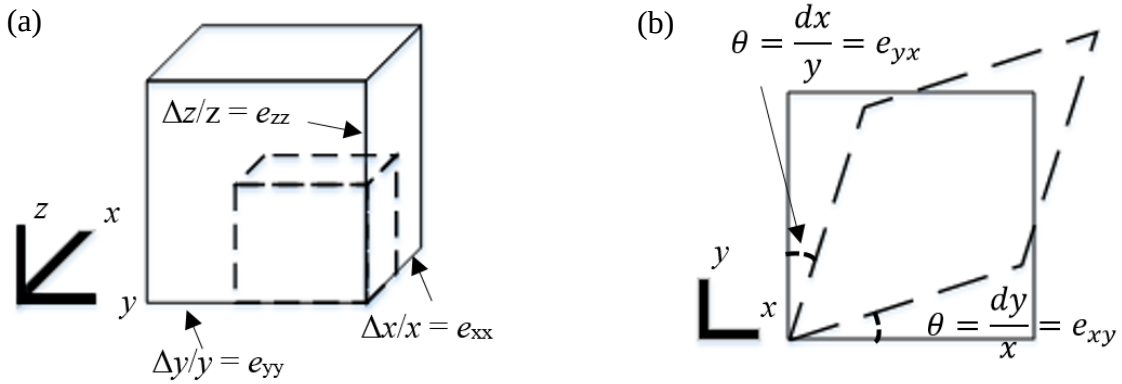

Figure 1-3. The diagram of normal strain (a) and shear strain (b).

For the e_{ik}, the first subscript refers to the axis that is being strained and the second one refers to the direction where it is being strained. Therefore, when $i = k$, e_{ik} represents the normal strain that the side is strained along its own direction (Fig. 1-3 (a)). And the value of the strain is $\Delta i / i$. For $i \neq k$, e_{ik} represents the shear strain that the side along i direction is deformed to k direction as shown in Fig. 1-3 (b) (i.e. angular change between i and k axes). It is clear to see that e_{ik} should equal to e_{ki}. Therefore, strain tensor has only six independent elements, namely e_{xx}, e_{xy}, e_{xz}, e_{yy}, e_{yz}, and e_{zz}. Generally, in order to simplify the two subscripts to only one, the strain tensor is always denoted as a 1×6 matrix using engineering strain notations s_λ ($\lambda = 1, 2, \ldots, 6$). The conversion between s_λ and e_{ik} is shown in Table 1-3.

Table 1-3. The conversion between s_λ and e_{ik}.

s_1	s_2	s_3	s_4	s_5	s_6
e_{xx}	e_{yy}	e_{zz}	$2e_{yz}$	$2e_{zx}$	$2e_{xy}$

II. Stress

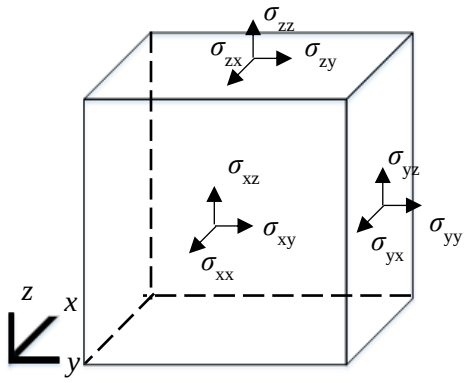

Figure 1-4. The diagram of the stress tensor components on a cubic structure.

The applied external force on the unit area of the forced object is called stress. It is important to note that stress is also a second rank tensor, denoted as σ_{ik} (i, k = x, y, z). As shown in Fig. 1-4, the first subscript (i) represents the plane on which the stress component acts is normal to the i direction; and the second one (k) represents the stress applied direction. The same as strain, σ_{ik} ($i = k$) is the normal stress and σ_{ik} ($i \neq k$) is the shear stress. Since at the equilibrium state, the total moment induced by the inner stresses should equal to zero. Therefore, σ_{ik} should equal to σ_{ki}. Consequently, stress tensor also has only six independent elements. A 1 × 6 matrix is used to represent stress using engineering stress notations T_λ (λ = 1, 2, … , 6). The conversion between T_λ and σ_{ik} is shown in Table 1-4.

Table 1-4. The conversion between T_λ and σ_{ik}.

T_1	T_2	T_3	T_4	T_5	T_6
σ_{xx}	σ_{yy}	σ_{zz}	σ_{yz}	σ_{zx}	σ_{xy}

For a small deformation, strain is a linear function with stress. This is called Hooke's Law. Mathematically, this law can be written as

$$\begin{pmatrix} s_1 \\ s_2 \\ s_3 \\ s_4 \\ s_5 \\ s_6 \end{pmatrix} = \begin{pmatrix} S_{11} & S_{21} & S_{31} & S_{41} & S_{51} & S_{61} \\ S_{12} & S_{22} & S_{32} & S_{42} & S_{52} & S_{62} \\ S_{13} & S_{23} & S_{33} & S_{43} & S_{53} & S_{63} \\ S_{14} & S_{24} & S_{34} & S_{44} & S_{54} & S_{64} \\ S_{15} & S_{25} & S_{35} & S_{45} & S_{55} & S_{65} \\ S_{16} & S_{26} & S_{36} & S_{46} & S_{56} & S_{66} \end{pmatrix} \begin{pmatrix} T_1 \\ T_2 \\ T_3 \\ T_4 \\ T_5 \\ T_6 \end{pmatrix} \quad (1\text{-}1)$$

where **S** is called elastic compliance matrix. Or it can be rewritten as

$$\begin{pmatrix} T_1 \\ T_2 \\ T_3 \\ T_4 \\ T_5 \\ T_6 \end{pmatrix} = \begin{pmatrix} c_{11} & c_{21} & c_{31} & c_{41} & c_{51} & c_{61} \\ c_{12} & c_{22} & c_{32} & c_{42} & c_{52} & c_{62} \\ c_{13} & c_{23} & c_{33} & c_{43} & c_{53} & c_{63} \\ c_{14} & c_{24} & c_{34} & c_{44} & c_{54} & c_{64} \\ c_{15} & c_{25} & c_{35} & c_{45} & c_{55} & c_{65} \\ c_{16} & c_{26} & c_{36} & c_{46} & c_{56} & c_{66} \end{pmatrix} \begin{pmatrix} s_1 \\ s_2 \\ s_3 \\ s_4 \\ s_5 \\ s_6 \end{pmatrix} \quad (1\text{-}2)$$

where **c** is called elastic stiffness matrix. Easily to find that the inverse of **S** is **c** (i.e. $\mathbf{S} = \mathbf{c}^{-1}$).

Both compliance and stiffness matrices are symmetric. So there are 21 independent compliance and stiffness elements, respectively. Notice that piezoelectric materials are all anisotropic material. So considering all 21 elements in the matrices is necessary.

1.1.2.2. Dielectricity

A dielectric material is an electric insulating material or a poor electric conductor. During the application of the electric field, the positive and negative charges are displaced minutely to generate an intrinsic field balancing the applied field. Therefore, the induced charges separation causes dielectric polarization that lead to the energy storage capability. [16]. All piezoelectric materials are dielectrics. An important parameter of dielectric material is dielectric constant (or permittivity), which is reflecting the polarization in the material in response to the external electric field. The higher dielectric constant results in higher polarization in the material under given electric field.

In order to understand the relation among polarization, electric field and dielectric constant, three vectors and two coefficients have to be introduced, namely polarization (P), electric field (E), electric displacement (D), electric susceptibility (χ), and dielectric constant (ε). Since all piezoelectric materials are anisotropic, these five parameters are highly dependent upon the direction.

It is discovered that the polarization along one direction will be influenced by electric field from all three directions, and the relation is as following

$$\begin{bmatrix} \mathrm{P}_1 \\ \mathrm{P}_2 \\ \mathrm{P}_3 \end{bmatrix} = \begin{bmatrix} \chi_{11} & \chi_{12} & \chi_{13} \\ \chi_{21} & \chi_{22} & \chi_{23} \\ \chi_{31} & \chi_{32} & \chi_{33} \end{bmatrix} \begin{bmatrix} \mathrm{E}_1 \\ \mathrm{E}_2 \\ \mathrm{E}_3 \end{bmatrix} \quad (1\text{-}3)$$

where the subscript of 1, 2, and 3 in P and E are representing the components along x, y and z axis, respectively. Moreover, the electric susceptibility matrix is symmetric, i.e. $\chi_{12} = \chi_{21}$, $\chi_{13} = \chi_{31}$, $\chi_{23} = \chi_{32}$. Therefore, at most, there are only six independent components in

the matrix. But depending on the structure of the crystals and crystallographic point groups, the number of independent components may reduce. For instance, for 4mm group (Hermann-Mauguin notation), there are only two independent susceptibility matrix components.

The electric displacement is also linearly proportional to the electric field.

$$\begin{bmatrix} D_1 \\ D_2 \\ D_3 \end{bmatrix} = \begin{bmatrix} \varepsilon_{11} & \varepsilon_{12} & \varepsilon_{13} \\ \varepsilon_{21} & \varepsilon_{22} & \varepsilon_{23} \\ \varepsilon_{31} & \varepsilon_{32} & \varepsilon_{33} \end{bmatrix} \begin{bmatrix} E_1 \\ E_2 \\ E_3 \end{bmatrix} \tag{1-4}$$

This relation can also be written as

$$\begin{bmatrix} D_1 \\ D_2 \\ D_3 \end{bmatrix} = \varepsilon_0 \begin{bmatrix} E_1 \\ E_2 \\ E_3 \end{bmatrix} + \begin{bmatrix} P_1 \\ P_2 \\ P_3 \end{bmatrix} \tag{1-5}$$

where ε_0 is electric permittivity of free space (8.854×10^{-12} F/m). By combining Eq. 1-3 ~ 1-5, the relation between electric susceptibility and dielectric constant is able to be obtained:

$$\begin{bmatrix} \varepsilon_{11} & \varepsilon_{12} & \varepsilon_{13} \\ \varepsilon_{21} & \varepsilon_{22} & \varepsilon_{23} \\ \varepsilon_{31} & \varepsilon_{32} & \varepsilon_{33} \end{bmatrix} = \begin{bmatrix} \varepsilon_0 + \chi_{11} & \chi_{12} & \chi_{13} \\ \chi_{21} & \varepsilon_0 + \chi_{22} & \chi_{23} \\ \chi_{31} & \chi_{32} & \varepsilon_0 + \chi_{33} \end{bmatrix} \tag{1-6}$$

It is important to note that, usually, in order to simplify the calculation, relative permittivity ($\varepsilon_{r\text{-}ij}$, i, j=1, 2, 3) which can be obtained by dividing the dielectric constant by permittivity of free space is used in the research.

The same as the electric susceptibility, the dielectric constant matrix is symmetric and has no more than six independent components. Depending upon the crystallographic point group, the number of independent components can be reduced.

1.1.3. Piezoelectricity

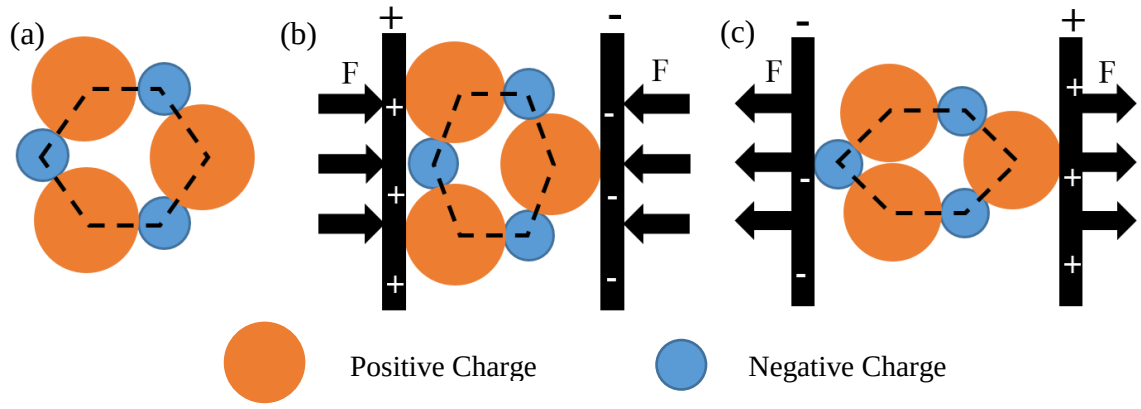

Figure 1-5. The principle of piezoelectric effect. The crystal is in the electrical equilibrium state when no external force applied to it (a). However, due to the compression (b) or tension (c), the centers of positive and negative charges are not coinciding. Therefore, positive and negative charges appear and accumulate on opposite outer surface of the crystal.

In the piezoelectric crystal, at the equilibrium state, it is electrically neutral. Therefore, the positive and negative charges are balanced. However, the atoms are not centrally symmetric (Fig. 1-5 (a)). So when the external force is applied to the material, the crystal deformation pulls some atoms closer and pushes some away. The centers of the positive and negative charge are not coincident anymore giving rise to the positive and negative charges appear on opposite outer surface of the crystal (Fig. 1-5 (b) and (c)). This is so-called direct piezoelectric effect.

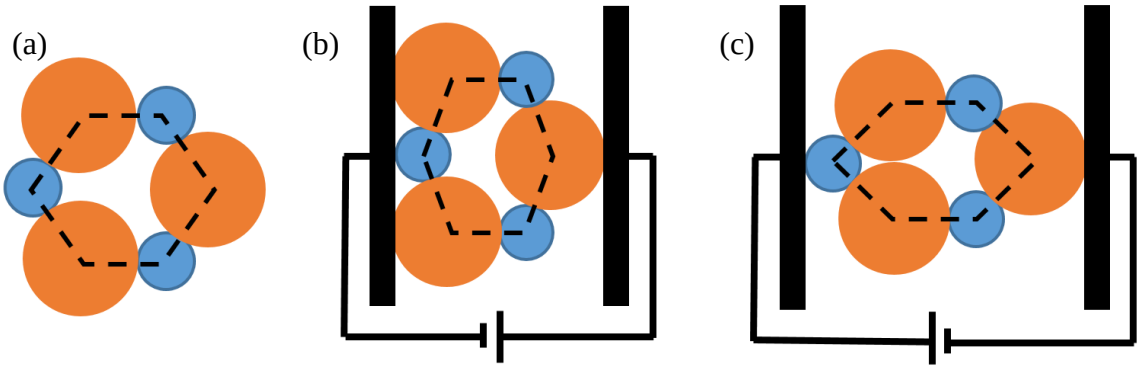

Figure 1-6. The principle of inverse piezoelectric effect. The crystal is in the electrical equilibrium state when no external electric field applied (a). As the electric field applied, in order to balance this field, the centers of positive and negative charges are forced to move oppositely to generate intrinsic electric field. These two fields are cancelled each other to rebalance the crystal. Therefore, due to the motion of positive and negative charges, the crystal is deformed (b and c).

For the inverse piezoelectric effect, when the external electric field is applied to the material. In order to reach the lowest free energy state, the crystal has to reorient the positive and negative charges to generate an intrinsic field for balancing the external electric field. Therefore, the material is deformed due to the reorientation of the crystals (Fig. 1-6).

The piezoelectric effect (or inverse piezoelectric effect) is a coupling of elastics and dielectrics, which is the capability of linearly accumulate electric charge in response to mechanical stress (or deformation in response to the applied electric field). Two piezoelectric constants, $\boldsymbol{g_{ij}}$ and $\boldsymbol{d_{ij}}$, are necessary to be introduced to mathematically express the piezoelectric and inverse piezoelectric effects, respectively. $\boldsymbol{g_{ij}}$ is the 3×6 piezoelectric voltage constant matrix with the unit of V-m/N. The expression is shown as Eq. 1-7.

$$g_{ij} = E_j / T_i \tag{1-7}$$

For those piezoelectric sensors and energy harvesters that require great output electric signal, high $\boldsymbol{g_{ij}}$ value is needed. On the other hand, for those piezoelectric actuators that require large deformation, high $\boldsymbol{d_{ij}}$ value is needed. $\boldsymbol{d_{ij}}$ is the 3×6 piezoelectric charge constant matrix with the unit of m/V, which is expressed mathematically as Eq. 1-8.

$$d_{ij} = S_j / E_i \tag{1-8}$$

Generally, for both piezoelectric constants, axis 3 is always assigned to the direction of the initial polarization of the piezoelectric material (or called poling direction). The relation between piezoelectric voltage and charge constants is shown as Eq. 1-9.

$$d_{ij} = \varepsilon_{ii} g_{ij} \tag{1-9}$$

The properties of the piezoelectric materials are anisotropic. Several commonly used piezoelectric materials with the elastic, dielectric and piezoelectric parameters are listed in the Table 1-5. PZT-855, the ferroelectric material used in this work, is also listed in the table and compared with these piezoelectric materials. In the industry or research, for some specific applications, to obtain the highest piezoelectric coefficient for a better performance, specific poling, stress, and signal collection directions need to be well considered and chosen. For instance, according to Table 1-5, in order to obtain high output electric power for the given stress level, an α-Quartz piezoelectric energy harvester should be built along the d_{11} (or g_{11}) direction (applied pressure direction is the same as induced polarization direction which is perpendicular to the poling direction) rather than the d_{14} (or g_{14}) direction

(induced polarization is along the direction perpendicular to poling direction, while applied stress is a shear stress).

Table 1-5. Several commonly used piezoelectric (not ferroelectric) materials and piezoelectric, elastic and dielectric parameters compared with PZT-855.

		α-Quartz	ZnO	$Li_2B_4O_7$	$Bi_{12}GeO_{20}$	PZT-855
Parameters	Unit					
Point group		32	6mm	4mm	23	4mm & 3m
ε_{r11}	-	4.5	9.26	8.9	38.63	2778
ε_{r22}	-	4.5	9.26	8.9	38.63	2778
ε_{r33}	-	4.6	11.0	8.07	38.63	3170
d_{11}	pC/N	2.31	-	-	-	-
d_{14}	pC/N	0.73	-	-	40.5	-
d_{31}	pC/N	-	-5.2	-1.84	-	-265
d_{33}	pC/N	-	10.6	8.76	-	515
c_{11}	GPa	85.1	210	135	128	113
c_{22}	GPa	85.1	210	135	128	113
c_{33}	GPa	105.4	229	56.8	128	98.9
c_{44}	GPa	57.1	42.5	58.5	25.5	20.1
c_{55}	GPa	57.1	42.5	58.5	25.5	20.1
c_{66}	GPa	39.1	44.3	46.7	25.5	23.0
References		[18-20]	[19, 21]	[22, 23]	[25, 26]	[27]

1.2. Theory of Ferroelectricity

Ferroelectricity was first discovered in 1920 in Rochelle salt by J. Valasek. It is a property that the material exhibits spontaneous electric polarization in the absence of an electric field. This polarization can be reversed by the application of an external electric field [28]. Because of the existence of spontaneous electric polarization, the ferroelectric material is able to generate electric energy when applied mechanical deflection, which is the piezoelectric effect. Therefore, all ferroelectric materials are piezoelectric materials. However, not all piezoelectric materials are ferroelectric materials, because several piezoelectric materials have no spontaneous polarization (e.g. quartz).

It is important to note that the ferroelectric property exists only at the temperature that is lower than a critical value, which is called Curie temperature (T_C). The increasing number of ferroelectric materials, such as Lead Zirconate Titanate ($Pb(Zr_xTi_{1-x})O_3$) [29-32], Barium Titanate ($BaTiO_3$) [33-36], and Polyvinylidene fluoride (PVDF) [37-39], are used in various commercial and research applications. In this section, ferroelectricity is introduced in detail by taking perovskite ferroelectrics as the example. The perovskite

structure and phase transition is presented. The background of polarization, domain and domain walls is also shown. The hysteresis loop that is a commonly used tool for understanding ferroelectric materials is introduced. Finally, some popularly and commonly used ferroelectric materials are presented with the elastic, dielectric and piezoelectric parameters.

1.2.1. Perovskite Ferroelectrics

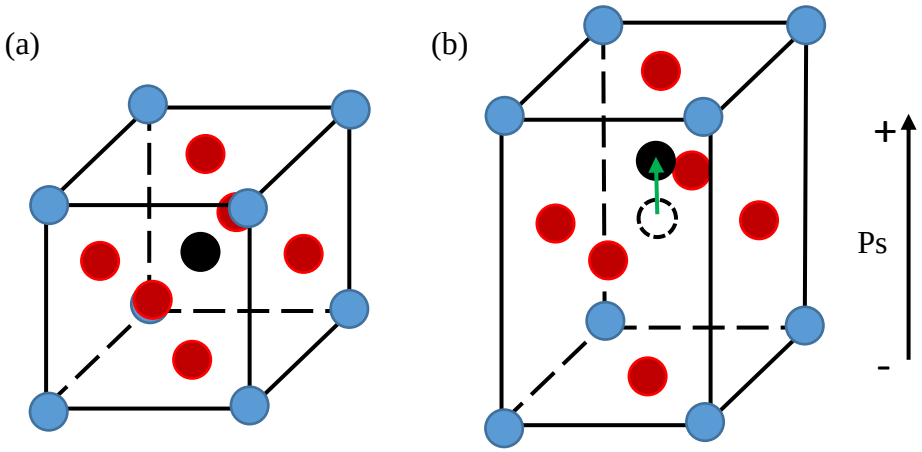

Figure 1-7. Schematic of elementary cell of perovskite ferroelectrics above (a) and below (b) Curie temperature. Above Curie temperature, the cell is in cubic lattice structure. While the temperature reduced to below Curie temperature, it reveals a tetragonal (or sometimes rhombohedral) lattice structure. The blue, red and black circles are representing A, O and B atoms of the general perovskite formula, respectively. Adapted from [41]

A ferroelectric material that has the perovskite crystal structure is called perovskite ferroelectrics. The perovskite ferroelectrics have a "pseudo-cubic" structure with general formula ABO_3. The valence of the A cation can be +1, +2 or +3 (such as Bi, Sr, or Pb). The valence of the B cation ranges from +3 to +5 (such as Ti, Zr, or Ta) [40]. The structure of perovskite ferroelectrics is centrosymmetric cubic while the temperature is above Curie temperature (T_c) (Fig. 1-7 (a)) with coinciding centers of the positive and negative charges and, accordingly, canceled each other out revealing no polarization. This phase is called paraelectric phase. However, when the temperature is reduced below T_C, the central ion in the unit lattice displaces forming a tetragonal structure. This causes the center of the positive and negative charge no longer being coinciding giving rise to spontaneous polarization. It is important to mention that the moving direction of the central ion can be a negative or positive direction of either one of the 2-fold, 3-fold and 4-fold axes of the

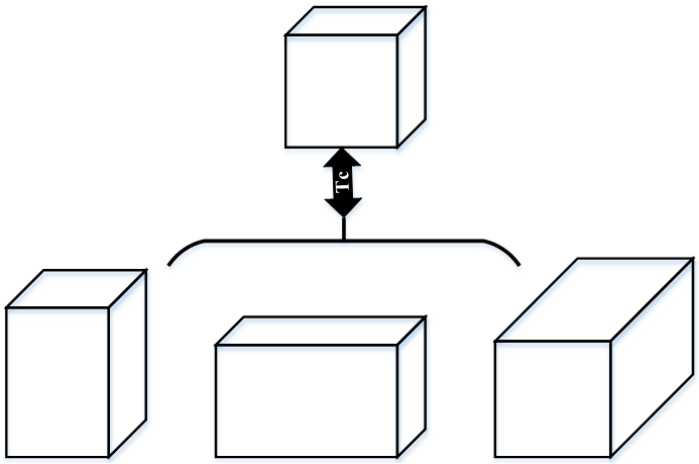

Figure 1-8. The paraelectric cubic lattes structure is changing to ferroelectric tetragonal structure due to the movement of the center ion during the temperature reduction through Curie temperature (T_c). The moving direction of the center ion could be either one of the 2-fold, 3-fold, and 4-fold axes. (a), (b) and (c) are showing three possibilities that the center ion moving along 4-fold axes positive direction to form 3 different directed spontaneous polarizations.

lattice. In the perovskite ferroelectrics, one unit lattice has six 2-fold axes, four 3-fold axes, and three 4-fold axes. So there are 26 possibilities of the polarization direction when temperature reducing to below T_C. Figure 1-8 is showing the formation of three direction possibilities of the spontaneous polarization (P_s) that the center ion moving along the positive direction of 4-fold axes during temperature reduction through the T_c.

1.2.2. Domain and Domain Walls

The ferroelectric domain is the region where polarizations have the same direction. The region that separates different domains is called domain wall. 180° and 90° walls are two most common walls. The domain wall, which separates domains with oppositely directed spontaneous polarizations, is called 180° wall as shown in Fig. 1-9 (a) and that which separates domains with mutually perpendicular polarization is called 90° wall as presented in Fig. 1-9 (b). However, because the relation of side lengths of a tetragonal structure is $a = b \neq c$ as shown in Table 1-1. The angle between two sides of 90° wall is slightly smaller than 90°. Additionally, other walls are also found in some ferroelectric materials, such as 60°, 120°, 71°, and 109° walls. For instance, in $BaTiO_3$ crystal, all aforementioned six domain walls are existing [42].

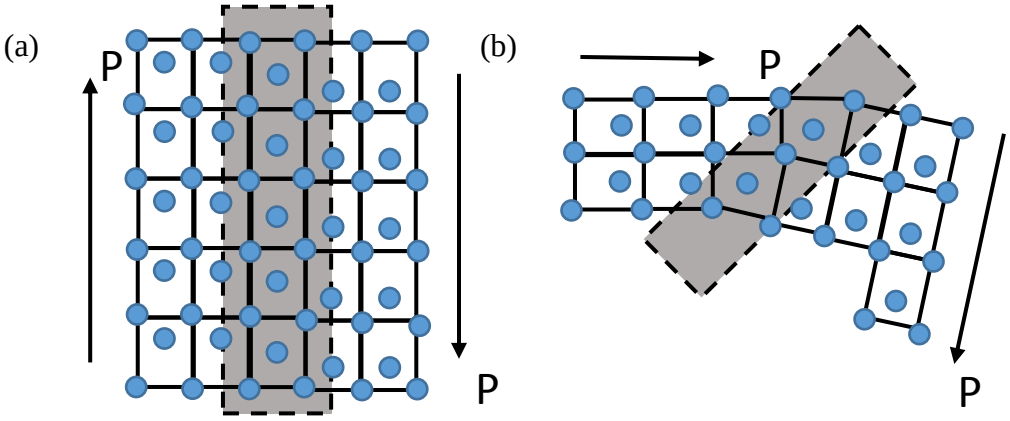

Figure 1-9. 180°and 90° domain walls in tetragonal perovskite ferroelectrics. The 180° wall is to separate the domains with oppositely directed spontaneous polarizations (a) and the 90° wall is to separate the domains with mutually perpendicular polarizations (b). After [41]

The formation of domain walls is to minimize the free energy in the crystal [43]. Two reasons lead to energy increasing in the material during phase change while temperature reduction. One is the motion of the center ion [41, 43, 44]. The onset of the center ion motion leads to the formation of spontaneous polarization (P_s). And this polarization produces surface charge, which forms an electric field (E_d) orienting oppositely to the P_s, as shown in Fig. 1-10 (a). In order to minimize this energy associated with this field to reach the equilibrium state, this domain will be split into two domains with oppositely polarized orientation. Therefore, the two field induced by polarizations are balanced. And

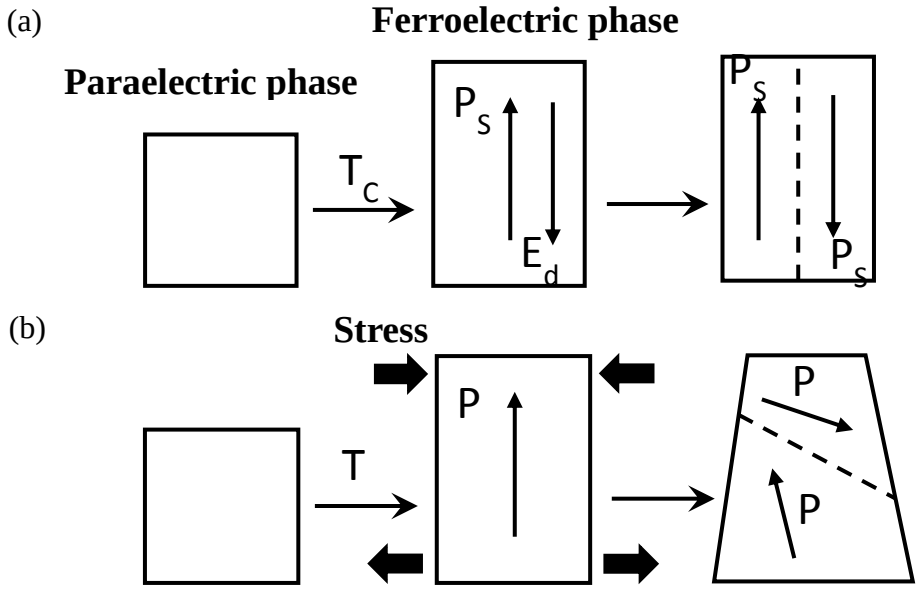

Figure 1-10. The formation mechanisms of 180° (a) and 90° (b) domain walls. TC, PS and Ed are presenting Curie temperature, spontaneous polarization and electric field. Adapted from [41]

a 180° wall is formed. Another reason is mechanical stress applied externally or generated during the temperature reduction [40, 43, 45]. As shown in Fig.1-10 (b), when a stress is applying to a crystal, the longer side of the crystal would be developed along the stress applied direction. However, the shorter side would remain parallel to the stress direction. This may separate the domain into two domains and form 90° wall. And the domain wall is the bisector plane at 45° with respect to the original longer side, because along this plane (also known as an invariant plane) the difference between the stresses of the adjacent domains is zero, which minimizes the elastic energy.

1.2.3. Polarization – Electric Field Hysteresis Loop

The polarization-electric field (PE) hysteresis loop is a simple and effective tool to understand the ferroelectric properties of the material. The occurrence of the hysteresis loop is because of the reorientation of the domain walls in response to the external electric field. Figure 1-11 is a typical ferroelectric hysteresis loop [46]. When no electric field is applied to the ferroelectric material, the directions of the domains are randomly distributed to lead to zero net polarization to reach the minima energy (point O). As the electric field strength increasing, new domains that are aligned to the electric field are nucleating and growing due to the domain wall motion and reorientation in response to the electric field. And in this period, the polarization linearly increases with the electric field (segment OA). With the field keeping increasing, the polarization is saturated and the ferroelectric material turns to single domain structure (all domains are aligning with the electric field direction) (point B). Then even the field further increases, the polarization could not increase due to the saturation. At this point, if the field starts to decrease, some of the domains will back-switch to make the macroscopic polarization reduce (segment BD). However, at the zero filed, the polarization is not zero leading to the remanent polarization (P_r, point D). In order to obtain zero polarization state, increasing the opposite field strength is required (segment DF). The field strength that zeros the polarization is called coercive field (E_c) (Point F). Further increase of the field in the negative direction will cause a new group of aligned polarizations. Similar reorientation of domains and saturation can be observed in the negative field region (segment FG). The spontaneous polarization can be estimated by intercepting the polarization axis with the extrapolated linear segment CB as shown in Fig. 1-11 (point E). In reality, the shape of the PE hysteresis loop may be affected by many

factors, such as mechanical stress, temperature, measuring frequency, and ferroelectrics fabrication process [41, 46].

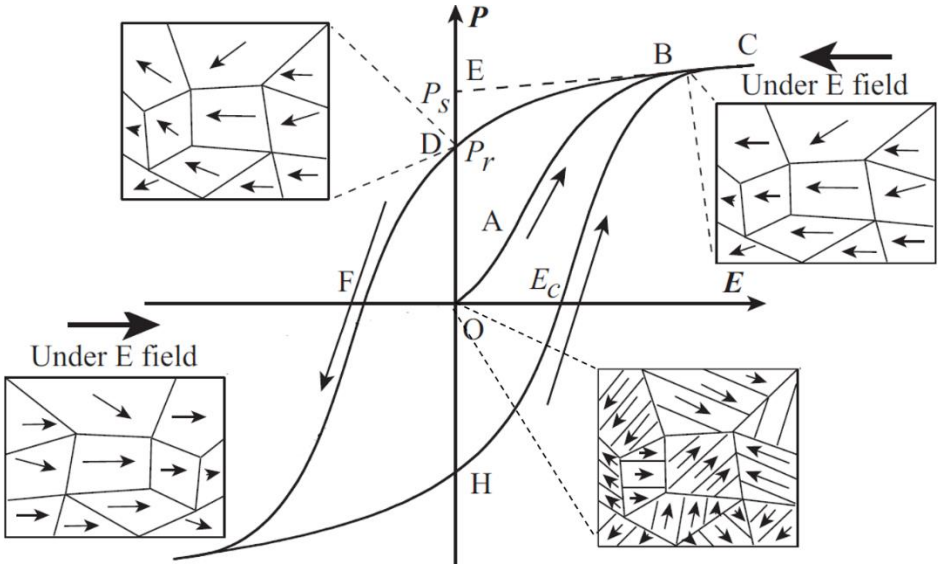

Figure 1-11. A typical PE hysteresis loop of a ferroelectric material and corresponded domain transition. Adapted from [46]

The hysteresis loop can be experimentally measured by a Sawyer-Tower circuit [47] as shown in Fig. 1-12. The capacitance of the reference capacitor has to be much higher than the capacitance of the ferroelectric material [46, 48]. Therefore, most of the voltage can lie over the ferroelectric material. The charge on the capacitor should equal to the charge over the ferroelectric material as they are in series connection. The polarization (P) over the ferroelectrics can be calculated by Eq. 1-10.

$$P = \frac{CV_c}{A} \tag{1-10}$$

where C is the capacitance of the reference capacitor; V_c is the measured voltage over the capacitor; A is the cross-sectional area that charges passing the ferroelectric material through. The electric field (E) over ferroelectrics can be obtained via Eq. 1-11.

$$E = \frac{V - V_c}{t} \tag{1-11}$$

where V is the source voltage of the circuit; t represents thickness of the ferroelectrics.

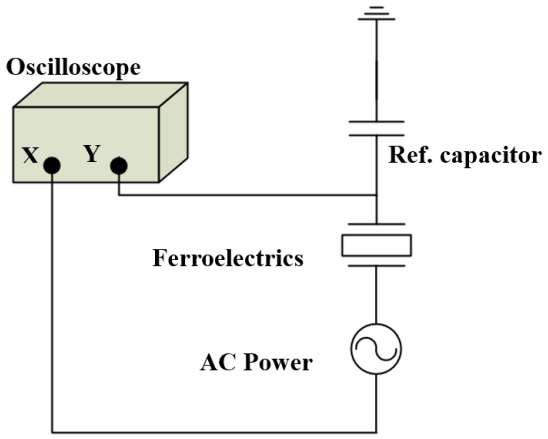

Figure 1-12. Sawyer-Tower circuit is designed to experimentally measure P-E hysteresis loop.

1.2.4. Several Ferroelectric Materials and Properties

Because of the existence of spontaneous polarization, piezoelectric coefficients of ferroelectric materials are generally higher than non-ferroelectric piezoelectric materials. Several commonly used ferroelectrics are listed in the Table 1-6 with their elastic, dielectric and piezoelectric parameters compared with PZT-855, which is the material used in this work. However, because of the crystal symmetry, large properties difference can be found in the materials along different directions.

Table 1-6. Several commonly used ferroelectric materials and piezoelectric, elastic and dielectric parameters compared with PZT-855.

		RS*	$BaTiO_3$	PVDF	$LiTaO_3$	PZT-855
Parameters	Unit					
Point group		2	4mm	4mm	3m	4mm & 3m
ε_{r11}	-	350	1621.9	7.35	40.9	2778
ε_{r22}	-		1621.9	9.27	40.9	2778
ε_{r33}	-		1897.4	7.75	42.3	3170
d_{14}	pC/N	233	-	-	-	-
d_{31}	pC/N	-	-79	20	-2	-265
d_{33}	pC/N	-	191	-20	8	515
c_{11}	GPa	27.5	166	3.61	232.8	113
c_{22}	GPa	42.3	166	3.13	232.8	113
c_{33}	GPa	37.5	162	1.63	275.9	98.9
c_{44}	GPa	7.8	42.9	0.55	94.9	20.1
c_{55}	GPa		42.9	0.59	93.2	20.1
c_{66}	GPa		44.8	0.69	93.2	23.0
Reference		[49, 50]	[51, 52]	[53, 54]	[22, 55]	[27]

* RS stands for Rochelle Salt (i.e. $NaKC_4H_4O_6 \cdot 4H_2O$). RS has two Curie points (24 °C and -18 °C) [56]. Between these two points, RS presents ferroelectric property. However, if temperature is out of this range, RS reveals only general piezoelectric properties (no spontaneous polarization). In this table, only show the ferroelectric properties of RS.

1.3. Lead Zirconate Titanate (PZT)

Lead zirconate titanate ($Pb(Zr_xTi_{1-x})O_3$) is a recently dominant ferroelectric ceramic material with a perovskite structure. In the 1950s, PZT was found to have strong piezoelectric effects by Jaffe et al. Besides high electric response, PZT has high Curie temperature (T_C), which creates more opportunities for high temperature applications. In this section, the crystal structure, elastic, dielectric and piezoelectric properties, and dopants of PZT are introduced.

1.3.1. Crystal Structure of PZT

Microscopically, below the T_C, PZT shows a perovskite structure with the B site occupied by either Zr or Ti and A site situated by Pb as shown in Fig. 1-13. And this perovskite structure is independent of Zr/Ti ratio.

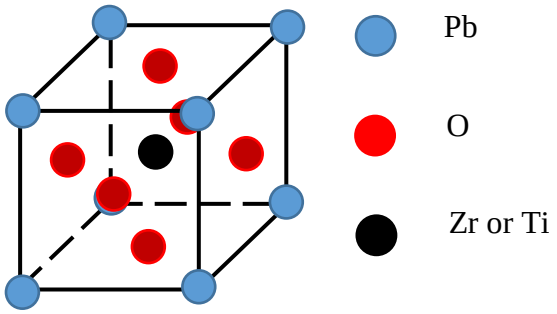

Figure 1-13. Above Curie temperature, PZT is presenting a cubic lattice structure with Pb, Oxygen and Titanium/Zirconium at the corners, face centers and body center of a lattice, respectively.

However, the lattice structure of PZT is strongly depending upon the value of x in the PZT formula, which reveals the ratio of Zr and Ti, when the temperature reduced to below Curie temperature with phase change (paraelectric to ferroelectric). Considering two extreme cases, when x is zero, the material is ferroelectric material $PbTiO_3$ with the tetragonal lattice structure while it turns to anti-ferroelectrics $PbZrO_3$ with the orthorhombic lattice structure if $x = 1$. PZT are falling in between these two cases. Figure 1-14 (a) is showing the temperature-composition phase diagram of PZT [57]. In the diagram, F represents the ferroelectric phase; A represents the anti-ferroelectric phase; and P represents the paraelectric phase. The subscript C, R, T, and O refer to cubic, rhombohedral, tetragonal, and orthorhombic lattice structures, respectively. PZT reveals different point groups of rhombohedral lattice structure at different temperature levels when Zirconium has a higher ratio. Under low temperature (LT), PZT presents 3m point group; while it shows 3 point group under high temperature

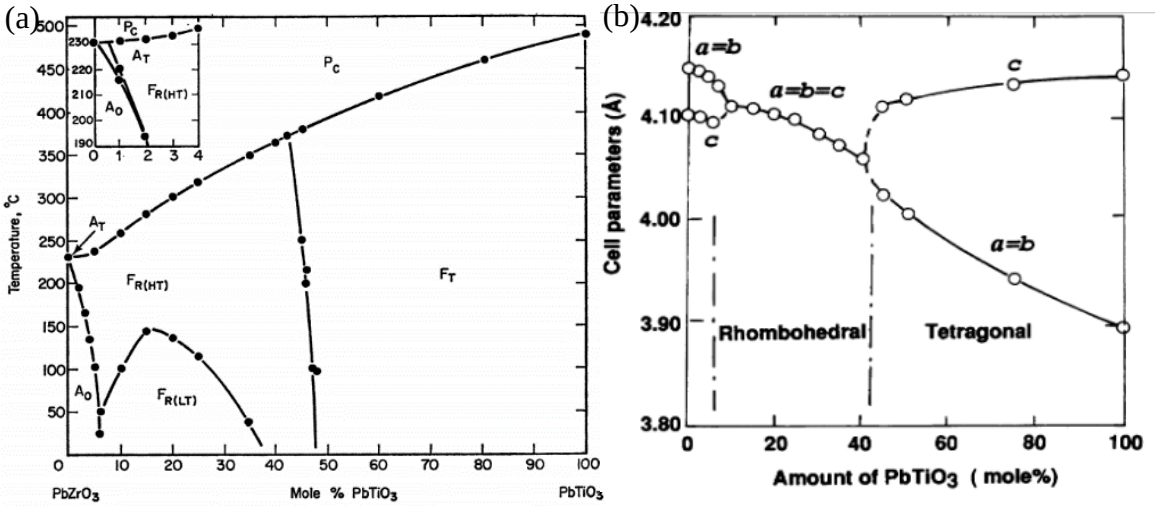

Figure 1-14. (a). Phase diagram of PZT with respect to the mole percentage of $PbTiO_3$. Above Curie temperature, the PZT shows cubic structure with no piezoelectric properties. Below Curie temperature, due to the different Zr/Ti ratio, the PZT presents different lattice structures. Used with permission [57] (b). Lattice parameters of PZT below Curie temperature with respect to the mole percentage of $PbTiO_3$. Used with permission [59]

(HT) [58]. The lattice parameters of PZT are also changing with the Zr/Ti ratio as shown in Fig. 1-14 (b) [59]. It is important to note that there is a boundary between FR and FT, which is called morphotropic phase boundary (MPB). At room temperature, MPB lies at the point Zr/Ti ≈ 53/47 [60]. At MPB, the two phases (FR and FT) are both existing in the PZT with the unstable state due to the energetically similar and elastically different between these two phases. It results in high mobility of domain walls and thus PZT can be easily poled [61]. Experiments have shown and demonstrated that large piezoelectric response generated in the PZT for Zr/Ti ratio close to this boundary.

1.3.2. Dielectric, Elastic and Piezoelectric Properties of PZT

Compared with other piezoelectric materials, higher dielectric and piezoelectric properties were found in PZT. It makes PZT a dominated piezoelectric material. Because PZT shows different lattice structures at different Zr/Ti ratios, the dielectric (relative permittivity), elastic (compliance coefficient, S_{11}) and piezoelectric (d_{33}) properties are varying with respect to the Zr/Ti ratio. As shown in Fig. 1-15 [62], sharp peak of relative permittivity, elastic compliance coefficient and piezoelectric coefficient are revealed in PZT at MPB as expected.

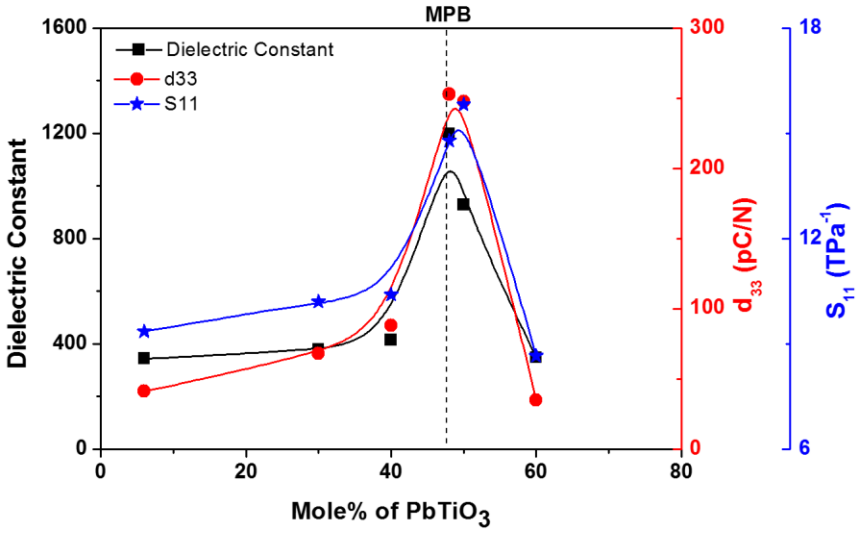

Figure 1-15. Dielectric, elastic and piezoelectric coefficients are highly depending upon the ratio of Zr/Ti. Around MPB, the maximum values of these three coefficients can be obtained. Recreated from [62]

In addition, temperature [62-64], thickness of PZT film [64-66], doping [67] are also demonstrated to play roles in affecting these three constants.

1.3.3. Hard and Soft PZT

Although the maximum piezoelectric coefficient can be obtained at MPB, in order to meet the specific requirements for different applications, a small amount of dopants ($\leq 3\%$ [69]) is added in the PZT to substitute some of A and B sites. Therefore, pure PZT turns to $PbX_zZr_yTi_xO_3$ (the sum of subscript x, y, and z is ONE), where X represents the additive.

Generally, there are two types of additives that have been adopted in PZT to modify the material properties. First is the donor type dopant (such as La^{3+}, Sb^{3+}, Bi^{3+}, W^{6+}), which provides unbound or free electrons to serve as current carriers . Donors with 3-valent ions at A positions to replace Pb^{2+}, or/and with 5 or 6-valent ions at B positions to replace Zr^{4+} and Ti^{4+} to create cation vacancies in the crystal structure of PZT [68]. This is known as "soft" PZT [69]. One example is $Pb_{0.96}(Zr_{0.52}Ti_{0.48}Nb_{0.024})O_3$ [70]. Donor dopant leads to high piezoelectric constants, permittivity, dielectric constants and dielectric loss due to increased domain wall mobility fascinating the domain reorientation, and thus allows this type of PZT primarily used in sensing purpose [71]. Another type of dopant is acceptor (such as Fe^{2+}, Fe^{3+}, Al^{3+}, Ga^{3+}), which provides positively charged anion vacancies in the crystal structure to accept electrons. The PZT that contains this type of dopant is called "hard" PZT [68]. One example is $Pb(Zr_{0.525}Ti_{0.472}Fe_{0.003})O_3$ [72]. Hard PZT owns opposite

properties as soft PZT. And it is more difficult to be polarized or depolarized resulting in more stabilized piezoelectric properties. Hard PZT are typically used in high mechanical loading or high voltage applications [71].

1.4. Overview of the Thesis

1.4.1. Literature Review on Piezoelectric Transducers (Chapter 2)

Piezoelectric material has been widely used in MEMS devices. In order to understand the piezoelectric transducers, including the categories, function, and the state-of-art in this field, a literature review is presented in Chapter 2. This chapter is consisting of three major piezoelectric transducers, namely actuators, sensors, and energy harvesters. Depending upon the different configurations and functions, these three categories are further divided into several sub-branches for clearer introduction. By introducing how piezoelectric effect is employed into these devices theoretically and taking several examples from literature, this chapter intends to give an overall picture of the application of piezoelectric effect in MEMS.

1.4.2. Photonic Sintering of Printed PZT Thick Films (Chapter 3)

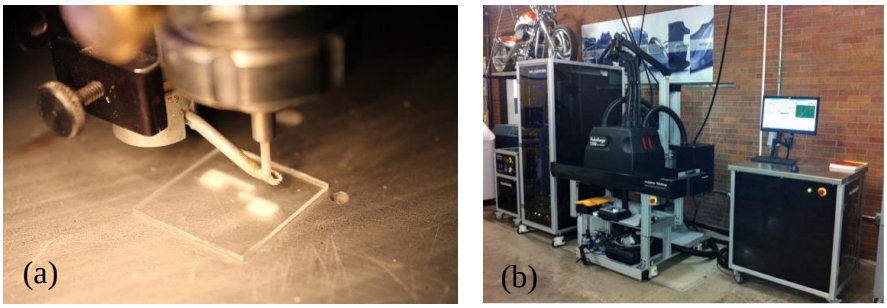

Figure 1-16. (a) Aerosol-Jet printer and (b) PulseForge photonic sintering system.

Few conventionally popular PZT film fabrication processes are introduced in Chapter 3 with the benefits and limitations. New PZT film deposition and sintering methods are then described. Firstly, to avoid complex subsequent processes (photolithography, etching, etc.) following the deposition to obtain desired features, a direct writing technique, i.e. aerosol-jet printing (Fig. 1-16 (a)), is employed to directly print PZT with designed structures on the substrate. Secondly, photonic sintering technique is adopted to densify the PZT film and accordingly enhance the film mechanical and piezoelectric properties (Fig 1-16 (b)). The detailed information of these two techniques is presented in Chapter 3.

By utilizing this process, a PZT thick film is successfully prepared on stainless steel substrate with significantly short processing duration. Compared with thermally sintered PZT thick films, photonic sintered group shows superior piezoelectric properties. All of the measurements are also presented in Chapter 3.

1.4.3. Photonic Sintered Flexible Energy Harvester (Chapter 4)

Due to the energy transfer direction and extremely short flash duration, the substrate temperature increase, during sintering, is found to be low. Therefore, the photonic sintering of PZT creates the possibility of preparing PZT on low melting point substrate. A polyethylene terephthalate (PET) sheet (melting point = 260 °C) is used to serve as the substrate for the experimental demonstration. Currently, the fabrication process of flexible piezoelectric energy harvester built on the low melting point substrate demands a complex sintered PZT film transfer step due to the mismatch between the melting temperature of the substrate and the film sintering temperature. However, by using this new process technique, a flexible d_{33} mode piezoelectric energy harvester is fabricated directly on the PET and tested. Desirable energy output is detected during measurement. The fabrication and testing processes are presented in Chapter 4 in detail.

1.4.4. Piezoelectric Properties Manipulation (Chapter 5)

Sintering and dipole reorientation (or poling) are two necessary fabrication steps for realizing ferroelectric film devices. Generally, these two steps are separately processed, which requires long procession duration and increases the complexity. The temperature changes due to the rapid pulsed flash accomplish the cyclic temperature excursions in the PZT film to above and below the Curie temperature, which provides a well temperature condition for dipole reorientation and creates the opportunity for the simultaneous performance of poling during photonic sintering. Chapter 5 is focusing on the demonstration of dipole reorientation during photonic sintering to further enhance the piezoelectric properties and shorten the procession duration. The film was characterized using g_{33} and d_{33}. Comparison was carried out with other 5 control groups to verify the enhancement of piezoelectric properties.

References:

[1] R. Besson, J. Boy, B. Glotin, Y. Jinzaki, B. Sinha, and M. Valdois, "A dual-mode thickness-shear quartz pressure sensor," *Ultrasonics, Ferroelectrics, and Frequency Control, IEEE Transactions on,* vol. 40, pp. 584-591, 1993.

[2] G. Caliano, N. Lamberti, A. Iula, and M. Pappalardo, "A piezoelectric bimorph static pressure sensor," *Sensors and Actuators A: Physical,* vol. 46, pp. 176-178, 1995.

[3] A. Shirinov and W. Schomburg, "Pressure sensor from a PVDF film," *Sensors and Actuators A: Physical,* vol. 142, pp. 48-55, 2008.

[4] Y. Wang, J. Zheng, G. Ren, P. Zhang, and C. Xu, "A flexible piezoelectric force sensor based on PVDF fabrics," *Smart Materials and Structures,* vol. 20, p. 045009, 2011.

[5] Y. Nemirovsky, A. Nemirovsky, P. Muralt, and N. Setter, "Design of novel thin-film piezoelectric accelerometer," *Sensors and Actuators A: Physical,* vol. 56, pp. 239-249, 1996.

[6] P. Scheeper, J. O. Gulløv, and L. M. Kofoed, "A piezoelectric triaxial accelerometer," *Journal of Micromechanics and Microengineering,* vol. 6, p. 131, 1996.

[7] J.-C. Yu and C.-B. Lan, "System modeling of microaccelerometer using piezoelectric thin films," *Sensors and Actuators A: Physical,* vol. 88, pp. 178-186, 2001.

[8] Q. Zou, W. Tan, E. S. Kim, and G. E. Loeb, "Single-and triaxis piezoelectric-bimorph accelerometers," *Microelectromechanical Systems, Journal of,* vol. 17, pp. 45-57, 2008.

[9] S. Joshi, M. Parmar, and K. Rajanna, "A novel gas flow sensing application using piezoelectric ZnO thin films deposited on Phynox alloy," *Sensors and Actuators A: Physical,* vol. 187, pp. 194-200, 2012.

[10] A. Kuoni, R. Holzherr, M. Boillat, and N. F. de Rooij, "Polyimide membrane with ZnO piezoelectric thin film pressure transducers as a differential pressure liquid flow sensor," *Journal of Micromechanics and Microengineering,* vol. 13, p. S103, 2003.

[11] H. Liu, S. Zhang, R. Kathiresan, T. Kobayashi, and C. Lee, "Development of piezoelectric microcantilever flow sensor with wind-driven energy harvesting capability," *Applied Physics Letters,* vol. 100, p. 223905, 2012.

[12] H.-B. Fang, J.-Q. Liu, Z.-Y. Xu, L. Dong, L. Wang, D. Chen, B.-C. Cai, and Y. Liu, "Fabrication and performance of MEMS-based piezoelectric power generator for vibration energy harvesting," *Microelectronics Journal,* vol. 37, pp. 1280-1284, 2006.

[13] F. Goldschmidtboeing and P. Woias, "Characterization of different beam shapes for piezoelectric energy harvesting," *Journal of Micromechanics and Microengineering,* vol. 18, p. 104013, 2008.

[14] A. R. Penmetcha, J. Ouyang, D. Cormier, and D. A. Borkholder, "Photonically Sintered PZT Energy Harvester," presented at the Proceedings of the ASME 2015 International Mechanical Engineering Congress & Exposition, IMECE 2015, Houston, TX, 2015.

[15] S. Roundy and P. K. Wright, "A piezoelectric vibration based generator for wireless electronics," *Smart Materials and Structures,* vol. 13, p. 1131, 2004.
[16] W. D. Callister and D. G. Rethwisch, *Materials science and engineering: an introduction* vol. 7: Wiley New York, 2007.
[17] C. Kittel, *Introduction to solid state physics*: Wiley, 2005.
[18] R. Bechmann, "Elastic and piezoelectric constants of alpha-quartz," *Physical review,* vol. 110, p. 1060, 1958.
[19] H. Jaffe and D. Berlincourt, "Piezoelectric transducer materials," *Proceedings of the IEEE,* vol. 53, pp. 1372-1386, 1965.
[20] W. G. Cady, *Piezoelectricity: An introduction to the theory and application of electromechanical phenomena in crystals*: McGraw-Hill, 1946.
[21] J. G. Gualtieri, J. Kosinski, and A. Ballato, "Piezoelectric materials for acoustic wave applications," *Ultrasonics, Ferroelectrics, and Frequency Control, IEEE Transactions on,* vol. 41, pp. 53-59, 1994.
[22] H.-R. Jung, B.-M. Jin, J.-W. Cha, and J.-N. Kim, "Piezoelectric and elastic properties of $Li_2B_4O_7$ single crystal," *Materials Letters,* vol. 30, pp. 41-45, 1997.
[23] M. Adachi, T. Kimura, W. Miyamoto, Z. Chen, and A. Kawabata, "Dielectric, Elastic and Piezoelectric Properties of $La_3Ga_5SiO_{14}$ (LANGASITE) Single Crystals," *JOURNAL-KOREAN PHYSICAL SOCIETY,* vol. 32, pp. S1274-S1277, 1998.
[24] A. Dubovskiy, E. Domoroshchina, G. Kuz'micheva, and G. Semenkovich, "Changes in defects under external influence in langasite crystals," in *Frequency Control Symposium and Exposition, 2004. Proceedings of the 2004 IEEE International*, 2004, pp. 642-645.
[25] M. Petrov, A. Paugurt, V. Bryksin, S. Wevering, B. Andreas, and E. Krätzig, "Dynamic light beam deflection caused by space charge waves in photorefractive crystals," *Applied Physics B: Lasers and Optics,* vol. 69, pp. 341-344, 1999.
[26] A. Slobodnik Jr and J. Sethares, "Elastic, Piezoelectric, and Dielectric Constants of $Bi_{12}GeO_{20}$," *Journal of Applied Physics,* vol. 43, pp. 247-248, 1972.
[27] S. Zhu, B. Jiang, and W. Cao, "Characteriation of piezoelectric materials using ultrasonic and resonant techniques," *Proceedings of the SPIE,* vol. 3341, pp. 154-162, 1998.
[28] K. Uchino, *Ferroelectric Devices 2nd Edition*: CRC press, 2009.
[29] Y. Jeon, R. Sood, J.-H. Jeong, and S.-G. Kim, "MEMS power generator with transverse mode thin film PZT," *Sensors and Actuators A: Physical,* vol. 122, pp. 16-22, 2005.
[30] P. Muralt, "PZT thin films for microsensors and actuators: Where do we stand?," *Ultrasonics, Ferroelectrics, and Frequency Control, IEEE Transactions on,* vol. 47, pp. 903-915, 2000.
[31] P. Muralt, M. Kohli, T. Maeder, A. Kholkin, K. Brooks, N. Setter, and R. Luthier, "Fabrication and characterization of PZT thin-film vibrators for micromotors," *Sensors and Actuators A: Physical,* vol. 48, pp. 157-165, 1995.
[32] D. Shen, J.-H. Park, J. Ajitsaria, S.-Y. Choe, H. C. Wikle III, and D.-J. Kim, "The design, fabrication and evaluation of a MEMS PZT cantilever with an integrated Si proof mass for vibration energy harvesting," *Journal of Micromechanics and Microengineering,* vol. 18, p. 055017, 2008.

[33] J. Ramsay and E. Mugridge, "Barium titanate ceramics for fine-movement control," *Journal of Scientific Instruments,* vol. 39, p. 636, 1962.
[34] Z. Wang, J. Hu, A. P. Suryavanshi, K. Yum, and M.-F. Yu, "Voltage generation from individual $BaTiO_3$ nanowires under periodic tensile mechanical load," *Nano letters,* vol. 7, pp. 2966-2969, 2007.
[35] K.-I. Park, S. Xu, Y. Liu, G.-T. Hwang, S.-J. L. Kang, Z. L. Wang, and K. J. Lee, "Piezoelectric $BaTiO_3$ thin film nanogenerator on plastic substrates," *Nano letters,* vol. 10, pp. 4939-4943, 2010.
[36] K. Abe, K. Uchino, and S. Nomura, "Barium titanate-based actuator with ceramic internal electrodes," *Ferroelectrics,* vol. 68, pp. 215-223, 1986.
[37] A. Odon, "Probe with PVDF sensor for energy measurements of optical radiation," *Measurement Science Review,* vol. 3, pp. 111-114, 2003.
[38] F. Charette, A. Berry, and C. Guigou, "Active control of sound radiation from a plate using a polyvinylidene fluoride volume displacement sensor," *The Journal of the Acoustical Society of America,* vol. 103, pp. 1493-1503, 1998.
[39] J. Kymissis, C. Kendall, J. Paradiso, and N. Gershenfeld, "Parasitic power harvesting in shoes," in *Wearable Computers, 1998. Digest of Papers. Second International Symposium on*, 1998, pp. 132-139.
[40] N. Stucki, "Artificial ferroelectric materials," University of Geneva, 2008.
[41] D. Damjanovic, "Ferroelectric, dielectric and piezoelectric properties of ferroelectric thin films and ceramics," *Reports on Progress in Physics,* vol. 61, p. 1267, 1998.
[42] P. Marton, I. Rychetsky, and J. Hlinka, "Domain walls of ferroelectric $BaTiO_3$ within the Ginzburg-Landau-Devonshire phenomenological model," *Physical Review B,* vol. 81, p. 144125, 2010.
[43] I. D. Mayergoyz and G. Bertotti, *The science of hysteresis* vol. 3: Elsevier, 2005.
[44] M. E. Lines and A. M. Glass, *Principles and applications of ferroelectrics and related materials*: Oxford University Press, 1977.
[45] G. Arlt, "Twinning in ferroelectric and ferroelastic ceramics: stress relief," *Journal of Materials Science,* vol. 25, pp. 2655-2666, 1990.
[46] L. Jin, F. Li, and S. Zhang, "Decoding the fingerprint of ferroelectric loops: comprehension of the material properties and structures," *Journal of the American Ceramic Society,* vol. 97, pp. 1-27, 2014.
[47] C. B. Sawyer and C. Tower, "Rochelle salt as a dielectric," *Physical review,* vol. 35, p. 269, 1930.
[48] J. Hemberger, P. Lunkenheimer, R. Viana, R. Böhmer, and A. Loidl, "Electric-field-dependent dielectric constant and nonlinear susceptibility in $SrTiO_3$," *Physical Review B,* vol. 52, p. 13159, 1995.
[49] A. dos Santos, L. Cardoso, J. Sasaki, M. Miranda, and F. Melo, "X-ray multiple diffraction as a probe to determine all the piezoelectric coefficients of a crystal: Rochelle salt case," *Journal of Physics: Condensed Matter,* vol. 15, p. 7835, 2003.
[50] Y. Xu, *Ferroelectric materials and their applications*: Elsevier, 2013.
[51] D. Berlincourt and H. Jaffe, "Elastic and piezoelectric coefficients of single-crystal barium titanate," *Physical review,* vol. 111, p. 143, 1958.

[52] R. Bechmann, "Elastic, piezoelectric, and dielectric constants of polarized barium titanate ceramics and some applications of the piezoelectric equations," *The Journal of the Acoustical Society of America,* vol. 28, pp. 347-350, 1956.
[53] Y. Roh, V. V. Varadan, and V. K. Varadan, "Characterization of all the elastic, dielectric, and piezoelectric constants of uniaxially oriented poled PVDF films," *Ultrasonics, Ferroelectrics, and Frequency Control, IEEE Transactions on,* vol. 49, pp. 836-847, 2002.
[54] S. Sokhanvar, M. Packirisamy, and J. Dargahi, "A multifunctional PVDF-based tactile sensor for minimally invasive surgery," *Smart Materials and Structures,* vol. 16, p. 989, 2007.
[55] A. Warner, M. Onoe, and G. Coquin, "Determination of elastic and piezoelectric constants for crystals in class (3m)," *The Journal of the Acoustical Society of America,* vol. 42, pp. 1223-1231, 1967.
[56] W. Mason, "Theory of the ferroelectric effect and clamped dielectric constant of Rochelle salt," *Physical review,* vol. 72, p. 854, 1947.
[57] B. Jaffee, W. Cook, and H. Jaffee, "Peizoelectric Ceramics," ed: Academic Press, New York, 1971.
[58] X. Dai and Y. Wang, "Study on the Order of the FR (LT)–FR (HT) Phase Transition of PZT Ceramics," *physica status solidi (a),* vol. 124, pp. 435-440, 1991.
[59] G. Shirane, K. Suzuki, and A. Takeda, "Phase transitions in solid solutions of $PbZrO_3$ and $PbTiO_3$ (II) X-ray study," *Journal of the Physical Society of Japan,* vol. 7, pp. 12-18, 1952.
[60] C. K. Kwok and S. B. Desu, "Low temperature perovskite formation of lead zirconate titanate thin films by a seeding process," *Journal of materials research,* vol. 8, pp. 339-344, 1993.
[61] X. Zhu, *Piezoelectric Ceramic Materials: Processing, Properties, Characterization, and Applications*: Nova Science Publishers, 2010.
[62] Z. Zhuang, M. J. Haun, S.-J. Jang, and L. E. Cross, "Composition and temperature dependence of the dielectric, piezoelectric and elastic properties of pure PZT ceramics," *Ultrasonics, Ferroelectrics, and Frequency Control, IEEE Transactions on,* vol. 36, pp. 413-416, 1989.
[63] S. Sherrit, G. Yang, H. Wiederick, and B. Mukherjee, "Temperature dependence of the dielectric, elastic and piezoelectric material constants of lead zirconate titanate ceramics," in *Proceedings of the international conference on smart materials, structures and systems*, pp. 7-10, 1999.
[64] R. Wolf and S. Trolier-McKinstry, "Temperature dependence of the piezoelectric response in lead zirconate titanate films," *Journal of Applied Physics,* vol. 95, pp. 1397-1406, 2004.
[65] L. Lian and N. Sottos, "Effects of thickness on the piezoelectric and dielectric properties of lead zirconate titanate thin films," *Journal of Applied Physics,* vol. 87, pp. 3941-3949, 2000.
[66] F. Xu, S. Trolier-McKinstry, W. Ren, B. Xu, Z.-L. Xie, and K. Hemker, "Domain wall motion and its contribution to the dielectric and piezoelectric properties of lead zirconate titanate films," *Journal of Applied Physics,* vol. 89, pp. 1336-1348, 2001.

[67] R. G. Sabat, B. K. Mukherjee, W. Ren, and G. Yang, "Temperature dependence of the complete material coefficients matrix of soft and hard doped piezoelectric lead zirconate titanate ceramics," *Journal of Applied Physics,* vol. 101, p. 064111, 2007.
[68] W. Heywang, K. Lubitz, and W. Wersing, *Piezoelectricity: evolution and future of a technology* vol. 114: Springer Science & Business Media, 2008.
[69] D. Berlincourt, "Piezoelectric ceramic compositional development," *The Journal of the Acoustical Society of America,* vol. 91, pp. 3034-3040, 1992.
[70] X. Yang and T. Chaki, "Preparation and properties of $Pb_{0.99}Nb_{0.02}(Zr_{0.52}Ti_{0.48})_{0.98}O_3$ by a new sol–gel technique," *Journal of Materials Science,* vol. 32, pp. 4661-4671, 1997.
[71] L. APC International. *Soft vs. Hard Ceramics*. Available: https://www.americanpiezo.com/piezo-theory/ceramics.html
[72] T. Weston, A. Webster, and V. McNamara, "Lead Zirconate-Lead Titanate Piezoelectric Ceramics with Iron Oxide Additions," *Journal of the American Ceramic Society,* vol. 52, pp. 253-257, 1969.

Chapter 2 Piezoelectric Transducers

2.1. Introduction

Piezoelectric effects, including direct and inverse piezoelectric effects, have been extensively used in MEMS (microelectromechanical systems) devices recently. It is defined as the electric polarization (or mechanical strain) linearly produced by mechanical strain (or applied electric field).

The piezoelectric transducers can be divided into three classes according to the thickness [1]: If the thickness is over 25 μm, it is called bulk piezoelectric device. The established industrial manufacturing approaches have better reliability for bulk devices. For the film thickness in the range of 1 ~ 25μm, it is called thick film piezoelectric device. Compared with bulk devices, the key advantages of thick film are the lower driving voltage and high-frequency applications. If the thickness is lower than 1μm, it is called thin film piezoelectric device.

Although there are many benefits of using the piezoelectric material for transducer applications, limitations cannot be overlooked. Most of the piezoelectric materials are containing toxic components that are unfriendly to the environment and harmful to the human's health. For instance, Lead, a highly poisonous metal, is contained in Lead Zirconate Titanate material. Therefore, proper manufacturing processes and disposing methods are significantly important. Additionally, most piezoelectric materials have excellent chemical resistance [2]. Consequently, complex processes have to be involved to fabricate desired designed features.

2.2. Piezoelectric Actuators

Actuators are the devices operated by the driving power (electrical, thermal, and optical) to output the motion or force for the system. Based on the mechanism of the driving power, actuators can by classified into different types, such as thermal actuators [3-5], electrostatic actuators [6-8], and piezoelectric actuators. The piezoelectric actuators take advantage of the inverse piezoelectric effect to convert the electric power into mechanical deformation to obtain the displacement. Piezoelectric actuators are widely used due to its high precision (1 – 10 nm), large force generation (commercially available piezoelectric actuators is able to generate up to several tons force within a range 100's of μm deflection [9]), fast response time (in the range of micro-sec), small size and thermal expansion during actuation [10]. However, the major drawback of a piezoelectric actuator is the accuracy because of the ferroelectric hysteresis loop [11]. In addition, small generated strain limits the piezoelectric actuators used for large displacement applications [12].

Because of aforementioned characterization of the piezoelectric actuators, they are suitable for large forces but small strain applications. Many MEMS devices have integrated piezoelectric actuators, such as micro-pumps, micro-mirrors, and atomic force microscope (AFM), with two commonly used configurations, cantilever shape and membrane shape.

2.2.1. Cantilever-Shaped Actuators

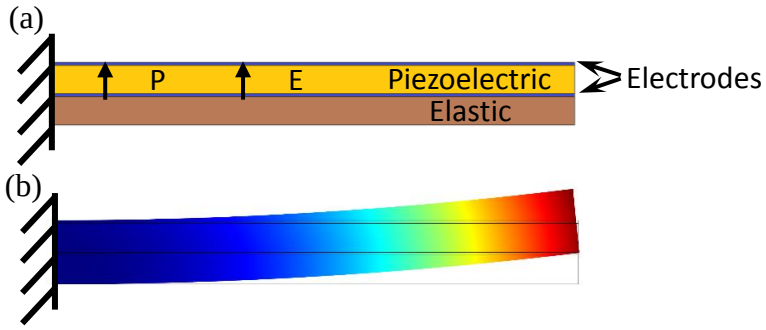

Figure 2-1. Diagram of a unimorph cantilever-shaped actuator (a). The piezoelectric material is sandwiched between two electrodes (blue) and deposited on an elastic material. The cantilever is bended while electric field is applied through the piezoelectric material (b).

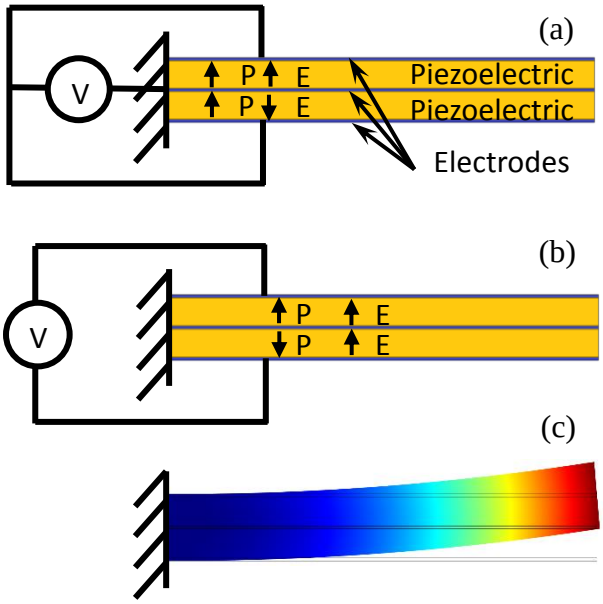

Figure 2-2. Two configurations of the bimorph cantilever-shaped actuator. Two layers of piezoelectric materials are separated by a center electrode layer. The bending is generated in the cantilever by either (a) oppositely applying the electric field to the two piezoelectric layers that have the same poling direction (parallel connection), or (b) poling oppositely but applying the electric field through the entire cantilever (series connection). After the application of the electric field, both cases will be bended up (c).

The cantilever-shaped actuators employ a single piezoelectric material that is sandwiched between electrically conductive materials and deposited on the cantilever-shaped, non-piezoelectric elastic material substrate with one fixed end and one free end. Therefore, the electric field applied between two electrodes results in the strain along the transverse direction. However, because of the strain resist of the substrate elastic material, the bending is induced in the structure. Upon removal of the field, the elastic restoring energy causes the cantilever recovered to the original flat shape. This so-called unimorph structure [13, 14], also known as heterogenerous bimorph or monomorph structure [15], is shown in Fig. 2-1. In order to amplify the tip deflection, bimorph cantilever-shaped piezoelectric actuators are designed [16, 17]. As shown in Fig. 2-2, a bimorph structure consists of two piezoelectric material separated by a thin electrode layer. By either oppositely applying electric field to the two piezoelectric layers (same poling direction) (Fig. 2-2 (a)) or oppositely poling the piezoelectric material (same applied electric field direction) (Fig. 2-2 (b)), elongation is induced in one layer of piezoelectric material, while shrinkage in the other layer. The deformation difference between top and bottom piezoelectric materials leads to a larger deflection (approximately two times larger than unimorph structure [18]) at the cantilever tip.

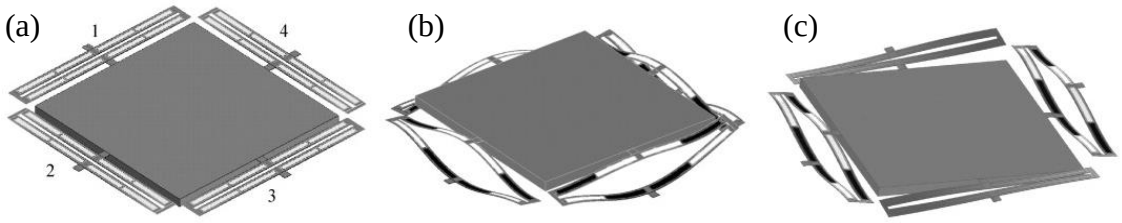

Figure 2-3. A micromirror with four cantilever-shaped piezoelectric actuator groups (a). When exciting different groups of actuators, the micromirro can achieve lowering, lifting (b), or angle changing (c). Used with permission [22]

Micromirrors have received a great deal of attention due to their wide applications in biomedical imaging [19], optical phased arrays [20], and projection displays [21]. For piezoelectric actuated micromirrors, most designs consist of at least one cantilever structure that supports and excites the mirror to bending vibration and twisting rotation. For instance, recently, Liu et al [22] employed four groups of unimorph structure piezoelectric actuators in a micromirror to control the tilting angle of the device. As shown in Fig. 2-3, by applying electric field to different cantilever combinations, the micromirror

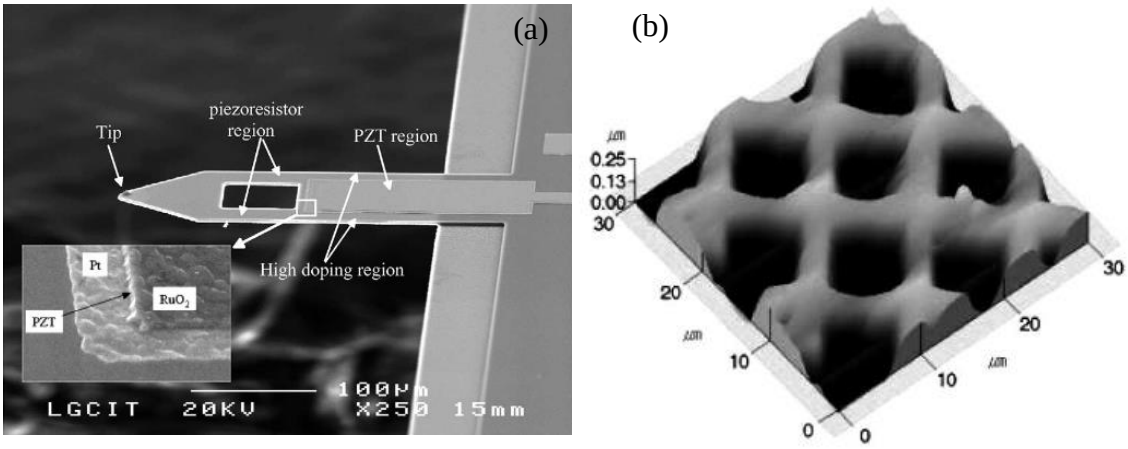

Figure 2-4. SEM image of a single AFM cantilever actuated by piezoelectric material (a) and the morphology measured using this device (b). Used with permission [23]

is able to face to the expected directions with well controlled tilting angles.

Atomic force mircroscopes (AFM) are powerful tool for imaging surface or atoms morphology via measuring (using a detection system) the displacement of a fine cantilever tip as the sample surface moves under it. To obtain high resolution images with high scanning speed, piezoelectric material is adopted for actuation purpose due to its capability of nano-meter deflection and high resonance frequency. Kim et al [23] developed an array of PZT cantilevers (Fig. 2-4 (a)) with a 73 kHz resonance frequency for AFM function.

And the scanning speed is able to reach 1 mm/s with good detected topographical image (Fig. 2-4 (b)). However, some undesirable properties such as hysteresis, nonlinear sensitivity, thermal drift and creep cause image distortions and bad repeatability [24, 25]. Many researches have been carried out to minimize or eliminate these defects. For example, Leang et al [25] designed a feedback and feedforward controller to compensate creep and hysteresis effects in a piezoelectric AFM system.

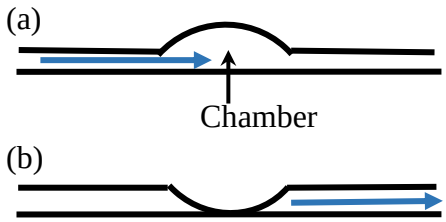

Figure 2-5. When the diaphragm is deformed up (a) or down (b), the fluid is sucked in to or pushed out from the chamber, respectively. This realizes the fluidic pumping function.

Micropumps are significantly essential device in drug delivery system to controllably deliver a fine volume of drugs from reservoir to the desired object. Conventional drug delivery approaches, such as oral tablets, injections, and inhalers, cannot deliver all drugs with accurately desired therapeutic rate range or do not directly deliver to the affected area. Therefore, utilization of a micropump is able to eliminate the inaccuracy and inefficiency. Because of the purpose of fine controlling delivered drug volume and rate, the piezoelectric material was widely employed in this application since one of the early piezoelectric micropumps for insulin delivery was fabricated [26]. Typically, the piezoelectric material is used to deflect the diaphragm of the chamber, with the combination of unidirectional valves or a peristaltic structure, to suck the fluid in (Fig. 2-5 (a)) and push it out (Fig. 2-5 (b)) unidirectionally. By repeating this cycle, the functional fluid is transferred from the inlet (connected to the reservoir) to the outlet (to the affected area). The benefits of using the piezoelectric material in micropump application include good reliability, energy efficiency, and moderately pressure and displacement. Wang et al. [27] designed a high flow-rate piezoelectric micropump

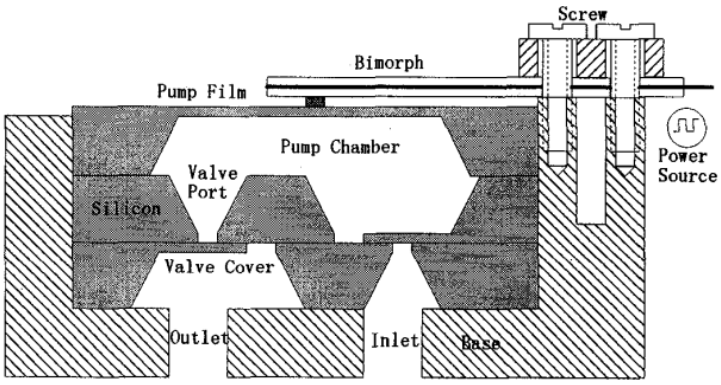

Figure 2-6. A cantilever-shaped PZT actuator was built on top of the micropump to deflect the chamber and to realize the fluid flows from inlet to outlet. Used with permission [27]

actuated by a top cantilever-shaped piezoelectric actuator as shown in Fig. 2-6, which was experimentally demonstrated a maximum flow rate of 365 µl/min with a maximum back pressure of 2.38 kPa when using 100 V_{pp} square actuator driving voltage at 20 Hz.

2.2.2. Membrane-Shaped Actuators

Generally, membrane-shaped piezoelectric actuators are fabricated by depositing piezoelectric films on top of a substrate, which is typically made of silicon [28] or Polydimethylsiloxane (PDMS) [29]. Therefore, the piezoelectric effective expansion of the film is limited due to the substrate expansion resistance resulting in structural bending in the film and diaphragm. The maximum deflection is located at the center of the film. However, due to the low stiffness of the bending structure, the actuators are typically used in low force and small displacement applications, such as micropumps, ink-jet printers, and micro-motors.

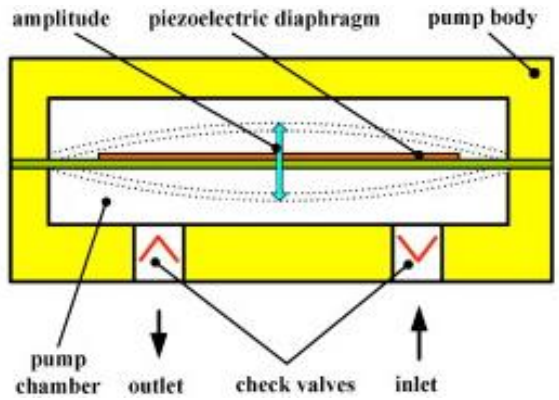

Figure 2-8. Piezoelectric membrane is deflected up and down due to the directional alternation of applied electric field. And this causes fluid sucked in and pumped out through the chamber. Used with permission [34]

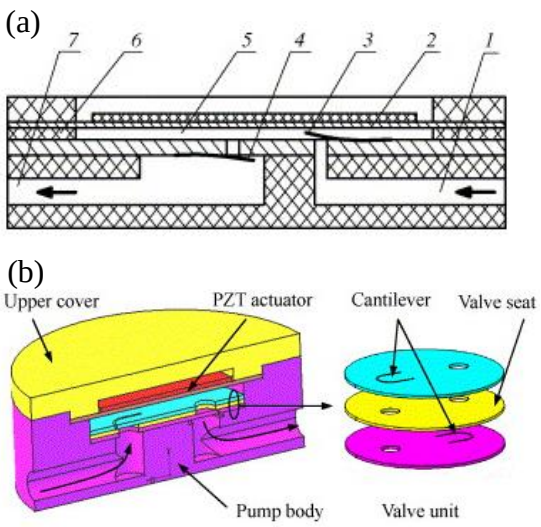

Figure 2-7. The diagram of the micropump with a circular shaped piezoelectric actuator. (a) The cross-sectional view of the Kan et al. designed micropump. It consists of an inlet (1), one piezoelectric film actuator (2), two cantilever valves (3, 4), one pump chamber (5), pump body (6) and an outlet (7). (b) The 3-D structure of the micropump. Used with permission [30]

Recently, micropumps driven by piezoelectric membrane-shaped actuators have been studied intensively. Kan et al [30] designed a circular piezoelectric thin-film actuator micropump as shown in Fig. 2-7. Up to approximately 3.5 ml/min flow rate was achieved with 50 V actuation voltage and 0.8 Hz frequency. Besides circular shape, square- [31], rectangular- [32], even dome-shaped [33] piezoelectric membranes are all developed for different

flow rate and stiffness purposes. Moreover, Zhang et al [34] designed a micropump that directly uses piezoelectric material as the diaphragm with no substrate. When the piezoelectric diaphragm is excited by alternating electric field, it buckles up and down due to the change of the sign of the electric field, and thereby the fluid is able to pumped in and out resulting from the deflection of the piezoelectric diaphragm (Fig. 2-8) .

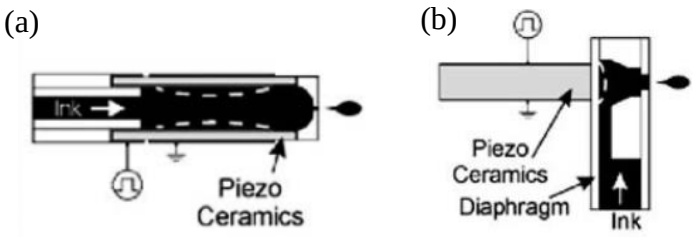

Figure 2-9. Two ink ejection modes used in ink-jet printing technology. (a) The piezoelectric actuator is placed over the wall and squeeze the ink out during actuation. (b) The piezoelectric actuator is on top of the ink chamber and pushing the ink out during actuation. Used with permission [35]

Both research and commercial ink ejecting applications also employ piezoelectric membranes due to their requirement of controllably fine deflection. Therefore, during piezoelectric actuation, an expected volume of ink stored in the cartridge is either squeezed (Fig. 2-9 (a)) or pushed (Fig. 2-9 (b)) out and deposited to the substrate [35]. Commercially available down to 1 pL ink drop volumes has been developed by FUJIFILM Corp. using piezoelectric actuators.

Another application of membrane-shaped piezoelectric actuator is ultrasonic micromotor. Since ultrasonic piezoelectric micromotor was invented by Vishnevsky et al. [36], many commercial products and researches [37-39] have been developed. Generally, an ultrasonic micromotor is driven under the piezoelectric material resonance frequency (in the range of 20 – 150 kHz). And it firstly converts electrical energy to oscillatory bending motion via piezoelectric material. Depending upon the excitation modes of bending (longitudinal, torsional or flexural), the structure can be induced series of travelling waves of

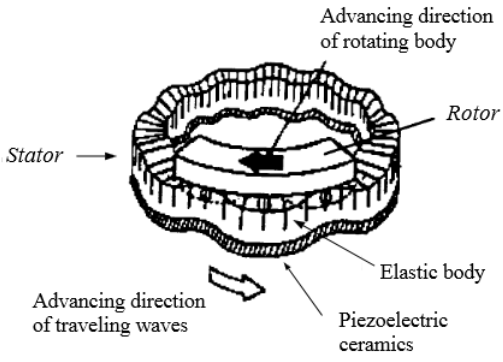

Figure 2-10. A wave of mechanical deformation with ultrasonic frequency is generated in the piezoelectric material to deform the stator. The top rotor is therein travelling along the stator following the wave. Used with permission [39]

deformation. This deformation occurs in a stator. Then this deformation is rectified to a driving force to achieve a unidirectional rotary or linear motion in a rotor or a carriage as shown in Fig. 2-10.

2.3. Piezoelectric Sensors

Sensors are the devices that convert a non-electrical physical or chemical quantity or parameter into an electrical signal and thereby can be detected and to convey information. Generally, an ideal sensor should: be able to be operated continuously without affecting the measurand; have appropriate sensitivity for a specific application and selectivity for a measurand; own fast and predictable response to the measurand; have a high signal to noise ratio (SNR); and be calibrated easily. As a microsensor, compacted size is also one of the most essential requirements. Piezoelectric material is a good microsensor candidate because of the direct piezoelectric effect. Basically, piezoelectric sensors are force sensors. Based upon the designs, piezoelectric force sensors can be expanded to other force related parameters sensing applications. However, the major drawback of piezoelectric sensors is that they can only measure dynamic or quasi-static force. Moreover, small electric signal output of the piezoelectric sensors requires an amplifying circuit for most applications. Although piezoelectric sensors have high SNR, the resistance from severe environmental condition, such as temperature (due to pyroelectric effect), vibration, electric and magnetic fields, is low and accordingly results in adversely influence to the performance of the sensor. Therefore, packaging sensors with protective materials or components is needed.

The first piezoelectric sensor was designed for force, pressure and acceleration measurement purposes in the period of World War I for research only [40]. Later, J. Thomson firstly reported a piezoelectric pressure sensor in year of 1919 [41]. Since then, piezoelectric sensors have gained great attention and development resulting in increasingly number of applications in deep ocean exploration [42, 43], structural health monitoring [44], and smart autonomous robot [45, 46]. In this section, several piezoelectric sensors will be introduced with their principles and applications.

2.3.1. Pressure sensors

The quantity “pressure” is defined as a force exerted on a unit area surface. Therefore, piezoelectric pressure sensor is a special form of force sensor with a design of a constant

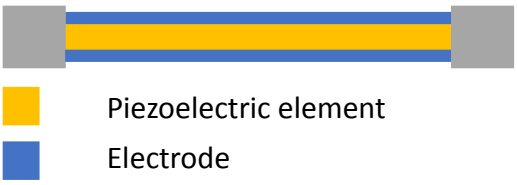

Figure 2-11. Diagram of a basic piezoelectric sensing element. The piezoelectric material is sandwiched between top and bottom electrodes. And the entire structure is anchored to the substrate.

effective area, generally a diaphragm. Basically, there are two types of pressure sensors, namely absolute and differential pressure sensors. Both types are measuring the difference between the reference pressure and given pressure. However, the reference pressure of the former type is the pressure in a sealed chamber, generally a vacuum environment (ideally, zero Pa); while the reference pressure of the latter type is a non-zero pressure level (mostly are atmospheric pressure). Absolute pressure sensors can be used as barometric pressure sensors [47], while the differential pressure sensors are reported for the applications of flow rate measurement [48] and arterial pressure monitoring [49]. The basic structure of the piezoelectric sensing element is shown in Fig. 2-11. The piezoelectric material (generally a film) is sandwiched between top and bottom electrodes. So the application of the force to the sensor induces charges accumulated in the electrodes and detectable. Therefore, the pressure can be easily obtained by dividing the measured force by the fixed effective sensing surface area. This structure is adopted to many piezoelectric sensing applications. For instance, Kuoni et al. designed a ZnO piezoelectric flow rate sensor by measuring the differential pressure at two chambers using this structure (Fig. 2-12) [48]. The sensitivity of single pressure sensor at one chamber was measured to approximately 8 mV/mbar. When the fluid flows through the pump, the pressure difference between two chambers were measured and used to calculate the flow rate. One more example is shown in Fig. 2-13 (a), a pressure sensor made from PVDF proposed by Shirinov and Schomburg [50]. The applied pressure deforms the PVDF foil, and accordingly induces the electric signal. As previously mentioned, the output of the signal of piezoelectric sensor is too small to be measured accurately. Amplifying circuit

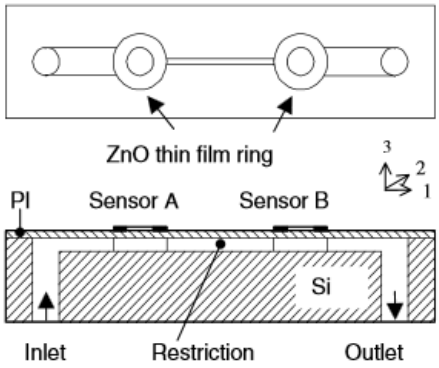

Figure 2-12. Diagrams of top and cross-sectional view of the differential pressure flow rate sensor. By measuring the pressure difference at the diaphragms of two chambers (chamber A and B), the flow rate can be calculated. Used with permission [48]

is needed in most applications. Fig. 2-13 (b) is one of the methods for amplifying the signal used in [50]. And by thoroughly choosing the capacitance of C_0, the output voltage can be amplified since it is the quotient of dividing PVDF generated charge (Q) by C_0.

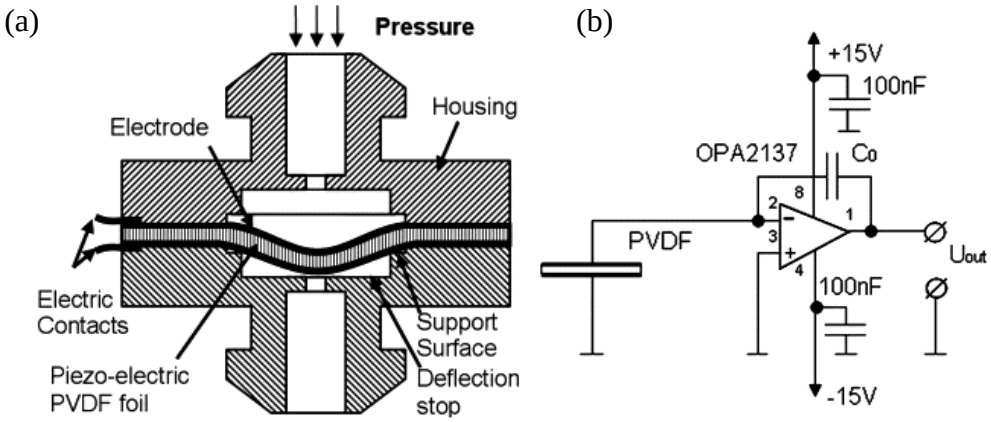

Figure 2-13. (a) The diagram of a PVDF foil pressure sensor. (b) The output signal was amplified by connecting with an amplifying circuit. Used with permission [50]

2.3.2. Accelerometers

Piezoelectric accelerometer was firstly designed by Bruel and Kjaer (B&K) and made from Rochelle salt in 1943 in Denmark [51]. And to date, because of the advantages [52] of excellent linearity response, wide frequency range, compacted device size, and no external power required, piezoelectric accelerometers are widely adopted in variety commercial applications, including inertia navigator, seismic sensor, and shock pulse monitor. In principle, in order to measure acceleration, a mass (usually called seismic mass) with m weight has to be attached to the piezoelectric material. Therefore, when the velocity of the system changes, due to the inertia of the mass, it either compresses or stretches the piezoelectric material resulting in electrical signal that is linear to the inertia force. So, according to Newton's second law of motion, $F = ma$, by

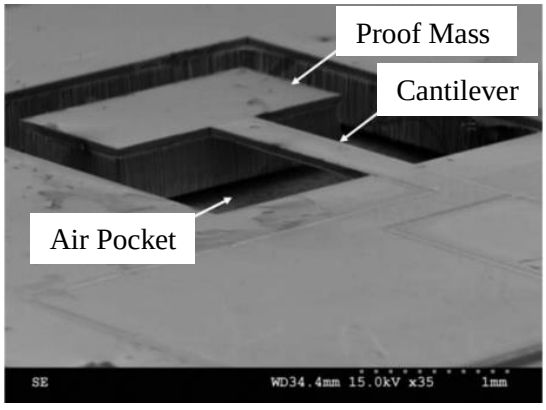

Figure 2-14. SEM image of Wong et al designed accelerometer, which is used to measure the acceleration perpendicular to the planar surface of the cantilever. Used with permission [53]

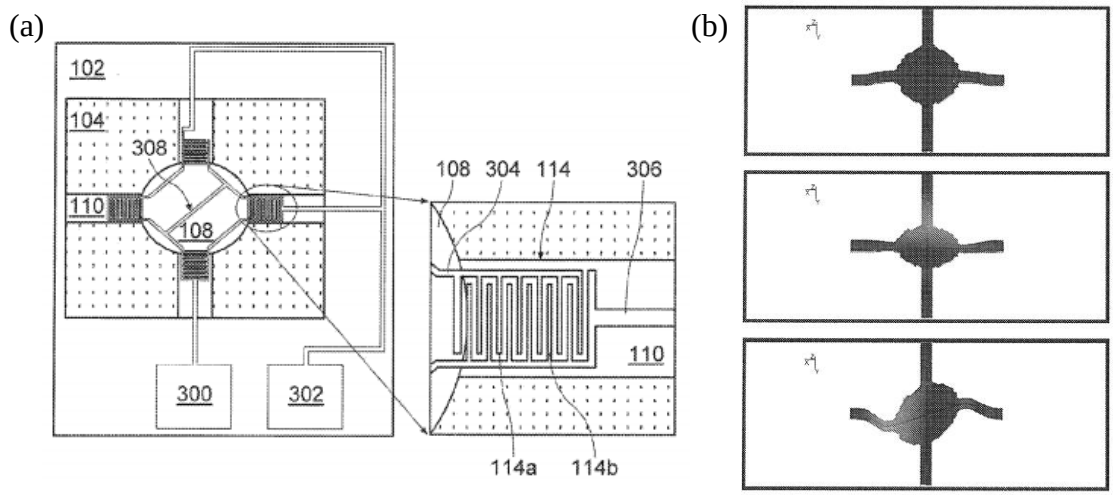

Figure 2-15. (a) The diagram of accelerometer for multi-directional accelerations sensing purpose. (b) The inertia of the mass results from acceleration will lead to deflection occurred in corresponded cantilevers and induces the electric signal. Used with permission [54]

measuring this force, the acceleration is able to obtained. There are generally two configurations of piezoelectric accelerometers. First is using single sensor to measure acceleration along single direction. For instance, Wong et al [53] designed a ZnO accelerometer as shown in Fig. 2-14. When the device is experiencing a vibration or acceleration perpendicular to the planar surface of the cantilever, the inertia of the mass will cause the bending of the cantilever and will lead to the electric signal generated from the ZnO that was coated on top of the cantilever. However, for most cases, the accelerations along multiple directions are needed. So multiple accelerometers are integrated into one single compact unit and form a multi-axis accelerometer. The second configuration is like this: a mass is centered and connected with multiple resilient soft cantilevers, where piezoelectric material is placed, along multiple directions. So this accelerometer can measure acceleration along different directions. In the year of 2014, Yao et al [54] reported an accelerometer patent, which used this configuration as shown in Fig. 2-15 (a). The seismic mass (108) is centered and supported by four cantilevers (110) of which piezoelectric thin films are coated on the top surface. And interdigitated electrodes (114) are utilized to structure the piezoelectric device as d_{33} mode for improving the sensitivity. When the acceleration is perpendicular to the device, the mass would be lifted or lowered resulting in all cantilevers bending. But if the acceleration is along the directions that are parallel to the device, rotation would occur at the mass and deflect corresponded cantilevers.

By detecting the output signal source and value, the direction and value of the acceleration can be obtained (Fig 2-15 (b))

2.3.3. Gyroscopes

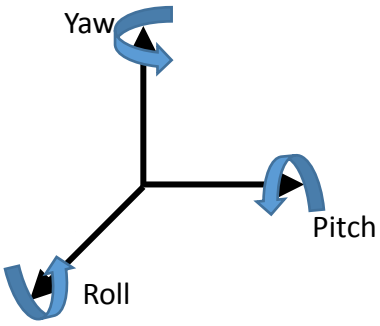

Figure 2-16. Roll, pitch, and yaw are the rotations along X, Y, and Z axis, respectively.

In order to complete a movement measurement of an object, besides the linear motion sensing using an accelerometer, rotation (pitch, yaw and roll determined as in Fig. 2-16) sensing is also required. The device that is used to detect the rotating speed is called gyroscope. Centrifugal, and Coriolis forces are playing significant roles in gyroscope. For any point in a rotating system, it is always exerted a centrifugal force. However, the Coriolis force will be activated only when this given point is experiencing relative motion to the rotating system. So according to this principle, the gyroscope is always vibrating at its resonant frequency (also known as driving mode). When the gyroscope is experiencing a rotation (also known as sensing mode), Coriolis force will be applied to the vibrated device since this vibration is the relative motion to the rotating system. So the piezoelectric material is able to sense this force and the rotation

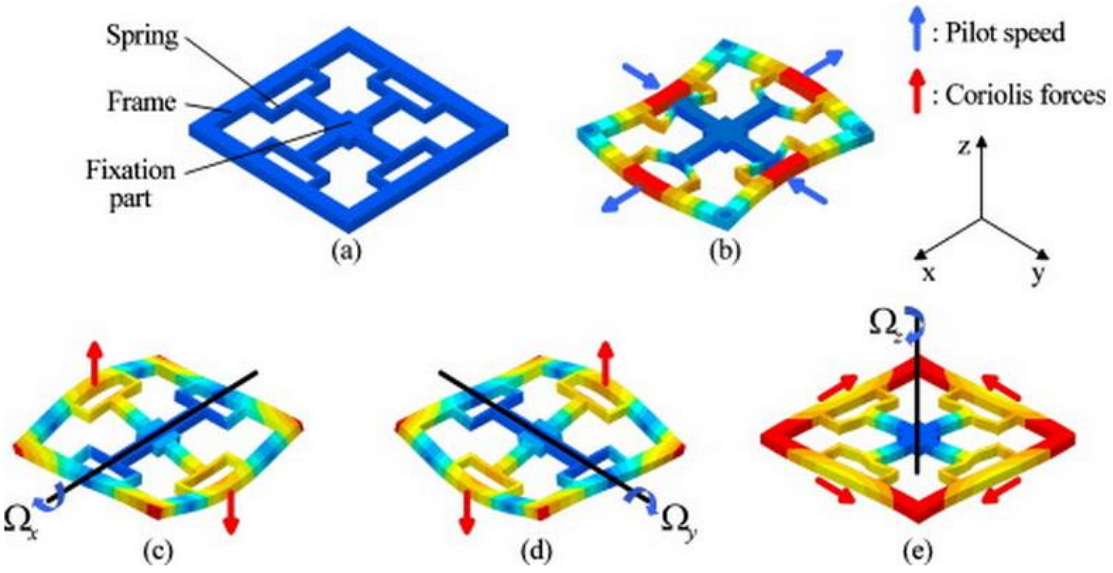

Figure 2-17. Simulation results of 3-axis Coriolis Vibrating Micro-Gyros: (a) structure layout, (b) driving mode, (c) X axis sensing mode, (d) Y axis sensing mode, (e) Z axis sensing mode. Used with permission [55]

speed can be calculated by $F_C = 2m\boldsymbol{\Omega} \times \boldsymbol{v}$ (F_C is the Coriolis force, m is the sensor weight, $\boldsymbol{\Omega}$ is the rotating speed of the system, $\boldsymbol{v}$ is the relative motion speed). Based upon it, Roland et al. presented a piezoelectric Coriolis vibrating gyroscope allowing the measurement of rotation rate along 3 orthogonal axes (Fig. 2-17) [55]. The frame and spring are all made of piezoelectric material (GaAs), sandwiched between top and bottom Au/Cr electrodes, and anchored to the center fixed element. During rotation, due to the extra motion on the sensing elements (e.g. motion towards z direction on beam 1 and 3 when rotating along x axis), deflection is occurred on related beams and generates electric signal. Such that the force is measured and rotating speed can be calculated.

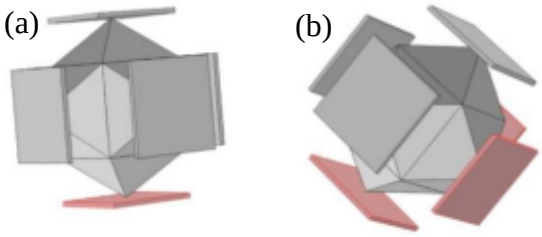

Figure 2-18. Simulation performed in COMSOL for different device positions. (a) For straightly placed device, the weight of the center mass is applied to the bottom plate. (b) While three plates are exerted force when the device is tilted. Used with permission [56]

Additionally, gravity is also utilizable when sensing pitch and roll. For instance, Madhuranath et al. simulated a piezoelectric gyroscope that only based on gravity as shown in Fig. 2-18 [56]. When the sensor is at the different angular position, the weight of the center mass is applied to different sensing plates (piezoelectric material). Therefore, by monitoring the force applied on all six sensing plates, the rotating angle of the sensor can be obtained, so as rotating speed.

2.3.4. Strain Gauges

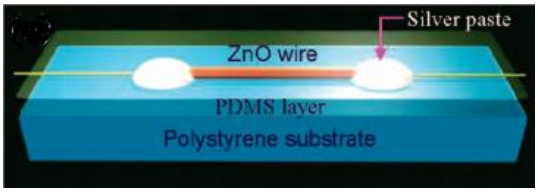

Figure 2-19. A ZnO nanowire piezoelectric surface strain sensor on the PDMS substrate. Used with permission [57]

Since strain is inherently associated with force, the piezoelectric strain gauges are actually force sensors. If a force sensor is attached to the structure that is undergoing the deformation, this deformation will yield a signal in the sensor that is proportional to the strain. According to the place where it is attached, piezoelectric strain gauges can be divided into two types. If the gauge is bonded to the surface of the structure, it is called surface strain gauge. For example, Zhou et al. [57] bonded ZnO nanowires on the PDMS-polystyrene flexible substrate (Fig. 2-19). When

the substrate is experiencing tensile strain, the ZnO nanowires are also strained and thereby generating correlated electric signal. On the other hand, if the gauge is embedded inside the host structure, it is called pin strain gauge.

2.4. Piezoelectric Energy Harvesters

With the development of MEMS, a power source that can provide stable, reliable and continuous energy to operate the systems is becoming indispensable. While most devices use a battery, this requires routine recharging or replacement. Therefore, a great amount of researches has been carried out on the energy harvesters as the self-power source. Electromagnetic, photovoltaic, and thermoelectric energy harvesters have been developed for different applications, such as wristwatches and solar panels. Piezoelectric effect provides an opportunity to leverage the mechanical energy from human body motion or the environment to power low energy required systems. This conversion method shows many advantages as a candidate of the micro energy harvester over other methods of conversion, such as greater output power density and simplicity of construction [58, 59].

2.4.1. d_{31} and d_{33} Modes

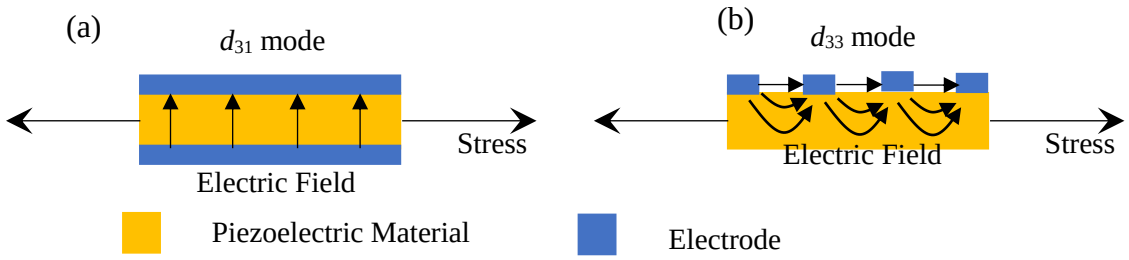

Figure 2-20. Two commonly used mode in piezoelectric energy harvesters. (a) d_{31} mode is the electric field direction perpendicular to the stress direction. While (b) d_{33} mode is these two directions are along the same axis.

Many methods have been reported to improve the harvested power by an energy harvester. One major method is by selecting a proper coupling mode of operation. Two modes are widely used for energy scavenging, namely d_{31} and d_{33}, as shown in Fig. 2-20. d_{31} mode is that the applied stress direction is perpendicular to the poling and induced charges direction (Fig. 2-20 (a)). So generally, the piezoelectric material is sandwiched between top and bottom electrodes and the stress is applied transversely. For instance, Shen et al. [60] designed and evaluated a d_{31} mode based piezoelectric vibration energy harvester

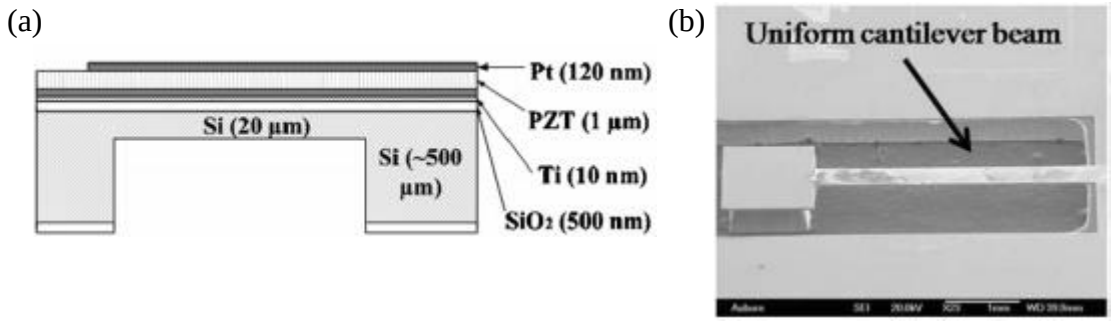

Figure 2-21. A d_{31} piezoelectric cantilever-shaped energy harvester. (a) A schematic of the side view of the energy harvester. The piezoelectric material was sandwiched between top and bottom electrode to form d_{31} mode. (b) SEM image shows the top view of the energy harvester. Used with permission [60]

as shown in Fig. 2-21. So when the cantilever is vibrating to bend, the direction of stress is along the cantilever surface. However, since the electrodes are placed top and bottom, the poling and induced charges directions are perpendicular to the cantilever, which is the stress direction. So this is a d_{31} mode energy harvester. Up to 2.15 μW was generated when connected the device with a 6 kΩ resistive load with applied $2g_a$ acceleration vibration (g_a = 9.81 N/m^2).

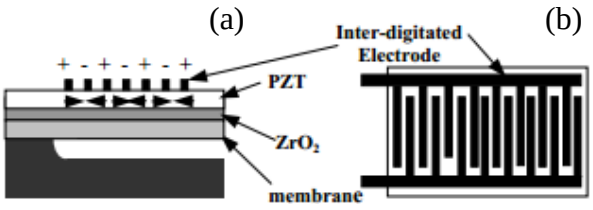

Figure 2-22. A d_{33} piezoelectric cantilever-shaped energy harvester. Interdigitated top electrode was used. So the electric field direction was the same as stress applied direction to form a d_{33} mode. The schematics of the (a) side and (b) top view of the energy harvester. Used with permission [61]

d_{33} mode is the mode in which the stress is applied on the same direction as the poling direction (Fig. 2-20 (b)). So d_{33} mode can be achieved by either using a top and bottom electrodes to sandwich the piezoelectric material, and applying a compressed pressure to the device; or using an interdigitated structure electrode on top of the piezoelectric film, and applying longitudinal stress to the device. Jeon et al. [61] designed a d_{33} mode piezoelectric energy harvester on a thin film cantilever (Fig. 2-22) with interdigitated electrode on top of piezoelectric material. It was demonstrated that up to 1 μW was delivered to a 5.2 MΩ load from the device under 13.7 kHz vibration frequency. Eq. 2-1 is showing the dominating equation of relation between the stress σ and generated open-circuit voltage (V) for these two modes

$$V_{3i} = \sigma g_{3i} L_i \tag{2-1}$$

where σ is the applied stress, g is the piezoelectric voltage constant and L is the distance between two electrodes. The subscript (i) can be 1 or 3 representing d_{31} or d_{33} mode, respectively. Because, for most piezoelectric materials, g_{33} (or d_{33}, piezoelectric charge constant) is generally 2 ~ 2.5 times higher than g_{31} (or d_{31}). Furthermore, the L_1 is limited by the thickness of the substrate, while L_3 can be easily designed and fabricated much larger. Therefore, d_{33} mode is able to produce higher voltage. Despite it, d_{31} is still commonly used due to simpler fabrication process. Nevertheless, Lee et al. [62] have demonstrated that the

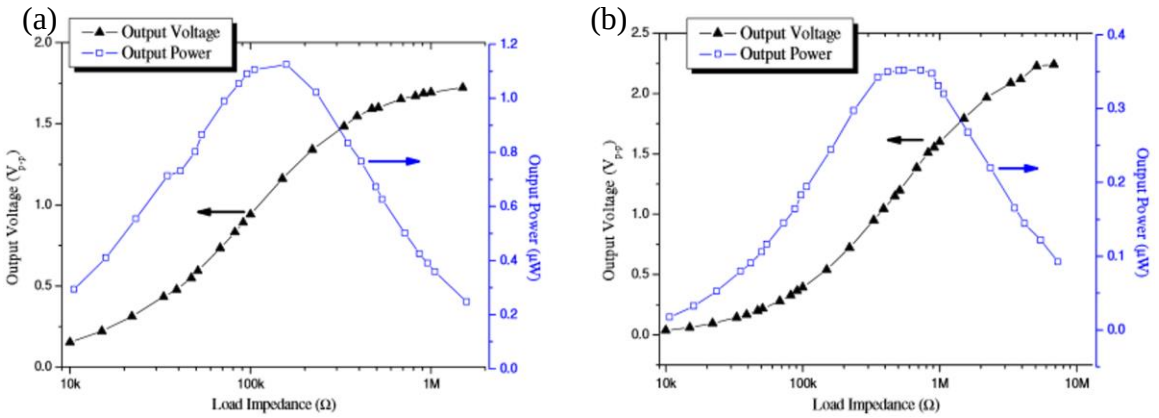

Figure 2-23. The output voltage and effective power with resistive load of Lee et al. designed (a) d31 and (b) d33 piezoelectric energy harvester. d33 mode can generate higher output voltage (~1.8 Vp-p V.S. ~2.3 Vp-p). However, d31 mode can generate higher effective power (~1.15 μW V.S. ~0.35 μW). Used with permission [62]

maximum output effective power of the d_{33} mode is lower than d_{31} mode for the same substrate, and piezoelectric material geometry and dimension (Fig. 2-23). Because the overlap area of two electrodes of d_{31} mode is much larger than d_{33} mode, while the distance is much shorter, resulting in higher capacitance and lower impedance. Therefore, the optimum load resistance of d_{31} mode is lower than d_{33} mode, and accordingly lower voltage can produce higher power on the lower optimal impedance.

2.4.2. Flexible Energy Harvesters

With the development of flexible electronics, the requirement of more practical applications, flexible energy harvesters have been extensively developed lately. In order to achieve good flexibility without weakening the piezoelectric response, both substrate and the piezoelectric material have to be flexible. PET (poly (ethylene terephthalate)), PDMS (Polydimethylsiloxane), KAPTON, were chosen as the substrate because of their good

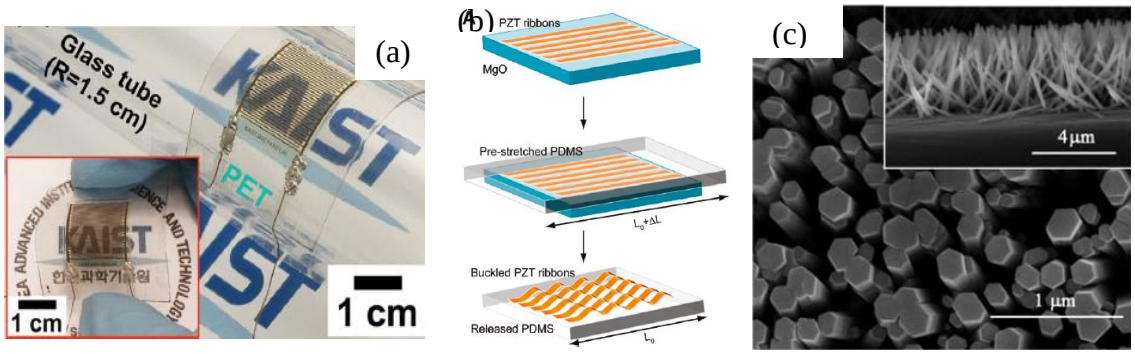

Figure 2-24. Both substrate and piezoelectric material are required to be flexible to achieve flexible energy harvester. (a) 2μm PZT film on PET substrate shows flexible and transparent. [63] (b) Formation of bulcked PZT ribbons on PDMS substrate. [64] (c) SEM images of top and side (inset) view of ZnO nanorods grown on a ZnO paper.Used with permission [65]. Figures are used with permission.

flexibility. For piezoelectric material, thin film and nano wires/rods/ribbons are two major candidates for flexible requirement. Park et al. [63] transferred a 2 μm thick PZT film on a PET substrate to realize a flexible energy harvester as shown in Fig. 2-24 (a) with high piezoelectric performance (12.24 μW generated power). Qi et al. [64] transferred an array of PZT ribbons from MnO substrate to pre-stretched PDMS substrate. After releaving the PDMS stress, the PZT ribbons were buckled up with high stretchebility and flexibility as shown in Fig. 2-24 (b). Up to 60 pA was generated from 10 ribbons when experiencing 8% strain. Qiu et al. [65] demonstrated that ZnO nanorods flexible energy harvester which was directly grew on a 0.4 cm × 0.8 cm ZnO paper can generate up to 10 mV output open-circuit voltage and 10 nA current (Fig. 2-24 (c)).

Because of the flexibility, the applications of piezoelectric energy harvester have been largely expanded. An increasing number of biomedical applications of flexible energy harvesters have been developed. Hwang et al. [66] designed a self-powered cardiac pacemaker enabled by a single crystalline (1-x) $Pb(Mg_{1/3}Nb_{2/3})O_3$ - x $PbTiO_3$ (PMN-PT) flexible energy harvester as shown in Fig. 2-25 (a). A real-time functional electrical stimulation was performed on a live rat using this energy harvester by bending and releasing the device to provide an artificial heart beating. The experimental results confirmed the function. Dagdeviren et al. [67] attached a flexible PZT ribbon energy harvester on bovine heart to convert the mechanical motion of heart to electric power to charge a cardiac pacemaker (Fig. 2-25 (b)). Flexible energy harvesters imbedded in shoes,

backpacks, knees/arms/fingers/ mounted bands have also been designed and demonstrated for powering biomedical sensors. [68-70]

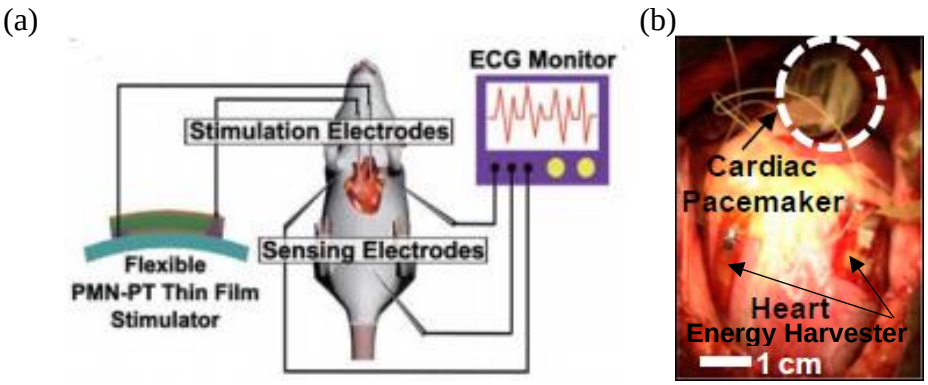

Figure 2-25. Flexible piezoelectric energy harvesters used for biomedical applications. (a) A schematic of the artificial cardiac pacemaker using electrical energy from the flexible PMN-PT energy harvester [66]. (b) PZT energy harvester was attached on the bovine heart to convert the heart beat to electric energy to power a cardiac pacemaker [67]. Figures are used with permission.

2.5. Conclusions

Three major members of piezoelectric transducers, namely actuators, sensors, and energy harvesters are introduced in this chapter.

The piezoelectric actuators take advantage of the inverse piezoelectric effect to convert the electric power into mechanical deformation to obtain the displacement. Piezoelectric actuators are widely used due to its high precision, large force generation, fast response time, small size and thermal expansion during actuation. Two commonly used configurations in the piezoelectric actuators, cantilever shape and membrane shape, are introduced in associate with the device examples. However, the major drawback of the piezoelectric actuators is their accuracy because of the ferroelectric hysteresis loop. Therefore, few solutions to overcome or reduce the impact from it are also provided according to the literature.

Piezoelectric sensors are another widely used piezoelectric device. Basically, piezoelectric sensors are only measuring the dynamic or quasi-static force. However, based upon the designs, piezoelectric force sensors can be expanded to other force related parameters sensing applications, such as pressure sensors, strain sensors, accelerometers,

and so forth. Four types of sensors in associate with the characteristics are presented in this chapter.

Piezoelectric energy harvester is the third major member of piezoelectric transducer. Two popularly used coupling modes of operation, d_{31} and d_{33}, are also presented in this chapter with few biomedical applications.

The PZT devices are either built on the high-temperature substrates, such as silicon, sapphire, and MgO, or constructed via complex film transfer method to realize the flexible device on low-temperature substrates. There is a need to process piezoelectric material directly on low-temperature substrates, which motivated this work.

References:

[1] *Adhesion Measurement of Thin FIlms, Thick Films, and Bulk Coatings*. Philadelphia, Pennsylvania: American Society for Testing and Materials, 1978.

[2] M. G. Joshi, *Compr. Transducers for Instrumentation*: Laxmi Publications, 2005.

[3] J. Ouyang and Y. Zhu, "Z-shaped MEMS thermal actuators: Piezoresistive self-sensing and preliminary results for feedback control," *Microelectromechanical Systems, Journal of,* vol. 21, pp. 596-604, 2012.

[4] Q.-A. Huang and N. K. S. Lee, "Analysis and design of polysilicon thermal flexure actuator," *Journal of Micromechanics and Microengineering,* vol. 9, p. 64, 1999.

[5] L. Que, J.-S. Park, and Y. B. Gianchandani, "Bent-beam electrothermal actuators-Part I: Single beam and cascaded devices," *Microelectromechanical Systems, Journal of,* vol. 10, pp. 247-254, 2001.

[6] R. Legtenberg, A. Groeneveld, and M. Elwenspoek, "Comb-drive actuators for large displacements," *Journal of Micromechanics and Microengineering,* vol. 6, p. 320, 1996.

[7] W. C. Tang, T.-C. H. Nguyen, M. W. Judy, and R. T. Howe, "Electrostatic-comb drive of lateral polysilicon resonators," *Sensors and Actuators A: Physical,* vol. 21, pp. 328-331, 1990.

[8] D. Horsley, N. Wongkomet, R. Horowitz, and A. P. Pisano, "Precision positioning using a microfabricated electrostatic actuator," *IEEE Transactions on Magnetics,* vol. 35, pp. 993-999, 1999.

[9] *Introduction to Piezo Positioning Technology*. Available: http://www.pi-usa.us/tutorial/4_4.html

[10] J.-L. Ha, Y.-S. Kung, R.-F. Fung, and S.-C. Hsien, "A comparison of fitness functions for the identification of a piezoelectric hysteretic actuator based on the real-coded genetic algorithm," *Sensors and Actuators A: Physical,* vol. 132, pp. 643-650, 2006.

[11] R. Changhai and S. Lining, "Hysteresis and creep compensation for piezoelectric actuator in open-loop operation," *Sensors and Actuators A: Physical,* vol. 122, pp. 124-130, 2005.

[12] R. Maeda, J. Tsaur, S. Lee, and M. Ichiki, "Piezoelectric microactuator devices," *Journal of Electroceramics,* vol. 12, pp. 89-100, 2004.

[13] Y. Haddab, N. Chaillet, and A. Bourjault, "A microgripper using smart piezoelectric actuators," in *Intelligent Robots and Systems, 2000.(IROS 2000). Proceedings. 2000 IEEE/RSJ International Conference on*, 2000, pp. 659-664.

[14] M. Sitti, D. Campolo, J. D. YAN, and R. S. Fearing, "Development of PZT and PZN-PT based unimorph actuators for micromechanical flapping mechanisms," in *Robotics and Automation, 2001. Proceedings 2001 ICRA. IEEE International Conference on*, 2001, pp. 3839-3846.

[15] S. J. Gross, "Micromachined switches and cantilever actuators based on piezoelectric lead zirconate titanate (PZT)," The Pennsylvania State University, 2004.

[16] M. Taya, A. A. Almajid, M. Dunn, and H. Takahashi, "Design of bimorph piezo-composite actuators with functionally graded microstructure," *Sensors and Actuators A: Physical,* vol. 107, pp. 248-260, 2003.

[17] J. H. Yoo, J. I. Hong, and W. Cao, "Piezoelectric ceramic bimorph coupled to thin metal plate as cooling fan for electronic devices," *Sensors and Actuators A: Physical,* vol. 79, pp. 8-12, 2000.
[18] J. G. Smits, S. I. Dalke, and T. K. Cooney, "The constituent equations of piezoelectric bimorphs," *Sensors and Actuators A: Physical,* vol. 28, pp. 41-61, 1991.
[19] Y. Bai, J. T. Yeow, P. Constantinou, S. Damaskinos, and B. C. Wilson, "A 2-D micromachined SOI MEMS mirror with sidewall electrodes for biomedical imaging," *IEEE/ASME Transactions on Mechatronics,* vol. 15, pp. 501-510, 2010.
[20] U. Krishnamoorthy, K. Li, K. Yu, D. Lee, J. Heritage, and O. Solgaard, "Dual-mode micromirrors for optical phased array applications," *Sensors and Actuators A: Physical,* vol. 97, pp. 21-26, 2002.
[21] R. A. Conant, P. M. Hagelin, U. Krishnamoorthy, M. Hart, O. Solgaard, K. Y. Lau, and R. S. Muller, "A raster-scanning full-motion video display using polysilicon micromachined mirrors," *Sensors and Actuators A: Physical,* vol. 83, pp. 291-296, 2000.
[22] W. Liu, Y. Zhu, K. Jia, W. Liao, Y. Tang, B. Wang, and H. Xie, "A tip–tilt–piston micromirror with a double S-shaped unimorph piezoelectric actuator," *Sensors and Actuators A: Physical,* vol. 193, pp. 121-128, 2013.
[23] Y.-S. Kim, H.-J. Nam, S.-M. Cho, J.-W. Hong, D.-C. Kim, and J. U. Bu, "PZT cantilever array integrated with piezoresistor sensor for high speed parallel operation of AFM," *Sensors and Actuators A: Physical,* vol. 103, pp. 122-129, 2003.
[24] A. Daniele, S. Salapaka, M. Salapaka, and M. Dahleh, "Piezoelectric scanners for atomic force microscopes: Design of lateral sensors, identification and control," in *American Control Conference, 1999. Proceedings of the 1999,* 1999, pp. 253-257.
[25] K. K. Leang and S. Devasia, "Feedback-linearized inverse feedforward for creep, hysteresis, and vibration compensation in AFM piezoactuators," *Control Systems Technology, IEEE Transactions on,* vol. 15, pp. 927-935, 2007.
[26] W. Spencer, W. T. Corbett, L. Dominguez, and B. D. Shafer, "An electronically controlled piezoelectric insulin pump and valves," *Sonics and Ultrasonics, IEEE Transactions on,* vol. 25, pp. 153-156, 1978.
[27] X. Wang, Z. Zhou, X. Ye, Y. Li, and W. Zhang, "A PZT-driven micropump," in *Micromechatronics and Human Science, 1998. MHS'98 Nagoya, Proceedings of the 1998 International Symposium on*, 1998, pp. 269-272.
[28] H. Van Lintel, F. Van de Pol, and S. Bouwstra, "A piezoelectric micropump based on micromachining of silicon," *Sensors and actuators,* vol. 15, pp. 153-167, 1988.
[29] T. T. Nguyen and N. S. Goo, "A novel PDMS valveless micropump with a circular lightweight piezo-composite actuator," in *Key Engineering Materials*, 2006, pp. 245-248.
[30] J. Kan, Z. Yang, T. Peng, G. Cheng, and B. Wu, "Design and test of a high-performance piezoelectric micropump for drug delivery," *Sensors and Actuators A: Physical*, vol. 121, pp. 156-161, 2005.
[31] C.-C. Lee, Q. Guo, G. Cao, and I. Shen, "Effect of electrode size and silicon residue on piezoelectric thin-film membrane actuators," *Sensors and Actuators A: Physical,* vol. 147, pp. 279-285, 2008.

[32] H. Ma, B. Hou, H. Wu, C. Lin, J. Gao, and M. Kou, "Development and application of a diaphragm micro-pump with piezoelectric device," *Microsystem Technologies,* vol. 14, pp. 1001-1007, 2008.
[33] G.-H. Feng and E. S. Kim, "Piezoelectrically actuated dome-shaped diaphragm micropump," *Journal of Microelectromechanical Systems,* vol. 14, pp. 192-199, 2005.
[34] Z. Zhang, J. Kan, G. Cheng, H. Wang, and Y. Jiang, "A piezoelectric micropump with an integrated sensor based on space-division multiplexing," *Sensors and Actuators A: Physical,* vol. 203, pp. 29-36, 2013.
[35] J. Brünahl and A. M. Grishin, "Piezoelectric shear mode drop-on-demand inkjet actuator," *Sensors and Actuators A: Physical,* vol. 101, pp. 371-382, 2002.
[36] V. S. Vishnevsky, V. L. Kavertsev, I. A. Kartashev, V. V. Lavrinenko, M. M. Nekrasov, and A. A. Prez, "Piezoelectric motor structures," ed: Google Patents, 1977.
[37] S. Dong, S. P. Lim, K. H. Lee, J. Zhang, L. C. Lim, and K. Uchino, "Piezoelectric ultrasonic micromotor with 1.5 mm diameter," *IEEE Transactions on Ultrasonics, Ferroelectrics, and Frequency Control,* vol. 50, pp. 361-367, 2003.
[38] T. Morita, M. Kurosawa, and T. Higuchi, "An ultrasonic micromotor using a bending cylindrical transducer based on PZT thin film," *Sensors and Actuators A: Physical,* vol. 50, pp. 75-80, 1995.
[39] A. M. Flynn, L. S. Tavrow, S. F. Bart, R. Brooks, D. J. Ehrlich, K. Udayakumar, and L. E. Cross, "Piezoelectric micromotors for microrobots," *Journal of Microelectromechanical Systems,* vol. 1, pp. 44-51, 1992.
[40] G. Gautschi, "Piezoelectric Sensorics: force, strain, pressure, acceleration and acoustic emission sensors, materials and amplifiers. 2002," ed: Berlin, 2002.
[41] J. Thomson, "Piezo-Electricity and Its Application," *Scientific American,* vol. 87, pp. 412-413, 1919.
[42] J. Irish and F. Snodgrass, "Quartz crystals as multipurpose oceanographic sensors—I. Pressure," in *Deep Sea Research and Oceanographic Abstracts*, 1972, pp. 165-169.
[43] M. Eble and F. Gonzalez, "Deep-ocean bottom pressure measurements in the northeast Pacific," *Journal of Atmospheric and Oceanic Technology,* vol. 8, pp. 221-233, 1991.
[44] G. Park, H. Sohn, C. R. Farrar, and D. J. Inman, "Overview of piezoelectric impedance-based health monitoring and path forward," 2003.
[45] L. Seminara, M. Capurro, P. Cirillo, G. Cannata, and M. Valle, "Electromechanical characterization of piezoelectric PVDF polymer films for tactile sensors in robotics applications," *Sensors and Actuators A: Physical,* vol. 169, pp. 49-58, 2011.
[46] E. S. Kolesar Jr and C. S. Dyson, "Object imaging with a piezoelectric robotic tactile sensor," *Journal of Microelectromechanical Systems,* vol. 4, pp. 87-96, 1995.
[47] Available: http://www.ammonit.com/
[48] A. Kuoni, R. Holzherr, M. Boillat, and N. F. de Rooij, "Polyimide membrane with ZnO piezoelectric thin film pressure transducers as a differential pressure liquid flow sensor," *Journal of Micromechanics and Microengineering,* vol. 13, p. S103, 2003.

[49] C. Dagdeviren, Y. Su, P. Joe, R. Yona, Y. Liu, Y.-S. Kim, Y. Huang, A. R. Damadoran, J. Xia, and L. W. Martin, "Conformable amplified lead zirconate titanate sensors with enhanced piezoelectric response for cutaneous pressure monitoring," *Nature communications,* vol. 5, 2014.

[50] A. Shirinov and W. Schomburg, "Pressure sensor from a PVDF film," *Sensors and Actuators A: Physical,* vol. 142, pp. 48-55, 2008.

[51] P. L. Walter, "Review: Fifty years plus of accelerometer history for shock and vibration (1940–1996)," *Shock and Vibration,* vol. 6, pp. 197-207, 1999.

[52] J. B. Johannes Wagner. (2012, Piezoelectric Accelerometers: Theory and Application. Available: http://www.mmf.de/manual/transducermane.pdf

[53] Y.-R. Wong, Y. Yuan, H. Du, and X. Xia, "Development of high sensitivity, large frequency bandwidth ZnO-based accelerometers," *Sensors and Actuators A: Physical,* vol. 229, pp. 23-29, 2015.

[54] K. Yao, S. Shanmugavel, T. D. Luong, A. S. Gaunekar, and H. Y. P. Ng, "Miniaturized piezoelectric accelerometers," ed: Google Patents, 2014.

[55] I. Roland, S. Masson, O. Ducloux, O. Le Traon, and A. Bosseboeuf, "GaAs-based tuning fork microresonators: A first step towards a GaAs-based Coriolis 3-axis micro-vibrating rate gyro (GaAs 3-axis μCVG)," *Sensors and Actuators A: Physical,* vol. 172, pp. 204-211, 2011.

[56] R. Praharsha. T. Madhuranath, and K. S. Rao, "Design and simulation of MEMS piezoelectric gyroscope using COMSOL multiphysics," in *Proceedings of the 2013 COMSOL Conference*, Bangalore, India, 2013.

[57] J. Zhou, Y. Gu, P. Fei, W. Mai, Y. Gao, R. Yang, G. Bao, and Z. L. Wang, "Flexible piezotronic strain sensor," *Nano letters,* vol. 8, pp. 3035-3040, 2008.

[58] H. A. Sodano, D. J. Inman, and G. Park, "A review of power harvesting from vibration using piezoelectric materials," *Shock and Vibration Digest,* vol. 36, pp. 197-206, 2004.

[59] S. R. Anton and H. A. Sodano, "A review of power harvesting using piezoelectric materials (2003–2006)," *Smart materials and Structures,* vol. 16, p. R1, 2007.

[60] D. Shen, J.-H. Park, J. Ajitsaria, S.-Y. Choe, H. C. Wikle III, and D.-J. Kim, "The design, fabrication and evaluation of a MEMS PZT cantilever with an integrated Si proof mass for vibration energy harvesting," *Journal of Micromechanics and Microengineering,* vol. 18, p. 055017, 2008.

[61] Y. Jeon, R. Sood, L. Steyn, and S.-G. Kim, "Energy harvesting MEMS devices based on d33 mode piezoelectric Pb (Zr, Ti) O3 thin film cantilever," in *CIRP Seminar on Micro and Nano Technology*, 2003.

[62] B.-S. Lee, S.-C. Lin, and W.-J. Wu, "Comparison of the piezoelectric MEMS generators with interdigital electrodes and laminated electrodes," in *The 15th International Symposium on: Smart Structures and Materials & Nondestructive Evaluation and Health Monitoring*, 2008, pp. 69331B-69331B-8.

[63] K. I. Park, J. H. Son, G. T. Hwang, C. K. Jeong, J. Ryu, M. Koo, I. Choi, S. H. Lee, M. Byun, and Z. L. Wang, "Highly‐Efficient, Flexible Piezoelectric PZT Thin Film Nanogenerator on Plastic Substrates," *Advanced Materials,* vol. 26, pp. 2514-2520, 2014.

[64] Y. Qi, J. Kim, T. D. Nguyen, B. Lisko, P. K. Purohit, and M. C. McAlpine, "Enhanced piezoelectricity and stretchability in energy harvesting devices fabricated from buckled PZT ribbons," *Nano letters,* vol. 11, pp. 1331-1336, 2011.
[65] Y. Qiu, H. Zhang, L. Hu, D. Yang, L. Wang, B. Wang, J. Ji, G. Liu, X. Liu, and J. Lin, "Flexible piezoelectric nanogenerators based on ZnO nanorods grown on common paper substrates," *Nanoscale,* vol. 4, pp. 6568-6573, 2012.
[66] G. T. Hwang, H. Park, J. H. Lee, S. Oh, K. I. Park, M. Byun, H. Park, G. Ahn, C. K. Jeong, and K. No, "Self‐Powered Cardiac Pacemaker Enabled by Flexible Single Crystalline PMN‐PT Piezoelectric Energy Harvester," *Advanced Materials,* vol. 26, pp. 4880-4887, 2014.
[67] C. Dagdeviren, B. D. Yang, Y. Su, P. L. Tran, P. Joe, E. Anderson, J. Xia, V. Doraiswamy, B. Dehdashti, and X. Feng, "Conformal piezoelectric energy harvesting and storage from motions of the heart, lung, and diaphragm," *Proceedings of the National Academy of Sciences,* vol. 111, pp. 1927-1932, 2014.
[68] H. S. Kim, J.-H. Kim, and J. Kim, "A review of piezoelectric energy harvesting based on vibration," *International Journal of precision engineering and manufacturing,* vol. 12, pp. 1129-1141, 2011.
[69] B. Yang and K.-S. Yun, "Piezoelectric shell structures as wearable energy harvesters for effective power generation at low-frequency movement," *Sensors and Actuators A: Physical,* vol. 188, pp. 427-433, 2012.
[70] Y. Qi and M. C. McAlpine, "Nanotechnology-enabled flexible and biocompatible energy harvesting," *Energy & Environmental Science,* vol. 3, pp. 1275-1285, 2010.

Chapter 3 Fabrication of PZT Film

3.1. Introduction

PZT has been extensively used in MEMS (microelectromechanical systems) devices due to its high piezoelectric response [1-3]. Generally, the PZT powders are formed by sol-gel method from Zirconium, Titanium, and Lead alkoxides. In order to form a PZT film, three key steps are required, i.e. deposition, sintering, and poling. Deposition is the first step of the film fabrication, which is used to form a PZT green body layer with desired thickness on a substrate. To meet the thickness requirements, different deposition methods have been developed, such as spin-coating, sputtering, and screen printing. This work adopted aerosol-jet printing technique to realize the PZT film deposition. Sintering is needed to densify the layer by fusing and merging the particles to enhance the film elastic properties. Generally, the sintering is a high temperature (> 1000 °C) process with a sufficiently long duration (> 0.5 hr). However, for some applications (e.g. flexible and stretchable PZT energy harvesters), to prevent the low-temperature substrate from burning and accordingly loose the properties, the substrate temperature increase has to be maintained sufficiently low. Therefore, many methods, like laser sintering, and adding sintering aids, have been employed to lower the film sintering temperature. The photonic sintering approach using pulsed high energy flashes to sinter PZT film is proposed in the work, for the first time, to sinter PZT film. During sintering, a low substrate temperature increase was obtained. Poling step is critical and indispensable to enhance piezoelectric property for the ferroelectric material, because the unpoled ferroelectric film shows low or even zero net polarization to lower the free energy and reach the equilibrium state. Poling is using high electric field in sufficient duration to reorient domains along the applied DC electric field direction to enhance the piezoelectric property. This chapter mainly focuses

on the approaches to realize these three steps and the new PZT aerosol-jet printing and photonic sintering approaches.

3.2. Established Fabrication Methods

3.2.1. PZT Film Deposition

PZT film formation is the first step of creating a PZT device. It is necessary to form a uniform film with the desired thickness and patterns at an expected location according to the devices' applications. Various built reliable deposition approaches have been employed for forming a PZT film.

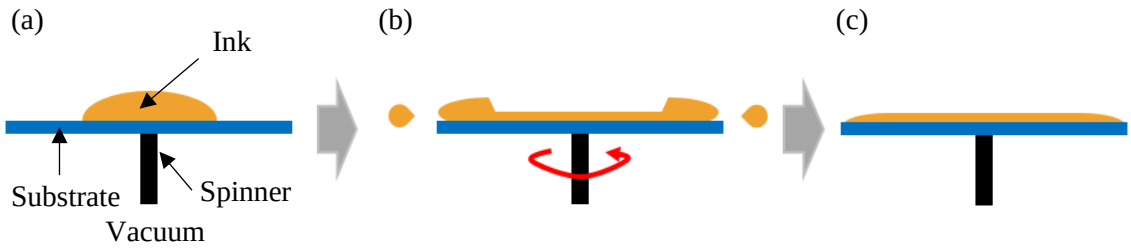

Figure 3-1. The procedure of spin coating step. (a) A small amount of ink is dispersed at the center of the substrate which is adhered to the spinner by vacuum. (b) The spinner starts to rotate. The centrifugal force spreads the ink out and makes the ink coated on the substrate. (c) The spinner keeps spinning to uniform the ink on the substrate.

Spin coating is one of the most common techniques to create a thin film on the flat surface. It can produce a uniform and evenly distributed film with, generally, nanometer thickness quickly and easily. Figure 3-1 shows the typical procedure of spin coating. The tool used for spin coating is called spin coater (or spinner), which is used to provide high rotation speed. A substrate is placed on the spinner and is held by a high vacuum during spinning. Usually a small amount of spinning material (sol-gel or ink) is dispersed at the center of the substrate (Fig. 3-1 (a)). Then the spinner is rotating to spread out the material on the substrate by centrifugal force (Fig. 3-1 (b)). The thickness of the coated film is

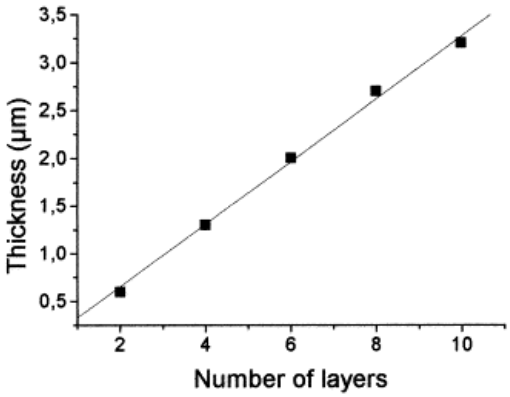

Figure 3-2. The thickness of a PZT film as a function of the number of spin coated layers on a stainless steel substrate. Used with permission [4]

mainly controlled by the spinning speed and the viscosity of the spinning material. The spinning speed will be kept for a while (generally shorter than 1 min) to further spread the ink and to uniform the film (Fig. 3-1 (c)). Because of its consistence and repeatability, thick films can be created by repeating the spinning process. For instance, Seveno et al. studied, at 6000 rpm spinning speed level during 20 s, the relation of number of coated PZT layers and thickness (Fig. 3-2) [4]. However, spin coating is a "single substrate" process to coat the entire surface of the substrate with the ink. Subsequent processing steps (masking, etching, etc.) are required to realize design features. In addition, most of ink is flung off the substrate and wasted during high speed rotation, the ink utilization is typically very low (around 10% or less). Additionally, it is not quite suitable for powder-based solution. Because the powders in the solution can be more easily spread out than the solvent due to heavier weight. It results in more powders are either flung out or left at the edge of the substrate. The powder uniformity and density in the film is relatively low.

Sputtering is another widely used thin film deposition approach. The film is formed due to the bombardment of a solid target by energetic particles (ions, electrons, etc.). Therefore, many atoms are ejected from the solid target due to the momentum exchange between incident energetic particles and bombarded target atoms. The ejected atoms are deposited on the substrate to form a thin film (Fig. 3-3) [5]. Sputtering method is able to provide better step coverage than spin coating. And reproducible deposition rate can be achieved using same process parameters and accordingly results in good thickness control over time. Bouregba et al. used sputtering approach to build a 150 nm thick PZT film in 0.5 hr [6]. While providing excellent control over film thickness and good reproducibility, sputtering rate is quite low and thereby it is only suitable for thin films.

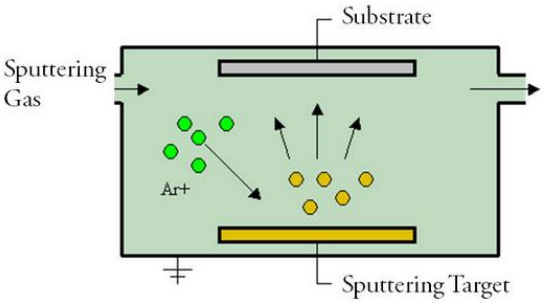

Figure 3-3. The diagram of sputtering process. Sputtering gas (Ar) is ionized and energized to a target. Then the energetic ions bombard the target causing ejection of the target material that is coated on the substrate. Used with permission [5]

Pulsed laser deposition is a chemical vapor deposition method developed over a decade. The high energy pulsed laser beam is focused to the target and used to melt,

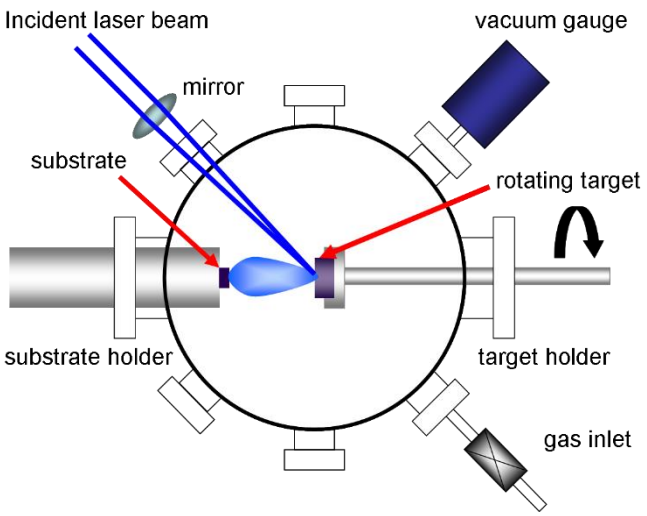

Figure 3-4. The pulsed laser deposition setup. Used with permission [7].

evaporate, and ionized the target material from the surface. The vaporized target ablation is deposited onto the substrate to form a thin layer and kept growing until desired thickness is achieved. The process is shown in the Fig. 3-4. This process can be occurred in both vacuum or specific gas environment (even air). Typical deposition rate is ~ 10s nm/min, plus the real time thickness control by simply turning the laser on and off, resulting in finely controlled thickness [8]. The substrate holder generally can be heated enabling multilayer films to be deposited without the need to remove the substrate after each layer deposition for thermal process (such as annealing or sintering) [8]. Horwitz et al. [9] developed pulsed laser deposition method and applied to PZT deposition, which yielded ~1μm thick PZT film using 5000 laser pulses.

Additive manufacturing is attracting considerable attentions due to its easy operation, cost effectiveness, and scalability. Therefore, many additive manufacturing deposition methods have been developed for PZT deposition, such as screen printing and ink-jet printing.

Screen printing is the most popular and traditional method for building thick PZT films. This technique requires creating designed features on a stencil that is placed under a screen. During printing, as shown in Fig. 3-5 [10], the material paste is forced by a squeegee through the fine mesh openings of the screen and transferred onto the substrate to form the features that are created on the stencil. The thickness of the film is dominated by the mesh size. Screen printing is one of the easiest methods for creating large size features without material limitation for the substrate. Maas et al. applied this method to create a 50 μm thick PZT film on a silicon substrate [11]. However, this technique also has many limitations. Different stencils are required when different designs are needed. Furthermore, the minimum printed feature size is limited to approximately 100 μm and alignment accuracy

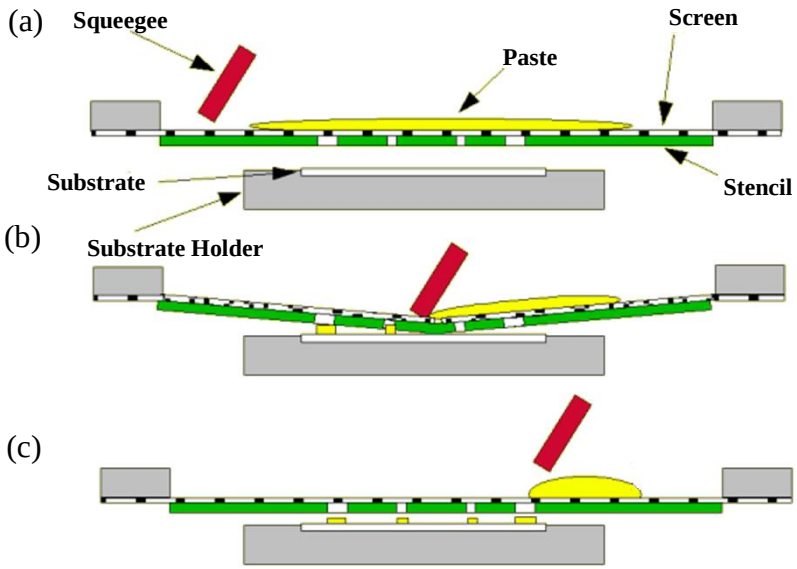

Figure 3-5. The diagram of screen printing process. (a) Paste is placed onto the top of the screen. (b) When the squeegee is applying pressure to force the ink passed through the mesh openings and transferred down to the underneath substrate. (c) After relieving the squeegee, the transferred paste left on the substrate. Used with permission [10]

is ±50 μm [12]. In addition, the film thickness is controlled by the screen mesh size that cannot be changed. Additionally, the screen has to be carefully cleaned to avoid the mesh clog and film contamination when next use.

Ink-jet printing has emerged as an alternate method of directly creating the desired design features (film and bulk). The material ink is stored in a cartridge that is installed on an ink-jet printer. During printing, ink is propelled through an orifice of the nozzle and formed fine droplets. These droplets are deposited onto the substrate to form the film. The printed film thickness can be controlled by the printing speed and the applied propelling force. Okamura et al. [13] used ink-jet printing technique to prepare PZT thin films with different Zr/Ti ratio and studied the properties of these PZT films. Wang et al. [14] demonstrated high loading fraction PZT suspension (40%) was able to be continuously ink-jet printed to form a bulk object without clogging the nozzle. Although ink-jet printing can provide direct feature writing, variability in droplet size limits its minimum feature sizes to approximately 20 μm [15]. Due to the size limitation of the nozzle orifice, only very fine particle inks are accepted for printing.

Aerosol-jet printing technique for PZT deposition is used in this work. The Aerosol Jet printer (Optomec, Inc., USA) is a maskless, CAD driven, non-contact printing system to deposit inks such as the PZT inks used in this research. The Aerosol Jet printer is able to precisely print inks having a wide viscosity range (1-1000 cP) onto almost any substrate including non-planar substrates. The printed film thickness can range from 100's of nanometers to 10's of millimeters depending upon the ink formulation and printing speed. The minimum achievable feature resolution is approximately 10 μm [16].

The described deposition methods are summarized in the Table 3-1 with the strengths and weaknesses.

Table 3-1. Deposition methods with the strengths and weaknesses.

Deposition Method	Strengths	Weaknesses
Spin Coating	Easy to operate. Short processing duration. Enable to realize a wide range of film thickness (nm to μm).	"Single substrate" process, for the specific size and feature requirements, subsequent processes are needed. Low ink usage rate.
Sputtering	Good repeatability. Well thickness control over time.	Low deposition rate, thus only suitable for thin film. For specific size and feature requirements, mask or post processes are needed.
Pulsed Laser Deposition	Good repeatability. Real time thickness control. Easy for multilayer films realization.	Low deposition rate, thus only suitable for thin film. For specific size and feature requirements, mask or post processes are needed.

Deposition Method	Strengths	Weaknesses
Screen Printing	Easy operation. Short processing duration. Direct realization of the features.	Low resolution. Different stencils are required for different designs.
Ink-Jet Printing	Easy to make changes to the design. Direct realization of the features. Short processing duration. Wide range of printed film thickness (depending on the ink property)	Different cartridges are required for different inks. Long processing time for large features. Short range of printable ink viscosity (up to 20 cP)
Aerosol-Jet Printing	Easy to make changes to the design. Direct realization of the features. Short processing duration. Wide range of printed film thickness (depending on the ink property). Wide range of printable ink viscosity (up to 1000 cP). Can print on non-planar substrate. High printing speed.	Splatters affect the feature resolution.

3.2.2. PZT Film Sintering

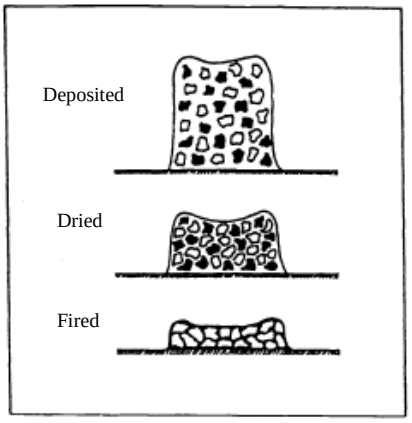

Figure 3-6. The sintering further dries the film and burns the organic products out. Particles fuse and merge together at high sintering temperature. Used with permission [17]

In order to densify the deposited film, enhance the mechanical properties of the PZT film, sintering process has to be performed after deposition (and drying). During the sintering process, the PZT particles fuse and merge together to form a high density film as shown in Fig. 3-6 [17]. Generally, the sintering temperature of PZT is higher than 1000 °C for a long period of time. For instance, Sangsubun et al. [18] sintered PZT powders at 1200 °C for 4 hr to obtain a highly densified film with approximately 96% relative density to the theoretical value. However, at such a high temperature, several issues may occur to weaken the PZT film mechanical and piezoelectric properties. Firstly, oxidization of the substrate is one of the most severe issues. Therefore, inert gases (e.g. Argon) are used to create oxygen-free environment. Moreover, those materials that are not easily oxidized, such as SiO_2 and Pt/Ti, are generally chosen as the substrate to further eliminate oxidization. Secondly, Lead tends to lose through the release of PbO vaporization during high-temperature (>850 °C) processing [19]. Therefore, extra amount of Pb or PbO is necessary to compensate the loss. Furthermore, the permeation and reaction may happen between Lead and the Silicon substrate. So insulator layer is generally required to isolate PZT and the Si substrate. Additionally, size shrinkage occurs during sintering (especially in thick PZT films) due to the removal of organic products and particles merge. This shrinkage would result in cracks in the film and hence weaken the piezoelectric property.

Because of aforementioned issues, performing a high temperature sintering is complicated, time consuming, and problematic for some applications. Several relatively lower temperature and shorter duration sintering methods have been developed.

A popular method to lower the sintering temperature of the PZT film is adding sintering aid. It has been demonstrated that the sintering temperature can be dramatically reduced to approximately 800 °C by adding liquid phase sintering aid [20]. Sintering aid is playing two roles during sintering. On the one hand, it is performed as a lubricant to reorient

the particles in the film to a better degree of merging. On the other hand, sintering aid acts as a diffusion path for the PZT particles to encourage dissolution and reprecipitation of the particles. Therefore, it accelerates the densification process. Many chemicals have been reported as the sintering aids, such as PbO [21], $Pb_5Ge_3O_{11}$ [22], and $LiBiO_2$-CuO [23].

Microwave sintering method was developed to shorten the sintering time and lower the sintering temperature. Microwave is electromagnetic wave with wavelength ranging between 1 m and 1 mm and frequency ranging from 1 to 300 GHz [24]. The difference between conventional furnace thermal sintering and microwave sintering is the mechanism of these two methods. Thermal approach sinters samples by transferring the heat through the objects via thermal conduction. The heating source of this technique is the furnace. However, microwave sintering is different. The material absorbs the electromagnetic energy and transforms it into heat to increase the temperature. Therefore, the heating source is material itself. Additionally, the internally generated heat is more selective and rapid to give rise to higher heating rates and remarkable reduction in the processing time (generally < 0.5 hour). Besides, because the heat is self-generated from the material, the heat consumption to the tool walls is avoided. For instance, Chang et al. used microwave method to successfully sinter sol-gel derived PZT at 500 W for 5 minutes soaking duration [25]. Although, the densification of the microwave sintered film is much higher than conventional thermal method with the same temperature and duration, some fundamental issues limit wide usage of microwave sintering PZT. The PZT can only absorb waves with a specific range of frequency, which limits the tool to high frequency (> 25 GHz). However, most commercialized microwave tool is at approximately 2.4 GHz, which lead to low microwave absorption of PZT. Therefore, either preheating is used or absorption aids are added to increase the efficiency of sintering. For example, Sharma et al. added Carbon powder in the PZT film to enhance the absorption [26]. Additionally, because the heat is generated internally, the volume of material is determining the heat generation. For a non-uniform film, the heat would generate non-uniformly and result in non-uniform property, even cracks in the film.

Laser sintering is an alternative low temperature fast thin film sintering approach. This technique uses focused high energy laser beam to scan the film in continuous or pulse mode to fuse and bond the powders into a layer of solid mass. For sintering PZT film, two kinds

of lasers are widely used: CO_2 and UV lasers. The advantages of laser sintering include the flexibility in manufacturing composites with different geometries with assistance of computer; controllable sintering thickness depending upon the laser energy and scanning speed; low influence to the substrate so create the possibility of processing PZT on low melting point substrate. However, laser sintering is not suitable for large size PZT samples due to the limitation of the laser spot size (generally ~ 50 μm in diameter).

The photonic sintering method is explored to eliminate the limitations of the existing sintering techniques in this work. The photonic sintering tool has a Xenon gas-filled flash lamp to generate broadband (ultraviolet to infrared), sub-millisecond high intensity pulses that controllably heat the particle films. The short pulse duration enables control of desired absorptive film heating and avoids undesirable conductive substrate heating. This approach permits PZT sintering while minimizing substrate heating, creating opportunities for direct sintering on low melting point materials.

The described deposition methods are summarized in the Table 3-1 with the strengths and weaknesses.

Table 3-2. Sintering methods with the strengths and weaknesses.

Sintering Method	Strengths	Weaknesses
Furnace	Easy to operate and access. Well established. Few parameters to control (time, ramping rate, and temperature).	Inert gas needed for avoiding oxidation. Substrate is heated up, thus low-temperature substrate cannot be used for high temperature process.
Microwave	High heating rate. Reduction in the processing time over the furnace sintering method.	Low energy absorption for PZT sintering. Non-uniform sintering quality for non-uniform film.
Laser	Controllable sintering thickness and path. Low	Low scanning speed and small laser spot size limit to

Sintering Method	Strengths	Weaknesses
	substrate temperature increase.	use it only for small features.
Photonic	Easy operation. Extremely short processing duration. Low substrate temperature increase.	Temperature gradient resulting in inconsistent sintering quality along depth direction.

3.2.3. PZT Film Poling

The properties of the piezoelectric materials are strongly dependent upon the direction. Significant differences of elastic and electric properties can be detected along different directions in fabricated PZT devices as mentioned in Chapter 2. However, in the unpoled PZT film, it shows low or even no overall piezoelectric property because of the distribution and orientation of the domains are arranged to minimize material free energy. Therefore, poling, which is used to reorient the domains towards the applied field direction, is significantly important to enhance the PZT piezoelectric property. Three factors are affecting poling quality, i.e. electric field, temperature, and time. The electric field is applied to generate space charge induced internal bias field in the PZT film to facilitate the alignment of the domains. With assistance of elevated temperature, the mobility of the domains is increased and, accordingly, it enhances the response of the domains to the electric field. Sufficient duration is also required for the poling process to stabilize and fix the reoriented domains after removing the field and temperature. However, the goal of poling process is using relatively shorter time, lower temperature and electric field to maximize the domains reorientation to obtain as high piezoelectric properties as possible. The most widely used method is directly applying high electric field (20 ~ 100 kV/cm) through the PZT film at elevated temperature, but lower than Curie point (T_C), for sufficiently long time (> 0.5 hr) to facilitate domains reorientation and stabilization. Since the breakdown field of the dry air is approximately 30 kV/cm, the sample would be poled in silicone oil while high poling electric field is utilized due to the high breakdown field of

the silicone oil. However, cleaning is very complex and time consuming after poling in the silicone oil. Therefore, several poling approaches have been developed to lower the field while obtaining similar or even superior piezoelectric property for PZT as conventional poling method.

One developed method is high temperature poling. This method requires the temperature increases to above PZT's T_C. Then desired DC poling electric field is applied and kept with reducing the temperature slowly to below T_C. This method is effective since the highest polarizability is just below T_C. Moreover, the electric field can be relatively low due to high temperature is utilized to highly increase the mobility of the domains. However, this high temperature limits further piezoelectric property improvement using a higher field since higher domain mobility results in lower breakdown field of the material. Additional to the better piezoelectric property, heat resisting property of the piezoelectric property of the PZT film is also demonstrated to be improved [27].

Photo-assisted poling has been demonstrated to improve the piezoelectric property of thin PZT films by Kholkin et al. [28]. Because the ultraviolet (UV) illumination of PZT films under electric field excites charge and the charge carriers may be trapped by defects near the film-electrode interfaces resulting in a bias electric field that compensated the depolarizing field. As a result, it improves the polarizing quality. However, since for the bulk PZT structure, high thickness results in opaque deep position at visible and UV wavelengths. Therefore, high poling quality would be difficult to be achieved at the deep layer. Consequently, this poling method can only positively affect thin films. Notice that, for exposure purpose, the top electrode of sandwiched PZT samples (i.e. electrode-PZT-electrode structure) requires transparent or semitransparent. So thin film or

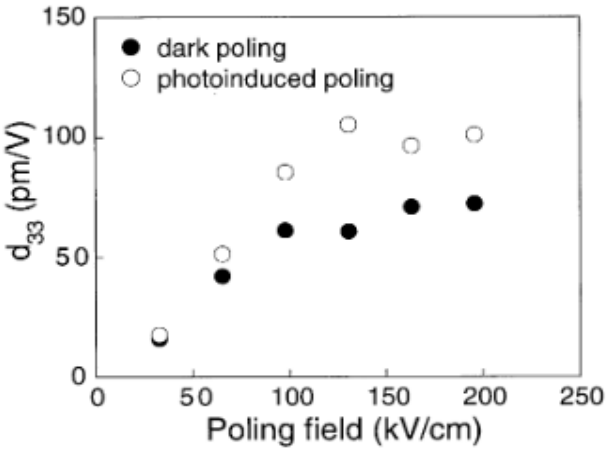

Figure 3-7. Piezoelectric coefficient (d_{33}) of a PZT film as a function of the applied poling field in dark and photoinduced poling conditions. The photoinduced poling results in enoumously higher d_{33} value when the filed level is higher than 50 kV/cm. Used with permission [28]

transparent electrically conductive material has to be used as the top electrode to allow for UV illumination of the film during poling. In order to obtain UV light, Kholkin et al. [28] used a 100 W Hg arc lamp, whose light was filtered through a 280 – 400 nm dichroic mirror to avoid excess heating of the films. After only 10 minutes poling at different electric field levels, the d_{33} was measured and plotted as a function of filed levels. A pronounced increase of d_{33} can be observed in photoinduced poling method compared with dark poling (without UV illumination) when poling field is higher than 50 kV/cm (Fig. 3-7).

Indium Tin Oxide (ITO) coated glass is widely used in many optical applications due to its electrical conduction and optical transparency. Ting et al. [29] employed this material as the electrodes for PZT film and claimed an enhanced piezoelectric properties of PZT was obtained. It is known that at a given temperature and duration level, the higher electric field applied to the PZT film, the higher piezoelectric field can obtained. However, many studies have been carried out and the observations reveal that cracks are produced and extended when high electric field is applied [30, 31]. These cracks lead to electric breakdown to negatively affect the poling process. However, Ting et al. [29] experimentally observed that the utilization of ITO glass electrodes can overcome the cracks occurred during high electric field (40 kV/cm) poling.

3.3. Photonic Sintering of Aerosol-Jet Printed PZT Film

With the development of the MEMS, the requirements of the low substrate temperature increase during PZT sintering is more and more urgent for some applications, for instance, flexible energy harvesters. Using conventional or aforementioned developed sintering methods could not meet the temperature requirement of the substrate. Therefore, this work reports a new PZT sintering method, namely photonic sintering. This approach facilitates the sintering of the PZT layer while lowering the temperature increase in the substrate. Additionally, aerosol-jet printing method, which is a direct writing technique, is employed for achieving PZT deposition. In this section, the detailed information of the new PZT deposition and sintering method is introduced. The piezoelectric property of photonic sintered PZT film is compared with thermally sintered sample to study the sintering quality of this new approach.

3.3.1. PZT Ink Preparation

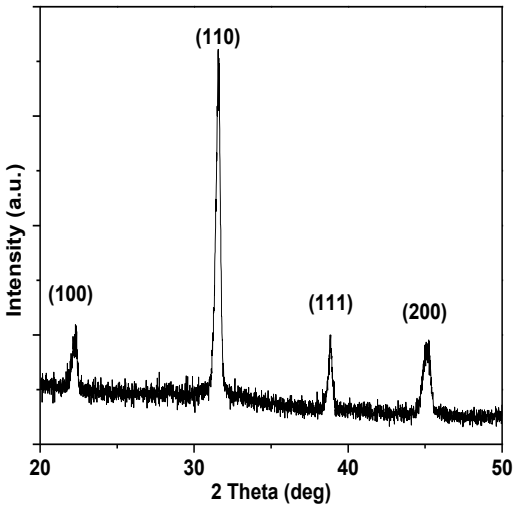

Figure 3-8. X-Ray Diffraction spectrum of the commercially available PZT powders shows peaks characteristic of a highly crystalline perovskite structure.

The PZT ink was prepared from commercially available PZT nanopowders (APC 855, APC International Ltd., USA) with a ratio 53:47 of Zirconium to Titanium. X-Ray Diffraction (XRD) on the starting PZT powder was performed on a Rigaku D/MAX-2B Powder X-Ray Diffractometer (Rigaku Co., Japan). In order to eliminate the influence of the substrate material, a silicon wafer substrate was used to provide a clean background spectra with an easily identifiable peak in the XRD analysis, while withstanding the high thermal sintering temperatures for sintered PZT film XRD analysis. The spectra indicate that the powders have the expected highly crystalline perovskite structure (Fig. 3-8). A PZT ink was formulated by mixing the PZT nanopowders with a DI water and ethylene glycol (EG) (Sigma-Aldrich Co. LLC., USA) solution. To obtain uniform and high-density films, a dispersant, DisperBYK-180 (BYK Chemie, Germany), was added to the ink solution. Polyvinylpyrrolidone (PVP) (Sigma-Aldrich Co. LLC., USA) was added to promote adhesion of printed PZT to the substrate following drying. The PZT ink composition was obtained by settling test and trial and error method. The ink composition by weight percentage is listed in Table 3-3.

Table 3-3. PZT ink composition

Material	Weight Percentage
PZT	30
DI Water	49.6
EG	12.4
DisperBYK-180	5
PVP	3

During manufacture of the PZT nano-particles, the PZT solution is spray dried with approximately 1% polyvinyl alcohol binder that agglomerates the nanoparticles together into aggregates ranging 10 ~ 150 μm. The prepared PZT ink solution was therefore stirred

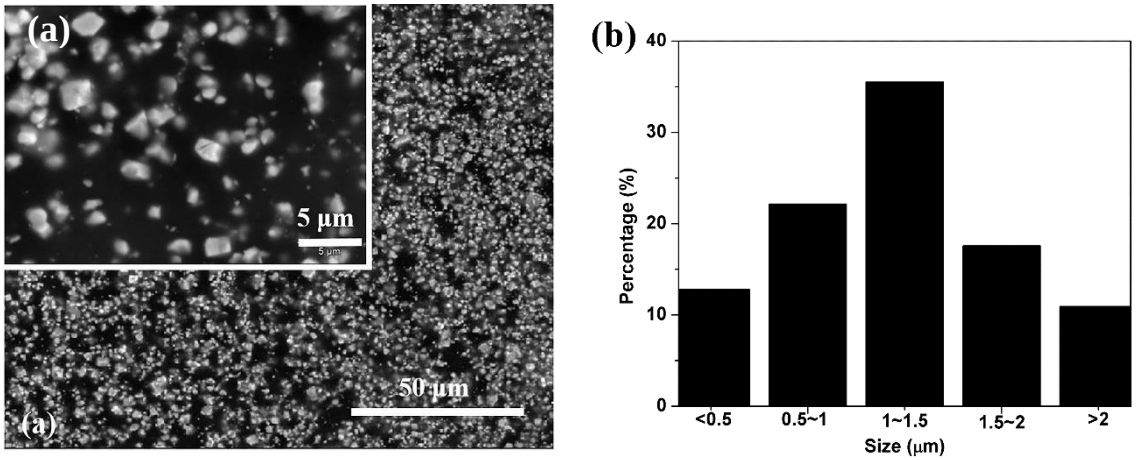

Figure 3-9. After stirring by a homogenizer, the PZT powders were de-agglomerated to separated particles (a). The inset of (a) is an example of one of five figures used to measure the powder size distribution. PZT particle size distribution was measured after de-agglomeration by a homogenizer (b). Over 70 % of the particles were smaller than 1.5 μm. The largest measured particle size was 3.54 μm.

by a homogenizer (PRO 250, PRO Scientific Inc., USA) for 5 minutes at 26000 rpm to de-agglomerate the PZT nano-particles (Fig. 3-9 (a)) and fully mix all components. The particle size distribution after de-agglomeration was examined by SEM image analysis using ImageJ. The inset of Fig. 3-9 (a) is an example of one of five equivalent magnification SEM images used for calculating the particle size distribution. The size distribution result is statistically recorded as shown in Fig. 3-9 (b). Over 70 % of the particles were smaller than 1.5 μm with the largest measured particle size 3.54 μm. The prepared ink was then transferred to a 120 ml atomization jar in the Aerosol Jet printer. The Aerosol Jet printer (Optomec, Inc., USA) is a maskless, CAD driven, non-contact printing system to deposit nanoparticle inks such as the PZT inks used in this research. The Aerosol Jet printer is able to precisely print inks having a wide viscosity range (1-1000 cP) onto almost any substrate including non-planar substrates. The printed film thickness can range from 100's of nanometers to 10's of millimeters depending upon the ink formulation and printing speed. The minimum achievable feature resolution is approximately 10 μm [16]. The Aerosol Jet printer atomizes the PZT ink into fine droplets that are carried to a ceramic nozzle with a 200 μm diameter orifice via a nitrogen carrier gas. The Aerosol Jet nozzle focusses the droplet stream to a ~20 - 100 μm wide printed line, depending on process parameters, via a co-axial nitrogen sheath gas. (The detailed process description of aerosol jet printing is presented in the Appendix A)

3.3.2. Film Sintering

Initial testing was done on stainless steel (SS) 430 substrates to facilitate direct comparison between the new photonic sintering and conventional thermal sintering. The 7 mm × 7 mm PZT film was printed on one side of the substrate. The printing speed was computer controlled and fixed at 10 mm/s for these experiments. The printing process was repeated twice on the same region to increase the printed film thickness. The printed film was dried in a vacuum oven at 200 °C for 2 hours to remove solvent. The dried PZT film was then either photonically or thermally sintered.

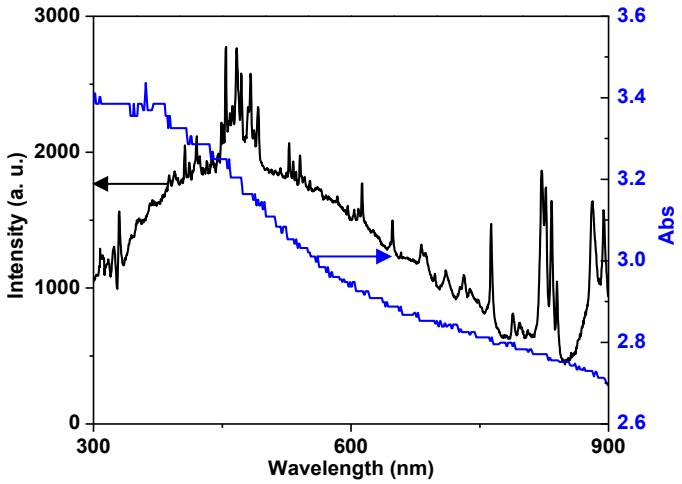

Figure 3-10. The light intensity spectrum of the Novacentrix bulb generated at 250 V level pulse setting (black), with a peak emission in the violet regime. The dried PZT film light absorbance spectral curve (blue) has significant overlap with bulb emission, with the greatest absorbance in the ultraviolet (< 400 nm), but significant absorbance at all wavelength levels due to the material thickness (> 30 μm). (Light intensity spectrum of the Novacentrix bulb courtesy from Novacentrix Corporation)

For photonic sintering, the light absorbance of the PZT film was characterized from 300 nm to 900 nm using a spectrophotometer (UV2100U, Shimadzu Corporation, Japan). The light transmittance and reflectance were measured directly using the spectrophotometer and then the light absorbance was obtained by subtracting these two components from the light source intensity. A plain glass slide substrate (Thermo Fisher Scientific, Inc., USA) with a measured absorbance below 0.0005 was used in this measurement to eliminate influence from the substrate. The measurement (Fig. 3-10) shows that the PZT is most absorptive to UV light (< 400 nm), but has significant absorbance at all wavelength levels. The light intensity of the flash lamp (75 mm long × 20 mm internal diameter quartz tube) in the photonic sintering system (Pulseforge 3300,

Novacentrix Corporation, USA) was controlled by four parameters: applied voltage (250 V), pulse duration (1300 μs), pulse frequency (2 Hz) and number of pulses (N=15). This parameter combination resulted in an energy density of 2.85 J/cm^2 on the PZT film for each pulse (total = 42.75 J/cm^2). The lamp produces a broad-spectrum output that is somewhat dependent on the applied voltage. For the 250 V pulse settings used in this research, the spectral intensity of the lamp as a function of wavelength is plotted in Fig. 3-9 with peak emission in the violet regime. Relatively high ultraviolet and violet light emission generated from the Novacentrix bulb accordingly facilitates the PZT film sintering. A thermocouple (MT-23/3, Physitemp Instruments, Inc., USA) was attached to the top surface of the substrate close to the PZT film (< 1 mm) to measure the substrate temperature *in-situ*. The thermocouple was shielded with white card stock paper to prevent direct heating from the light flashes. The peak substrate temperature measured using the thermocouple was 170.7 °C following the last pulse of the exposure pulse stream. For conventional thermal sintering, the samples were placed in a furnace (Lindberg/Blue M Box Furnace, Thermo Scientific, USA). In order to avoid oxidation of SS at high temperature, Argon gas was continuously flowed into the furnace during the sintering process. The temperature was ramped at 25 °C/min up to a soak temperature of 1000 °C where it was held for 1 hour. Then the furnace was turned off to cool down to room temperature before removal of the sample. The photonically and thermally sintered PZT films were imaged in a Scanning Electron Microscope (SEM) (JSM 6400, JEOL Ltd., Japan) to visualize the sintered surface and to obtain the Energy-Dispersive X-Ray Spectroscopy (EDS) spectra. Since sintering removes the organic components of the film, quantification of the Carbon (C) content of the sintered PZT film via EDS provides one objective measure of sintering quality. XRD was used to examine the sintered PZT films to study possible phase change during the sintering process as evaporation of PbO occurs at approximately 800 °C potentially resulting in weakened piezoelectric properties. The PZT film density was estimated (density = weight/volume) before and after sintering by simply measuring film width and length using an optical microscope (KH-7700, Hirox-USA, Inc., USA), height using a contact profilometer (P2, KLA Tencor, USA) and weight using a digital balance (Veritas M314Ai, Hogentogler & Co., Inc., USA).

3.3.3. Piezoelectric Testing Methods

Hysteresis loop (remnant polarization and coercive field), piezoelectric voltage coefficient, and permittivity were used to quantitatively compare sintered and unsintered groups to investigate the sintering quality and piezoelectric properties. The sintered PZT films were covered with Copper tape (3M Company, USA) as the top electrode for electrical characterization.

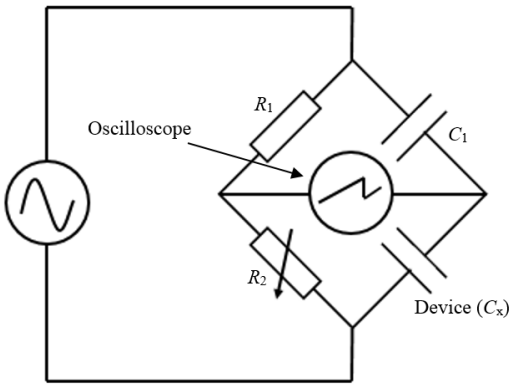

Figure 3-11. RC bridge circuit diagram for PZT film capacitance measurement. The bridge can be balanced by adjusting the resistance of R_2. The capacitance of the PZT device (C_X) is equal to the ratio $R_1 \times C_1$ to R_2

The ferroelectric properties were measured after six hours of PZT film preparation using a Sawyer-Tower circuit [32], with a 0.1 μF series capacitor. A signal generator (33120A, Agilent Technologies, USA) was used with an AC signal amplifier (610E, Trek, Inc., USA) to apply a 20 kV/cm sinusoidal wave signal having a frequency of 10 Hz to the circuit. The ferroelectric hysteresis loop was captured via an oscilloscope (TDS 2014B, Tektronix, Inc., USA). Prior to piezoelectric characterization, PZT films were poled under 150 °C for 2 hours with an electric field of 20 kV/cm. The poled PZT film was rested at room temperature overnight to relieve stress. Capacitance of the sintered film was measured using a RC bridge circuit as shown in Fig. 3-11 with applied 100 Hz, 10 V_{pp} sinusoidal wave signal. When the bridge was balanced, the capacitance of the device (C_x) can be obtained by Eq. 3-1.

$$C_x = \frac{C_1 R_1}{R_2} \tag{3-1}$$

Therefore, the relative permittivity (ε_r) can be calculated using Eq. 3-2

$$\varepsilon_r = \frac{C_x t}{\varepsilon_0 A} \tag{3-2}$$

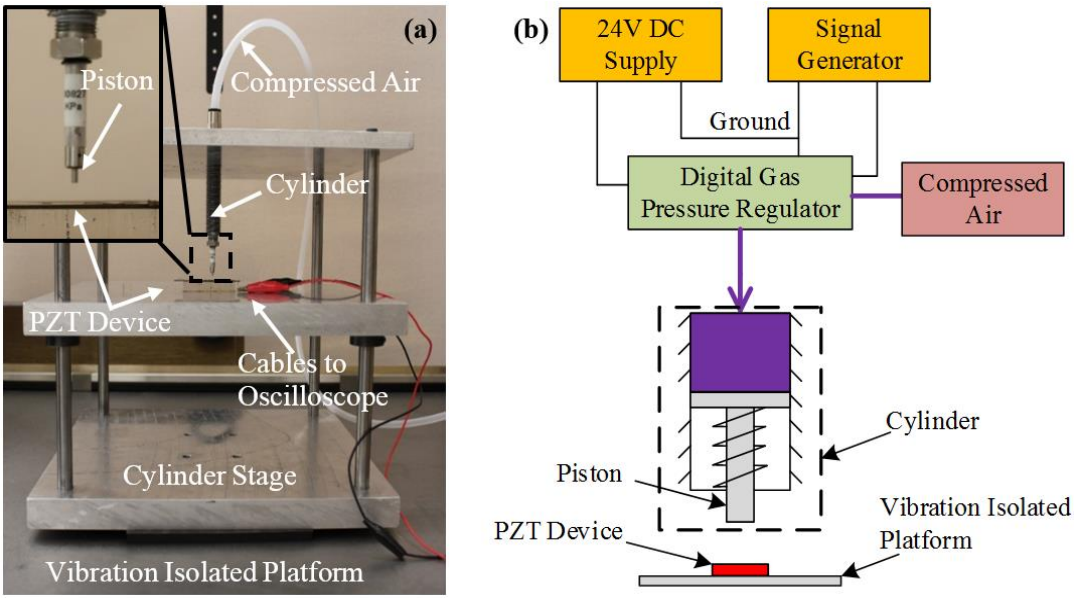

Figure 3-12. The picture (a) and schematic (b) of self-built cylinder system for piezoelectric voltage coefficient (g_{33}) measurement.

where t is the thickness of the sintered PZT film, A is the area of overlap of the top and bottom electrodes, and ε_0 is the permittivity of free space (8.854×10^{-12} F/m). The piezoelectric voltage constant, g_{33}, was measured using a custom-built cylinder system shown in Fig. 3-12 (a). The system was on a vibration isolated platform to eliminate the error due to environmental vibration. The set-up consisted of an electro-pneumatic pressure regulator (ITV2030-31N2BL4, SMC Co., USA) that was connected to a cylinder (SM-3-2, Clippard Instrument Laboratory, Inc., USA), located above the PZT device as shown in the Fig. 3-12 (b). The pressure regulator was supplied by a DC power supply of 24 V, while a signal generator provided the desired input signal to control the output compressed air pressure level and on/off frequency (Fig. 3-13 (a)). The output compressed air was applied to the cylinder to move the piston and accordingly provided the force to the device. A built-in spring was in the cylinder to push the piston back when the pressure regulator was in the off state. A linear relation between the applied signal magnitude (V_{pp}) on the signal generator and force generated from cylinder was obtained as shown in Fig. 3-13 (b). The stress (σ) applied to the device can be obtained by dividing this force by the contacted area of cylinder and sample (viz. 2 mm^2). This stress was then plotted against the open-circuit

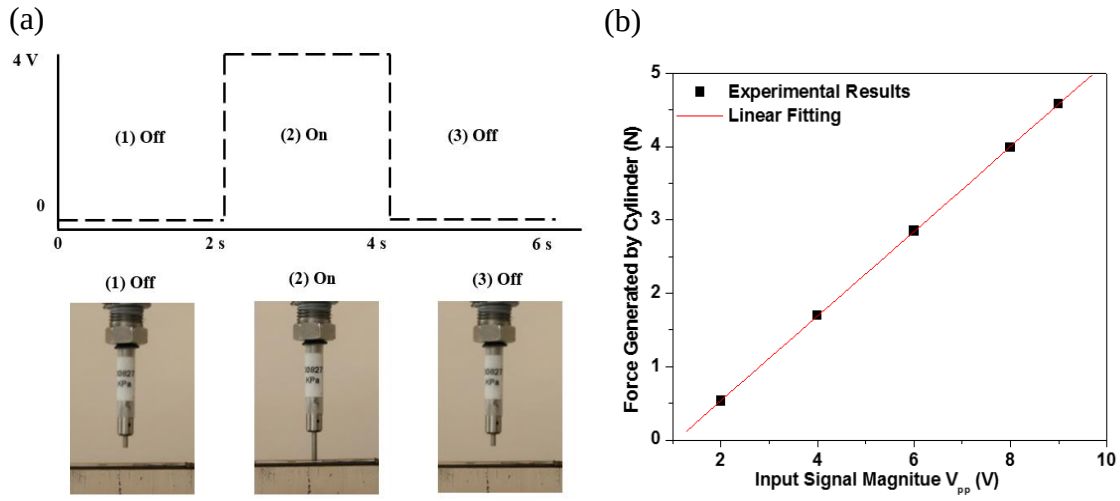

Figure 3-13. A signal generator provided a desired input signal to the gas pressure regulator to move the piston and accordingly to apply force to the PZT device. (a) The regulator was at off state when applied signal was zero, and no force was applied on the device ((1) and (3)). The regulator was at on state when the applied signal was at the desired drive voltage with a force was applied to the device (2). (b) The input signal magnitude has a linear relation with the force generated by the cylinder.

voltage measured using an oscilloscope. g_{33} was calculated using Eq. 3-3, where U represents the open-circuit voltage and t represents the PZT film thickness.

$$g_{33} = \frac{U}{t\sigma} \tag{3-3}$$

3.3.4. Heat Transfer Simulation

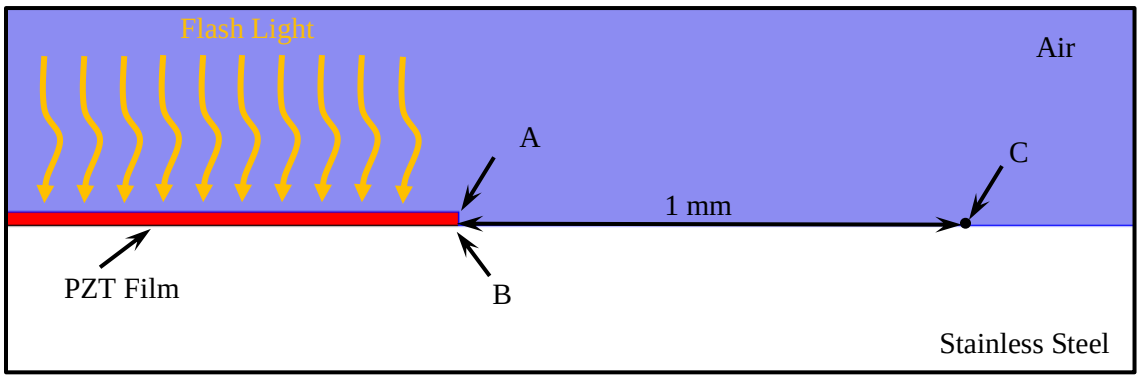

Figure 3-14. Device model (zoomed in) used in COMSOL heat transfer simulation. A, B and C are three study points for examining temperature change at the PZT layer, interface of PZT and SS, and position of thermocouple during photonic sintering, respectively.

Table 3-4. Material properties used in the finite element simulation

Material	Properties	Value	Unit
PZT	Thermal conductivity	1.6	W/(m-K)
	Heat capacity	320	J/(kg-K)
	Density	7500	kg/m^3
	Thickness	32.1	μm
Stainless Steel	Thermal conductivity	26	W/(m-K)
	Heat capacity	460	J/(kg-K)
	Density	7740	kg/m^3
	Thickness	550	μm
Air	Thermal conductivity	0.0257	W/(m-K)
	Heat capacity	1005	J/(kg-K)
	Density	1.205	kg/m^3

To examine the accuracy of the substrate thermocouple temperature measurement and to study the temperature change in the PZT layer and interface between PZT and substrate, heat transfer simulations were performed in COMSOL 4.3a. A 2-dimensional model was built as shown in Fig. 3-14 with equivalent dimensions as the experimental device. Material parameters used in the simulations are listed in Table 3-4. Three points (A, B, and C) were defined to evaluate temperature change. Point A was the top surface of the PZT layer, which directly absorbed the energy from flashes during sintering. Point B was the interface between PZT and substrate. Point C was on the substrate, and 1 mm from point B, where the experimental thermocouple probe was placed. In order to mimic the time dependent flashes, time dependent input energy was applied to the top surface of the PZT only. The input energy was the same as the experimentally used energy (i.e. 2.85 J/cm^2 for each flash). The initial temperature on the model was set as room temperature (20 °C). During sintering, heat was transferred from the PZT surface down to the substrate via conduction. The dominant equation used in the simulation was Eq. 3-4.

$$q_{cond} = \rho C_p \frac{\partial T}{\partial t} - \nabla(k \nabla T) \tag{3-4}$$

$$q_{conv} = h(T_{amb} - T) \tag{3-5}$$

$$q_{rad} = \varepsilon\sigma_{SB}(T_{\text{amb}}^4 - T^4) \tag{3-6}$$

where q_{cond} represents the power transferred by thermal conduction effects; ρ, C_p and k are the density, heat capacity, and thermal conductivity of the material, respectively; t is time, and T is the temperature. The values used for each of the material parameters are listed in the Table 3-2. However, since the experiment was performed in the atmospheric condition, heat dissipation by thermal convection from the device to the air was also considered in the simulation. The thermal convection governing equation used in the simulation is shown in Eq. 3-5, where q_{conv} represents the power transferred by thermal convection effects; h is the heat transfer coefficient of the air, which was set as 100 W/(m^2-K); and T_{amb} is room temperature (20 °C). Thermal radiation was studied in the simulation using the governing Eq. 3-6, where q_{rad} is the power transferred by thermal radiation effects, ε is the emissivity of the heated material (PZT and stainless steel), σ_{SB} is the Stefan – Boltzmann constant. Since it was difficult to find reported emissivity for PZT films, a range of values from 1 to 0.01 was used in the simulation with differences in resulting film temperature less than 0.8 % observed. Similarly, the influence of heat radiation (with PZT emissivity set to 1) resulted in a temperature change of less than 0.5% as compared to a simulation where $q_{\text{rad}} = 0$. Therefore, the influence of radiation was neglected in the simulation. After 15 flashes, the temperature change resulting at the three study points was plotted in Fig. 3-15. The highest temperature at the top PZT surface reached 917.4 °C, while the interface between PZT and SS only increased to 192.7 °C. The position

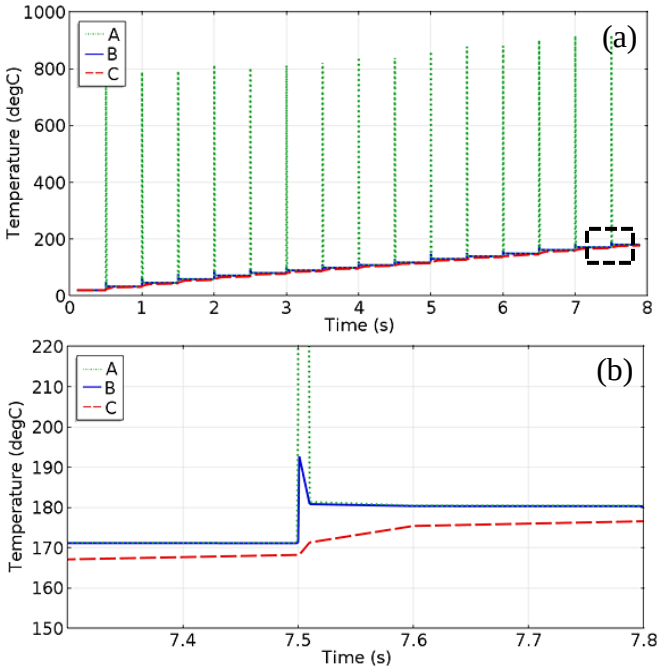

Figure 3-15. (a) Simulated temperature change at A, B, and C points for all 15 flashes. (b) The details of the dashed frame of (a), which is the temperature change at B and C for the last pulse of the exposure pulse stream. The highest temperature at the PZT surface was 917.4 °C (A), while the interface between PZT and SS only increased to 192.7 °C (B). The maximal substrate temperature at the thermocouple measurement point (C) was 177.7 °C.

where the thermocouple was placed increased to 177.7 °C. The simulation result of point C agreed well with the thermocouple measured result (170.7 °C). And the results suggests the simulated interface temperature was approximately 15 °C higher than that measured in the experiments.

3.3.5. Experimental Results and Discussions

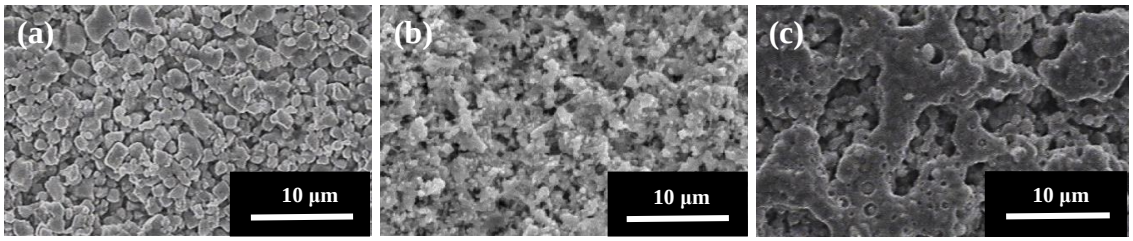

Figure 3-16. SEM images of PZT films prior to sintering (a), after thermal sintering (b), and after photonic sintering (c). The dried films are uniform with high density of PZT particles. The photonically sintered film has larger regions of fused and merged particles than thermally sintered film.

Figure 3-16 (a) shows an SEM image of the dried PZT film prior to sintering, showing uniformly distributed particles. Figures 3-16 (b) and (c) show the SEM images of thermally and photonically sintered PZT films, respectively. While sintering necks between PZT particles are noticeable in both Fig. 3-16 (b) and (c), the photonically sintered film has larger regions of fused and merged particles at the film surface. These are likely caused by actual melting of PZT powders during the sequence of short, but intense, energy pulses. Both approaches densified the PZT film from 74.2 % (dried film) of the theoretical APC 855 density to 84.6 % (thermal sintering) and 80.7 %

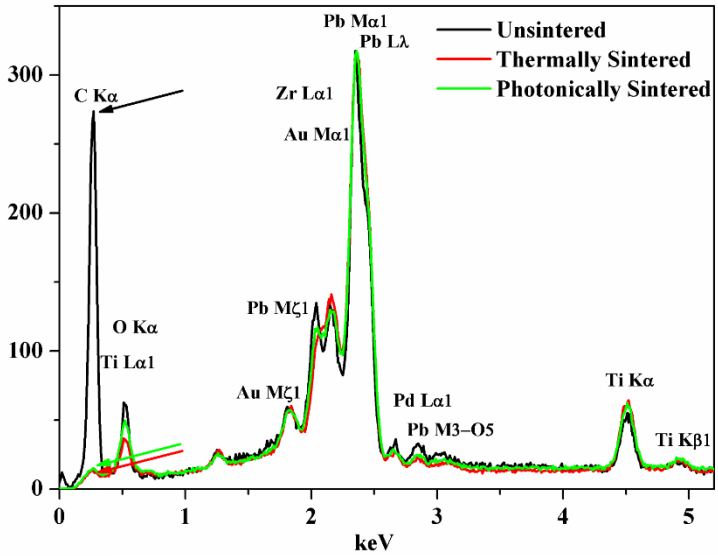

Figure 3-17. EDS (Energy-dispersive X-ray spectroscopy) results of unsintered and sintered PZT films. The PZT film prior to sintering (black) has a high C peak of 265. Photonic sintering (green) reduces the C peak to 14, which is comparable to that obtained with conventional thermal sintering (red), 12. Low C content indicates the organic products have been removed from the PZT film during sintering

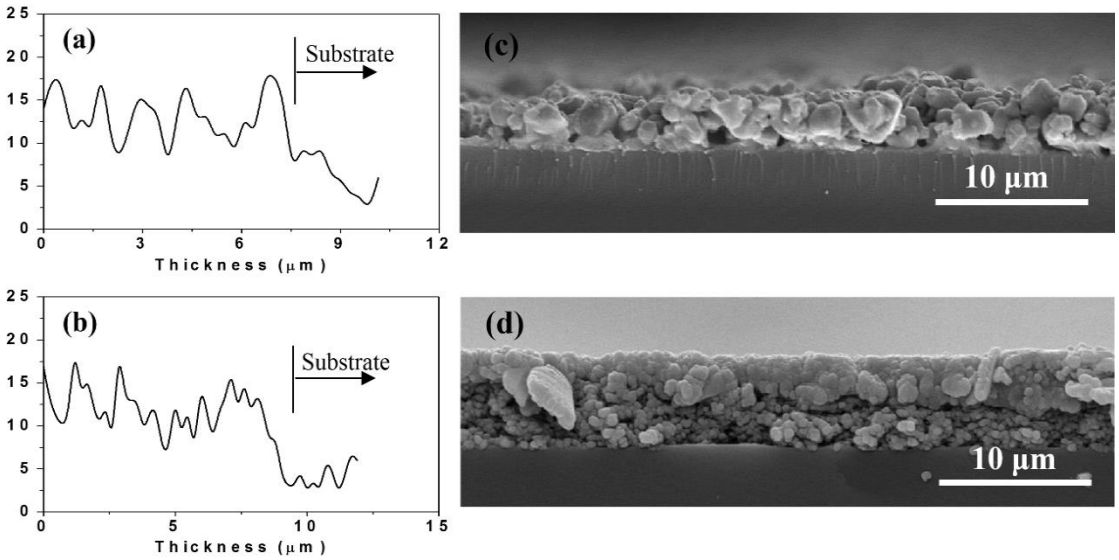

Figure 3-18. EDS of Carbon content of thermally sintered (a), and photonically sintered (b) films through the film thickness. The Carbon content were consistently low (averaged value of 12.5 for thermally sintered and 12.8 for photonically sintered) throughout the entire film thickness, demonstrating the organic products had been significantly removed from film. The films prior to sintering exhibit Carbon levels in excess of 265. Cross-sectional micrographs of thermally sintered (c) films show larger grain sizes than those of the photonically sintered (d) films, with the difference most prominent closest to the substrate.

(photonic sintering), respectively. Film thicknesses were measured before and after sintering using the contact profilometer. However, the films were directly printed resulting in a rough surface with some thickness non-uniformities. Therefore, an average thickness has been reported. The unsintered PZT film thickness of 32.1 μm was reduced during sintering to 6.1 μm (thermal) and 9.8 μm (photonic) due to removal of organic components and sintering densification of PZT particles. The EDS analysis of Fig. 3-17 reveals a high C peak of 265 for the unsintered films that is reduced to 14 for photonic sintering and 12 for thermal sintering. An almost equal C peak in the photonically sintered film suggests complete organic product removal in the sintering process as compared to the thermally sintered counterpart. Carbon content along film depth captured by EDS and cross-sectional micrographs of thermally, and photonically sintered films were used to study the sintering quality along the film thickness (Fig. 3-18). The carbon content was consistently low (averaged value of 12.5 (Fig. 3-18 (a)) for thermally sintered and 12.8 (Fig. 3-18 (b)) for photonically sintered) throughout the entire film thickness, demonstrating the organic products had been significantly removed from films. However, larger grain size was observed in the cross-sectional micrograph of thermally sintered film (Fig. 3-18 (c)) at the

substrate interface than those of the photonically sintered film (Fig. 3-18 (d)). This indicates the depth of photonic sintering did not extend through the full thickness of the printed film due the temperature gradient from surface to the substrate interface as shown by the simulation result of Fig. 3-15. The lower temperature results in less effective fusing and merging of the particles at the interface, resulting in a more porous layer deep within the film and contributing to an overall thicker film for the photonic sintering method. XRD results of sintered films are showing in Fig. 3-19. Because of the PbO evaporation, a second phase, known as pyrochlore phase (or Pb-deficient phase), was observed in both sintered films with much weaker phase intensity in photonically sintered film. This pyrochlore phase negatively affects the piezoelectric properties. Therefore, the photonically sintered film was expected to have better piezoelectric properties. However, the addition of low concentrations of PbO (1 wt.%) was demonstrated to reduce (thermally sintered) or eliminate (photonically sintered) this secondary phase (shown in Appendix B). This lower secondary phase exhibited in the photonically sintered PZT films is most likely due to the rapid sintering process: The duration is not sufficient to allow Pb complete the reaction with Oxygen resulting in less Pb deficiency. Therefore, photonic sintering can reduce or even eliminate the secondary phase to enhance the piezoelectric properties.

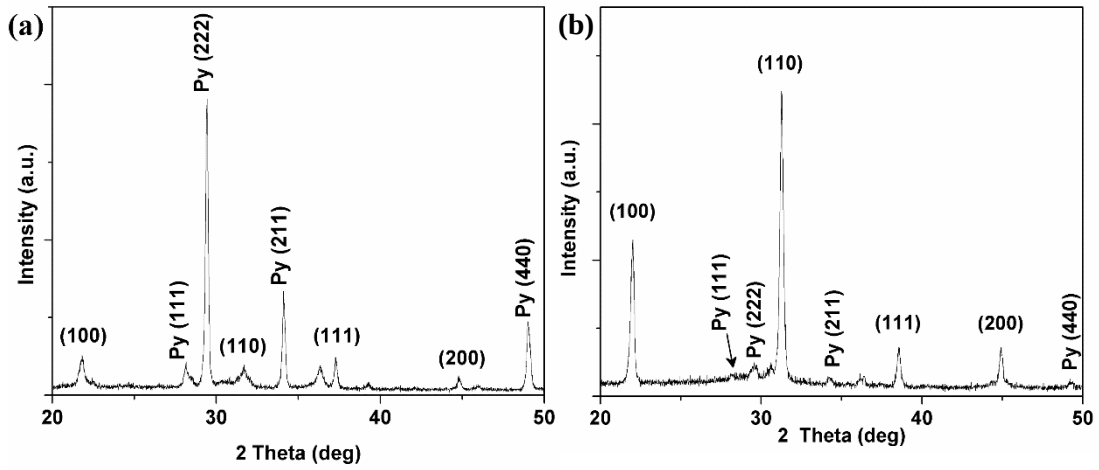

Figure 3-19. XRD results for thermally (a) and photonically (b) sintered PZT films. A pyrochlore phase (marked as "Py") was observed in both PZT films due to Pb lost during high temperature sintering. However, in photonically sintered film, this phase was much weaker

The measured ferroelectric and piezoelectric properties of PZT films sintered by the two approaches are summarized in Table 3-5 and compared with an unsintered group. Notice the g_{33} and ε_r were from the average of three samples. One standard deviation is also included in the table. The capacitance was measured using RC bridge circuit. And the relative permittivity was calculated using Eq. 3-2. The relative permittivity of thermally and photonically sintered PZT film were 1273.5 and 1615.1, respectively. Notice that higher relative permittivity was obtained in photonically sintered film. It indicates better energy storage capability is in photonically sintered PZT film. The ferroelectric property was tested using a self-built Sawyer-Tower circuit. Since the PZT powder has a perovskite structure, a weak ferroelectric hysteresis loop is expected in the unsintered film. After organic materials are removed during sintering, the PZT particles fuse together forming a denser film. Therefore, the sintered films are expected to show improved ferroelectric properties. The polarization-electric field loops for unsintered, thermally sintered, and photonically sintered films are plotted in Fig. 3-20. The remanent polarization (P_r) and the coercive field (E_c) for the photonically sintered films are 32.4 μC/cm^2 and 6.7 kV/cm, respectively. These exceed measured P_r and E_c values for the thermally sintered films of 17.1 μC/cm^2 and 6.3 kV/cm, respectively. This demonstrates superior performance with photonic sintering. The ferroelectric properties of both films are improved over the unsintered film (P_r = 0.03 μC/cm^2 and E_c = 1.7 kV/cm) as expected. The photonically sintered films show better remanent polarization to those reported by other groups measured with approximately 20 kV/cm electric field (e.g. ~10 μC/cm^2 by Zhang et al [33] using thermal sintering (estimated from Fig. 8 (a) of reference 33) and ~ 8 μC/cm^2

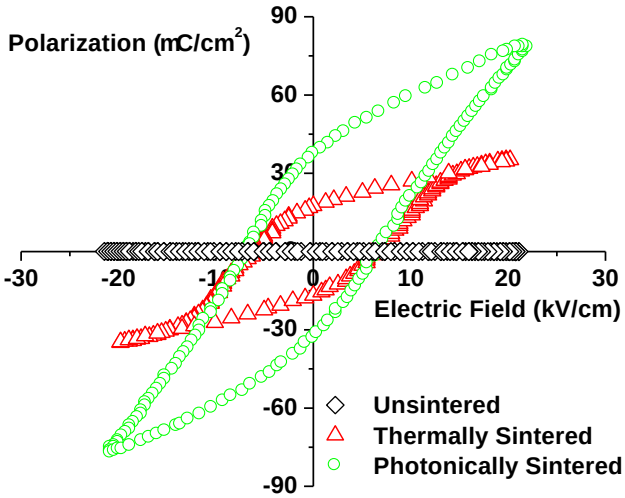

Figure 3-20. Low frequency hysteresis loop shows photonically sintered (green) PZT film has superior remanent polarization (32.4 μC/cm2) than the thermally sintered (red) film (17.1 μC/cm2). In both cases, the ferroelectric properties are improved over the unsintered (black) film (0.03 μC/cm2). Applied electric field in the ferroelectric measurement is 20 kV/cm, and frequency is 10 Hz.

by Baba et al [34] (estimated from Fig. 8 (a) of reference 34 using the innermost hysteresis curve)). The high remanent polarization and low coercive field allow operation at low voltages, with short switching times and good retention [25, 35]. These advantages are desirable for most piezoelectric device applications.

Table 3-5. The electrical properties of PZT films sintered using different methods

PZT Film	P_r	E_c	g_{33} (10^{-3} V-m/N)	ε_r
Unsintered	0.03	1.7		
Thermally Sintered	17.1	6.3	16.9±1.0	1273±159
Photonically Sintered	32.4	6.7	17.9±0.8	1615±212

The piezoelectric voltage constant (g_{33}) was measured using a custom-built cylinder system. The measured g_{33} values were -16.9×10^{-3} V-m/N and -17.9×10^{-3} V-m/N for the thermally sintered and photonically sintered films, respectively. Although these results are lower than the reported APC 855 PZT powder g_{33} value of -21×10^{-3} V-m/N, they can be dramatically improved by further optimizing the sintering performance to consistently sinter throughout the entire film thickness, and increasing the poling electric field strength, temperature and time [36, 37]. It is also important to note that the photonically sintered film has a higher g_{33} value than the thermally sintered film, suggesting the photonically sintered films may perform better as piezoelectric transducers. This improvement may be attributed to the greater degree of particle consolidation at the surface of the photonically sintered film. Many earlier experimental investigations have been reported for the relation between particle size and piezoelectric properties. [38, 39] The larger particle size, the higher piezoelectric properties. The reason is believed to relate to the contribution of the domain walls [40]. The piezoelectric properties are highly positively dependent upon the domain wall motion during the poling process [41]. Furthermore, the domain wall mobility increases with particle size [41]. Therefore, larger particle size will lead to higher domain wall mobility, and consequently would result in better piezoelectric properties. Another important contribution to the superior piezoelectric properties in photonically sintered PZT film is pyrochlore phase. Greater pyrochlore phase formation was observed in thermally sintered film leading to weaker piezoelectric properties. The piezoelectric coefficient results were surprisingly high since the relative permittivity of the films were low.

However, similar results have been reported by many self-synthesized and commercially available PZT (or PZT compositions) sintering methods [20, 42]. Additionally, two error sources may contribute to these high measured results. It is possible internal stress induced by drying and sintering of the samples may have induced domain alignment that could enhance the piezoelectric effect [43]. The resolution of the oscilloscope used for the open-circuit voltage measurements (4 mV) may have also introduced measurement error of a few percent. These factors may have impacted both measured g_{33} values. While additional optimization of g_{33} testing might refine the accuracy of the value, the current results demonstrate the PZT was successfully photonically sintered.

3.4. Further Enhancement of Piezoelectric Properties via Quality Sintering throughout the Entire Film Thickness

With the current film thickness and sintering parameters, the high quality sintering can only extend top ~5 μm film layer due to the temperature gradient as shown in the simulation result of Fig. 3-14. The porous bottom layer affected the poling quality and accordingly limited the piezoelectric property. Reducing the film thickness was necessary to achieve a high sintering quality throughout the film depth. However, due to the micro-scaled particle size limitation, it was difficult to obtain a further thinner film. Therefore, nanometer-scaled particles were used to replace the micrometer-scaled particles for achieving thinner film. Moreover, larger specific surface area of nano powders contributes to lowering the required sintering temperature to further improve the sintering quality throughout the film thickness. The effect of sinter aid on lowering the sintering temperature was also studied in this work to further reduce the sintering temperature. Design of experiment (DOE) was carried out for sintering parameter optimization to ultimately obtain a quality sintering throughout the entire film thickness.

3.4.1 PZT Sintering Temperature Reduction

Two main approaches are widely used to lower the PZT sintering temperature: reducing the powder size and adding the sintering aid.

In 1981, the importance of smaller particle size on lowering sintering temperature was highlighted by Rhodes [44]. After that, many groups have demonstrated that the reduction of particle size results in lower sintering temperature [45-47]. This attributes to that the

smaller particles have larger specific surface area, which results in higher surface energy due to the Eq. 3-7.

$$\Delta G = V\mathrm{d}P - S\mathrm{d}T + \gamma \mathrm{d}A \tag{3-7}$$

where G is the Gibbs free energy of a system, V is the volume, P is the pressure, S is the entropy, T is the temperature, γ is the surface energy, and A is the specific surface area. Therefore, provided the pressure and the temperature are the same, the surface energy is inversely proportional to the specific surface area for obtaining the same free energy. It is believed that the surface energy is the main driving force in the sintering process [48]. Moreover, due to smaller particle size, the size of pores and gaps between particles is also smaller. This shortens the required distance between two particles to form a neck during sintering. Therefore, smaller particles tend to be well sintered at lower temperature.

Recently, the nano-scaled powders (LQ-S2-P, Choko Co., Ltd., Japan) with approximately 480 nm average and 1.6 μm largest particle sizes were used for the purpose of obtaining the thinner film and lowering the required sintering temperature. The size distribution plot is shown in the Fig. 3-21.

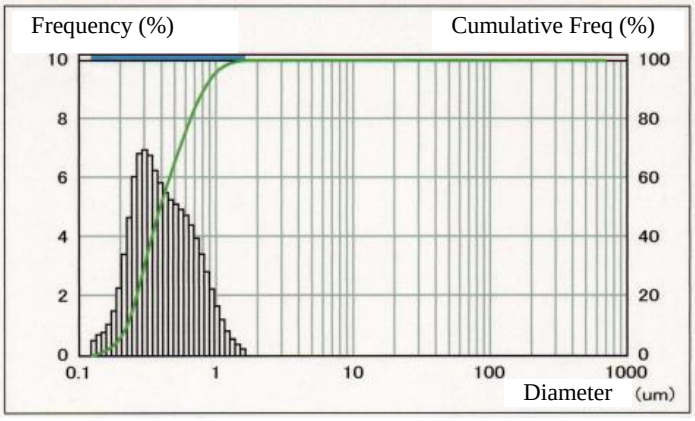

Figure 3-21. The particle size distribution of nano-scaled PZT powders. The average particle size is approximately 480 nm and the largest particle is 1.6 μm. (plot courtesy from Choko Co.)

The sintering temperature of nano-scaled particles was measured in comparison with micro-scaled powders. The particles were uniaxially dry pressed to form pellets. Then the pellets were sintered in the furnace under different temperatures for 1 hour. In order to avoid oxidation of the pellets at high temperature, Nitrogen gas was continuously flowed into the furnace during the firing process and was not removed until the furnace cooled down to the room temperature. Density of the pellets was used to quantitatively estimate the sintering quality. The fired pellets weight was measured using a digital balance (Veritas M314Ai, Hogentogler & Co., Inc., USA), and the volume was measured using Archimedes' method. The pellets' density was calculated using dividing weight by volume. The result of nano-scaled and micro-

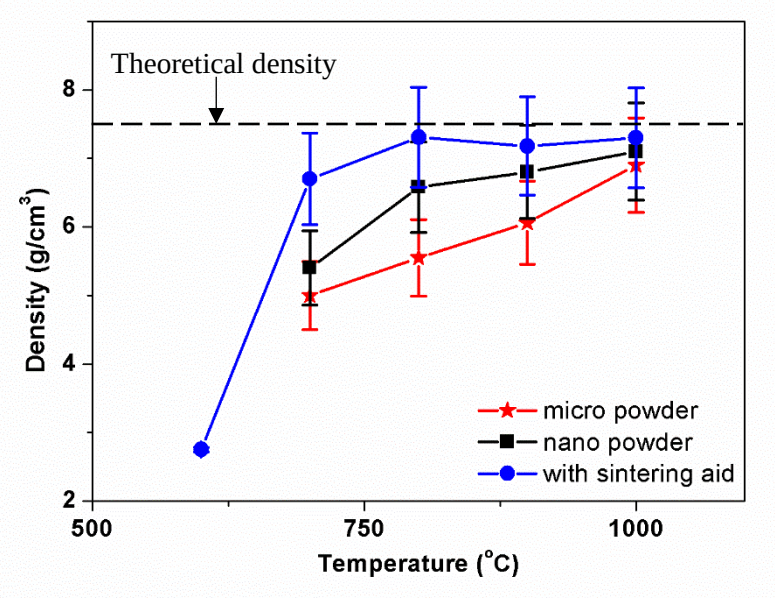

Figure 3-22. The measured density change with temperature for micro-scaled PZT particles, nano-scaled PZT particles, and nano-scaled PZT particles with sintering aid. Reduction of particle size can lower the sintering temperature from > 1000 °C to approximately 1000 °C. Mixing sintering aid with nano-scaled particles could further reduce the sintering temperature to ~ 800 °C.

scaled powder density change with temperature is shown in the Fig. 3-22. The pellets forming by the nano-scaled powders had higher density than the micro-scaled powders for all temperature levels and almost reached the reported theoretical density (7.5 g/cm^3) indicating better sintering quality can be achieved using nano-scaled powders. And the sintering temperature of the nano-scaled powders is approximately 1000 °C, while the micro-scaled powders have higher temperature (> 1000 °C). Notice each date-point is averaged from 3 samples and the error bar represents 1 standard deviation.

Adding sintering aid is another approach to lower the sintering temperature, which has been introduced in Chapter 3.3.1. Liquid phase sintering aid, basically the form of metal oxides additives into green unsintered ceramics to aid film densification, was first reported to lower the ceramic material sintering temperature over 50 years ago by W. D. Kingery [49]. These aids with certain weight percentage are incorporated into the ceramic film and fired. At an early stage of firing, typically, the temperature is significantly lower than the ceramic required sintering temperature, the aids change into a liquid phase by either forming a eutectic phase or self-melting. The liquid between particles accelerates particles' merge by playing two roles: Firstly, the liquid phase sintering aids serve as the lubricant to assist particles' reorientation into a more favorable packing arrangement as the particles

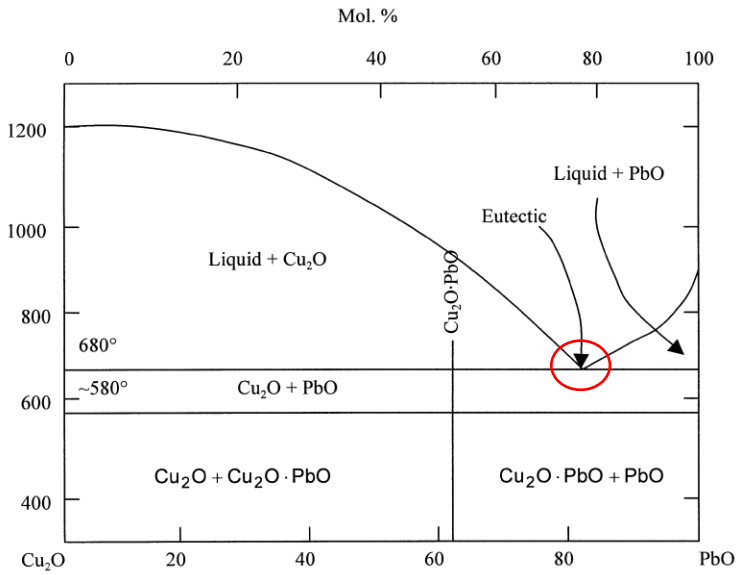

Figure 3-23. The phase equilibrium diagram of the Cu_2O-PbO system. The eutectic phase is formed as the temperature increased up to 680 °C. Used with permission [20]

expanding during firing. Secondly, the liquid phase sintering aids pull particles closer due to the generated capillary force. Therefore, the energy required to form the neck between two particles are lowered and accordingly reduces the sintering temperature. Corker et al. [20], for the first time, proposed the use of Cu_2O-PbO eutectic phase liquid sintering aid to lower the PZT film sintering temperature. The combination of Cu_2O and PbO in a molar percentage ratio of 1:4 forms a eutectic phase with the temperature of approximately 680 °C as shown in the Fig. 3-23. Corker et al. claimed the PZT film sintering temperature was reduced to 800 °C when adding 5% weight percentage of the sintering aid. Moreover, due to the low sintering temperature, the Lead loss issue is also eliminated. Therefore, the ink composition was updated using settling test and trial and error method and shown in the Table 3-6.

Table 3-6. Low sintering temperature nano-sized PZT powder based ink composition

Material	wt%
PZT	30
DI Water	65.4
PVP	3
Cu_2O	0.22
PbO	1.38

In order to study the sintering temperature of the updated ink, the ink was firstly dried on the hotplate at 200 °C for 1 hour to remove the DI water. Then a lump of the dried ink was pressed into a pellet, fired in the furnace, and measured the density using aforementioned method. The density change with the firing temperature is shown in the

Fig. 3-22. The samples with sintering aid had the highest density at all temperature levels and reached the theoretical value when fired under 800 °C. There was only slight fluctuation of measured density while fired using even higher temperature (> 800 °C). These indicate that the sintering temperature of the ink with sintering aid has been further reduced to ~ 800 °C.

3.4.2 Photonic Sintering Optimization

The usage of the nano-scaled powders creates the opportunity to reduce the film thickness. By fine adjusting the printing parameters, the resulting film thickness was 6 μm. The morphology of printed PZT film was inspected using a SEM. Prior to sintering, the nano-sized particles were uniformly distributed to form a high density PZT film. This film shows smaller pore size and more compacted particle pack than micro-sized particle based film shown in Fig. 3-24. A Design of Experiment (DOE) with 5 variables (voltage, pulse duration, frequency, number of pulses, and number of cycles), 2 levels, and 2 replicates was carried out to realize the optimal photonic sintering parameters (Appendix C). 7 mm × 7 mm square PZT films were printed on the stainless steel substrate for DOE study. SEM images were used to

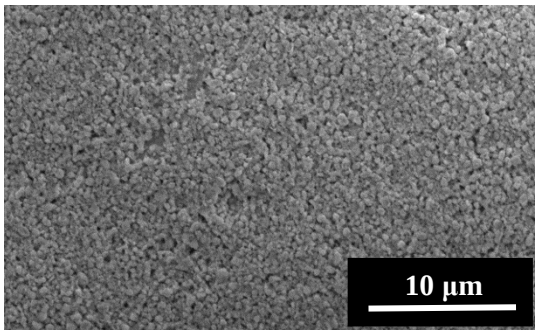

Figure 3-24. Prior to sintering, the nano-sized particles were uniformly distributed to form a high density PZT film. This film shows smaller pore size and more compacted particle pack than micro-sized particle based film.

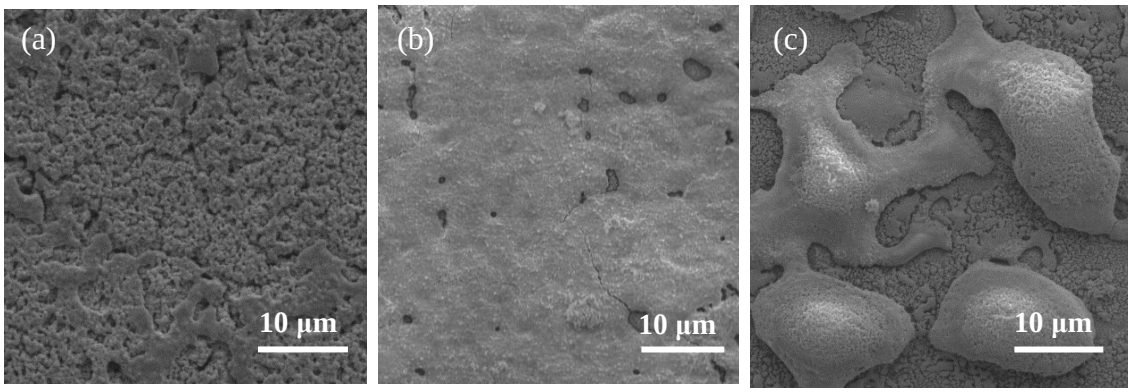

Figure 3-25. The SEM images of under-exposed (a), well-exposed (b), and over-exposed (c) films for DOE qualitative investigation. The sintering quality number of 0.2, 0.5, and 0.8, respectively, were given.

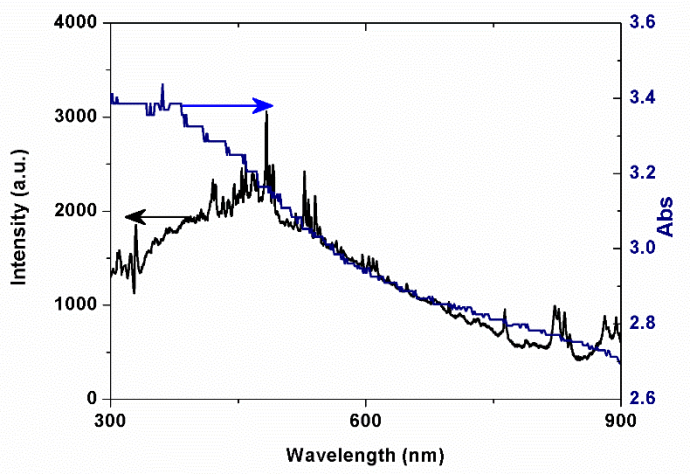

Figure 3-26. The light intensity spectrum of the Novacentrix bulb generated at 400 V level pulse setting (black), with a peak emission in the violet regime. The dried PZT film light absorbance spectral curve (blue) has significant overlap with bulb emission, with the greatest absorbance in the ultraviolet (< 400 nm). (Light intensity spectrum of the Novacentrix bulb courtesy from Novacentrix Corporation)

qualitatively evaluate the sintering results. A quality number ranging from 0 to 1 was given to represent the sintering quality served as the response for the DOE. 0 represented non-sintered films. 1 represented burned films. 0.5 represented well-sintered films. Three SEM image examples are shown in the Fig. 3-25 indicating an under-exposed film (Fig. 3-25 (a)), a well-exposed film (Fig. 3-25 (b)), and an over-exposed film (Fig. 3-25 (c)). The optimized sintering parameter combination is: voltage = 400 V; pulse duration = 650 μs; frequency = 2 Hz; number of pulses =20; number of cycles = 2. This combination gave an energy density of 5.06 J/cm^2 delivered to the target film for each pulsed flash and total 202.40 J/cm^2. For the 400 V pulse settings, the spectral intensity of the lamp as a function of wavelength is plotted in Fig. 3-26 with peak emission in the violet regime. The dried PZT film light absorbance spectral curve is also plotted and shows high absorbance over all wavelength with the greatest absorbance in the ultraviolet (< 400 nm), which has significant overlap with the bulb emission spectrum This great overlap accordingly facilitates the PZT film sintering. A COMSOL simulation was carried out to further study the temperature change in the film and substrate. The module, material parameters, and settings used in the COMSOL for this modeling were the same as mentioned in the Chapter 3.3. The geometries and size of the substrate and the PZT film built in the COMSOL were equivalent as the experiments. The input energy was updated to 5.06 J/cm^2 for each pulse.

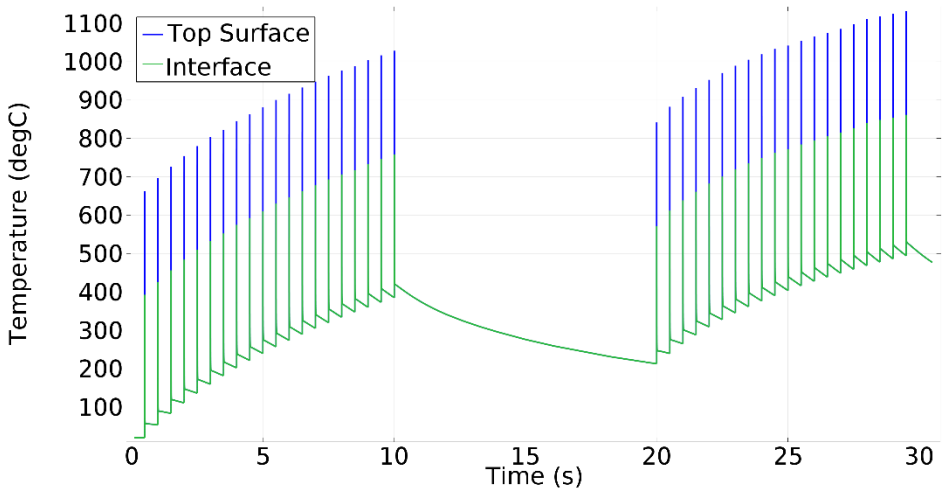

Figure 3-27. Simulated temperature change at the top surface of the PZT film and the film-substrate interface for 2 cycles of flashes. The temperature, after 2 cycles, is sufficiently high to sinter throughout the whole thickness.

In the experiment, there was a 10 seconds time gap between two cycles to avoid the PulseForge sintering chamber overheated to stop working. After the entire 2 cycles of exposure, the temperature change resulting at the film top surface and the film-substrate interface was plotted in Fig. 3-27. The highest temperature at the top PZT surface reached > 1100 °C, and the interface between PZT and substrate also increased to ~ 900 °C. Both temperatures are sufficiently high to sinter the film, which suggests the film should have been successfully sintered throughout the whole thickness at such sintering parameters combination. The cross-sectional view of the well-sintered PZT film was imaged in the SEM (Fig. 3-28). It is observed that the entire film was merged and densified as one single piece indicating a good sintering quality throughout the entire film thickness, which also verificated the simulation. A thermally sintered PZT film was also prepared for comparison using 1000 °C for 1 hour in the N_2 environment.

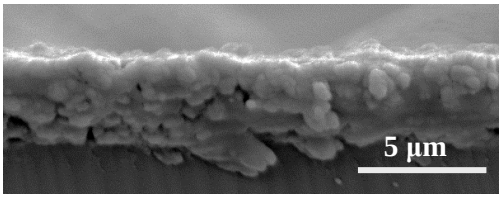

Figure 3-28. Cross-sectional view of the well-sintered PZT film. The whole film was merged and densified as a one piece indicating a good sintering quality throughout the entire thickness.

3.4.3 Piezoelectric Characterization

The P-E hysteresis loop, permittivity, and piezoelectric voltage coefficient (g_{33}) of the sintered films were measured using self-built Sawyer-Tower circuit, RC bridge circuit, and

cylinder system, respectively. The measured piezoelectric properties of PZT films using updated process are summarized in Table 3-7 in comparison with the aforementioned micro-scaled powder based film and thermally sintered groups. Notice, g_{33} and ε_r were obtained from the average of three samples. One standard deviation is also included in the table. The P-E hysteresis loops for the photonically and thermally sintered nano-scaled PZT powder films are plotted in Fig. 3-29. The remanent polarization (P_r) and the coercive field (E_c) are 43.9 μC/cm^2 and 9.8 kV/cm, respectively, for the photonically sintered film, which exceed the thermally sintered film (17.7 μC/cm^2 and 10.8 kV/cm, respectively). The g_{33} and relative permittivity values of the photonically sintered PZT film are 22.1×10^{-3} V-m/N and 2640, respectively, which also are better than thermally sintered film. This enhanced performance of photonically sintered film is attributed to the elimination of the secondary phase as mentioned in the Chapter 3.3. Moreover, by comparing all four groups listed in the Table 3-7, the nano-scaled powder based film shows superior piezoelectric properties to those micro-scaled groups sintered using the same technique, and the photonically sintered nano-scaled powder based film yields the best piezoelectric properties. This matches the sintering tempearture results shown in the Fig. 3-22 that the nano-scaled powders could form a more compacted and denser film at the same firing temperature than micro-scaled powders resulting in superior piezoelectric performance. Consequently, by reducing the powder size, adding the sintering aid, and optimizing the sintering parameters, a quality sintering was achieved throughout the entire film thickness, and the further enhanced piezoelectric properties were obtained.

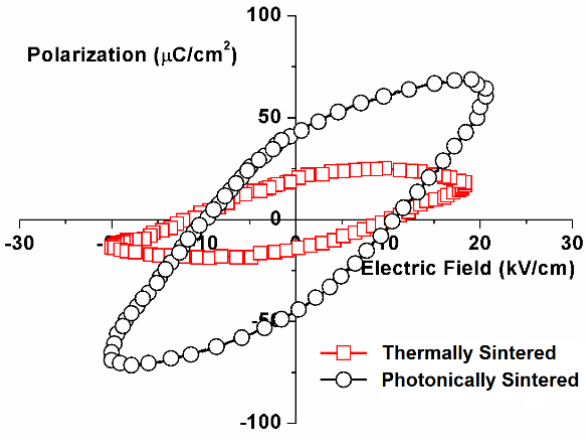

Figure 3-29. Polarization-electric field hysteresis loop of thermally (red) and photonically (black) sintered nano-scaled PZT powder based film. The remanent polarization (P_r) and the coercive field (E_c) are 43.9 μC/cm^2 and 9.8 kV/cm, respectively, for the photonically sintered films. These results are superior than those of thermally sintered group.

Table 3-7. The electrical properties of micro-sized and nano-sized particle based PZT films.

Powder	Sintering	P_r (μC/cm^2)	E_c (kV/cm)	g_{33} (10^{-3} V-m/N)	ε_r
Micro	Thermal	17.1	6.3	16.9±1.0	1271±159
Micro	Photonic	32.4	6.7	17.9±0.8	1615±212
Nano	Thermal	17.7	10.8	21.3±1.4	1810±246
Nano	Photonic	43.9	9.8	22.1± 2.0	2640±305

3.5. Conclusions

Deposition, sintering, and poling are three key steps of preparing a PZT film device. This chapter introduces few popularly and widely used approaches for each step. Then a new PZT thick preparation process was introduced: Aerosol jet printing technique was used to obtain the desired thick PZT films. This technique provides the opportunity of directly creating complex PZT features that have previously been difficult to achieve. The photonic sintering method was adopted to sinter PZT thick film on the stainless steel substrate in a short duration with low temperature increase measured on the substrate. This processing technique eliminates the oxidation of the substrate metallic material, allows sintering PZT in atmospheric environment, reduces the pyrochlore phase to enhance the piezoelectric properties, and lowers the substrate temperature increase during the sintering. It accordingly expands the substrate material options and opens the possibility of directly fabricating PZT films on low temperature substrates without complex film transfer processes traditionally required for these materials. The ferroelectric piezoelectric properties of photonically and thermally sintered PZT films were measured, demonstrating enhanced PZT characteristics with photonic sintering. The photonic sintering quality of the films along X-Y direction is comparable with thermally sintering. However, due to the temperature gradient, quality sintering does not extend throughout the entire film thickness. A further optimization of the film sintering quality throughout the PZT film thickness was accordingly carried out by reducing the powder size, adding the sintering aid, and analyzing the sintering parameters using DOE approach. The further improvement of piezoelectric properties was obtained in the fully photonically sintered PZT film.

References:

[1] T. Kobayashi and R. Maeda, "Piezoelectric optical micro scanner with built-in torsion sensors," *Japanese Journal of Applied Physics*, vol. 46, p. 2781, 2007.

[2] M. Koch, A. Evans, and A. Brunnschweiler, "The dynamic micropump driven with a screen printed PZT actuator," *Journal of Micromechanics and Microengineering*, vol. 8, p. 119, 1998.

[3] J. J. Ruan, A. V. Quintero, P. Janphuang, D. Isarakorn, D. Briand, and N. F. de Rooij, "PZT thick sheet on flexible plastic substrate for vibration energy harvesting," in *Proceedings of Power MEMS 2011*, 2011, pp. 151-154.

[4] R. Seveno, P. Limousin, D. Averty, J.-L. Chartier, R. Le Bihan, and H. Gundel, "Preparation of multi-coating PZT thick films by sol–gel method onto stainless steel substrates," *Journal of the European Ceramic Society*, vol. 20, pp. 2025-2028, 2000.

[5] G. Balonek. Coating a Grating Structure Using Various Deposition Techniques. Available: http://www.optics.rochester.edu

[6] R. Bouregba, G. Poullain, B. Vilquin, and H. Murray, "Orientation control of textured PZT thin films sputtered on silicon substrate with TiO_x seeding," *Materials research bulletin*, vol. 35, pp. 1381-1390, 2000.

[7] K. Wang, "Laser based fabrication of graphene," *Advances in Graphene Science*, InTech, 2013

[8] ANDOR, "Pulsed laser deposition," Available: http://www.andor.com

[9] J. S. Horwitz, K. S. Grabowski, D. B. Chrisey, and R.E. Leuchtner, "In situ deposition of epitaxial PbZr.Ti(1-x)O3 thin films by pulsed laser deposition," *Applied Physics Letters*, vol. 59, pp. 1565-1567, 1991.

[10] A. Hobby. (1997). Screen Printing for The Industrial User. Available: http://www.gwent.org/gem_screen_printing.html

[11] R. Maas, M. Koch, N. Harris, N. White, and A. Evans, "Thick-film printing of PZT onto silicon," *Materials Letters*, vol. 31, pp. 109-112, 1997.

[12] A. Frood, S. Beeby, M. Tudor, and N. White, "Photoresist patterned thick-film piezoelectric elements on silicon," *Journal of Electroceramics*, vol. 19, pp. 327-331, 2007.

[13] S. Okamura, R. Takeuchi, and T. Shiosaki, "Fabrication of ferroelectric Pb (Zr, Ti) O_3 thin films with various Zr/Ti ratios by ink-jet printing," *Japanese Journal of Applied Physics*, vol. 41, p. 6714, 2002.

[14] T. Wang and B. Derby, "Ink‐Jet Printing and Sintering of PZT," *Journal of the American Ceramic Society*, vol. 88, pp. 2053-2058, 2005.

[15] Y. Zhang, C. Liu, and D. Whalley, "Direct-write techniques for maskless production of microelectronics: A review of current state-of-the-art technologies," in *Electronic Packaging Technology & High Density Packaging, 2009. ICEPT-HDP'09. International Conference on*, 2009, pp. 497-503.

[16] J. A. Paulsen and J. M. Renn "Maskless printing of miniature polymer thick film resistors for embedded applications," in *IPC 3rd International Conference on Embedded Technology*, vol. 2, 2006.

[17] V. Tajan, P. Gonnard, and M. Troccaz, "Elaboration of PZT thick films by screen printing," in *3rd International Conference on Intelligent Materials*, 1996, pp. 564-569.

[18] C. Sangsubun, M. Naksata, A. Watcharapasorn, T. Tunkasiri, and S. Jiansirisomboon, "Optimal Fabrication and Sintering Properties of PZT Ceramics from Sol-Gel Powder."
[19] R. Dorey and R. Whatmore, "Electroceramic thick film fabrication for MEMS," *Journal of Electroceramics*, vol. 12, pp. 19-32, 2004.
[20] D. Corker, R. Whatmore, E. Ringgaard, and W. Wolny, "Liquid-phase sintering of PZT ceramics," *Journal of the European Ceramic Society*, vol. 20, pp. 2039-2045, 2000.
[21] T. Futakuchi, K. Nakano, and M. Adachi, "Low-Temperature Preparation of Lead-Based Ferroelectric Thick Films by Screen-Printing," *Japanese Journal of Applied Physics*, vol. 39, p. 5548, 2000.
[22] F. Duval, R. Dorey, Q. Zhang, and R. Whatmore, "Lead germanium oxide sinter-assisted PZT composite thick films," *Journal of the European Ceramic Society*, vol. 23, pp. 1935-1941, 2003.
[23] X. Wang, K. Murakami, O. Sugiyama, and S. Kaneko, "Piezoelectric properties, densification behavior and microstructural evolution of low temperature sintered PZT ceramics with sintering aids," *Journal of the European Ceramic Society*, vol. 21, pp. 1367-1370, 2001.
[24] J. D. Katz, "Microwave sintering of ceramics," *Annual Review of Materials Science*, vol. 22, pp. 153-170, 1992.
[25] H.-Y. Chang, S.-Y. Cheng, and C.-I. Sheu, "Microwave sintering of ferroelectric PZT thick films," *Materials Letters*, vol. 62, pp. 3620-3622, 2008.
[26] P. K. Sharma, Z. Ounaies, V. Varadan, and V. Varadan, "Dielectric and piezoelectric properties of microwave sintered PZT," *Smart materials and structures*, vol. 10, p. 878, 2001.
[27] M. Hirose, M. Takada, H. Oka, and K. Miyabe, "Relationship between poling condition and heat resisting properties in lead zirconate titanate," *Japanese Journal of Applied Physics*, vol. 33, p. 5345, 1994.
[28] A. Kholkin and N. Setter, "Photoinduced poling of lead titanate zirconate thin films," *Applied physics letters*, vol. 71, pp. 2854-2856, 1997.
[29] Y. Ting, H. Gunawan, J.-Z. Zhong, and C.-W. Chiu, "A new poling method for piezoelectric ceramics with thick film," *Journal of the European Ceramic Society*, vol. 34, pp. 2849-2855, 2014.
[30] V. Z. Parton, "Fracture mechanics of piezoelectric materials," *Acta Astronautica*, vol. 3, pp. 671-683, 1976.
[31] Y. E. Pak, "Crack extension force in a piezoelectric material," *Journal of Applied Mechanics*, vol. 57, pp. 647-653, 1990.
[32] C. B. Sawyer and C. Tower, "Rochelle salt as a dielectric," *Physical review*, vol. 35, p. 269, 1930.
[33] H. Zhang, J. F. Li, and B. P. Zhang, "Sintering and Piezoelectric Properties of Co‐Fired Lead Zirconate Titanate/Ag Composites," *Journal of the American Ceramic Society*, vol. 89, pp. 1300-1307, 2006.
[34] S. Baba, H. Tsuda, and J. Akedo, "Thickness dependence of electrical properties of PZT films deposited on metal substrates by laser-assisted aerosol deposition," *IEEE Transactions on Ultrasonics, Ferroelectrics, and Frequency Control*, vol. 55, pp. 1009-1016, 2008.

[35] S. Pandey, A. James, C. Prakash, T. Goel, and K. Zimik, "Electrical properties of PZT thin films grown by sol–gel and PLD using a seed layer," *Materials Science and Engineering: B*, vol. 112, pp. 96-100, 2004.
[36] A. Kholkin, D. Taylor, and N. Setter, "Poling effect on the piezoelectric properties of lead zirconate titanate thin films," in *Applications of Ferroelectrics, 1998. ISAF 98. Proceedings of the Eleventh IEEE International Symposium on*, 1998, pp. 69-72.
[37] H. Shifeng, C. Jun, L. Futian, L. Lingchao, Y. Zhengmao, and C. Xin, "Poling process and piezoelectric properties of lead zirconate titanate/sulphoaluminate cement composites," *Journal of materials science*, vol. 39, pp. 6975-6979, 2004.
[38] H. G. Lee and H. G. Kim, "Ceramic particle size dependence of dielectric and piezoelectric properties of piezoelectric ceramic - polymer composites," *Journal of Applied Physics*, vol. 67, pp. 2024-2028, 1990.
[39] G. Rujijanagul, S. Boonyakul, and T. Tunkasiri, "Effect of the particle size of PZT on the microstructure and the piezoelectric properties of 0-3 PZT/polymer composites," *Journal of materials science letters*, vol. 20, pp. 1943-1945, 2001.
[40] C. A. Randall, N. Kim, J.-P. Kucera, W. Cao, and T. R. Shrout, "Intrinsic and extrinsic size effects in fine-grained morphotropic-phase-boundary lead zirconate titanate ceramics," *Journal of the American Ceramic Scociety*, vol. 500, p. 677-688, 1998.
[41] F. Xu, S. Trolier-McKinstry, W. Ren, B. Xu, Z.-L. Xie, and K. Hemker, "Domain wall motion and its contribution to the dielectric and piezoelectric properties of lead zirconate titanate films," *Journal of Applied Physics*, vol. 89, pp. 1336-1348, 2001.
[42] V. Bedekar, J. Oliver, and S. Priya, "Design and fabrication of bimorph transducer for optimal vibration energy harvesting," IEEE Transactions on Ultrasonics, Ferroelectrics, and Frequency Control, vol. 57, pp. 1513-1523, 2010.
[43] K. Lefki and G. Dormans, "Measurement of piezoelectric coefficients of ferroelectric thin films," *Journal of Applied Physics*, vol. 76, pp. 1764-1767, 1994.
[44] W. H. Rhodes, "Agglomerate and particle size effects on sintering Yttria-stabilized Zirconia," *Journal of American Ceramic Socity*, vol. 64, pp. 19-22, 1981.
[45] J. O. Ranogajec, M. I. Djuric, M. I. Radeka, and P. E. Jovanic, "Influence of particle size and furnace atmosphere on the sintering of powder for tiles production," *Ceramics-Silikáty*, vol. 44, pp. 71-77, 2000.
[46] L. B. Kong, J. Ma, W. Zhu, and O. K. Tan, "Highly enhanced sinterability of commercial PZT powders by high-energy ball milling," *Materials Letters*, vol. 46, pp. 274-280, 2000.
[47] J. R. Groza, "Nanositnering," *Nanostructured Materials*, vol. 12, pp. 987-992, 1999.
[48] L. C. De Jonghe and M. N. Rahaman, "4.1 Sintering of ceramics," *Handbook of Advanced Ceramics: Materials, Applications, Processing and Properties*, vol. 2, p. 187, 2003.
[49] W. D. Kingery, "Densification during sintering in the presence of a liquid phase. I. Theory," *Journal of Applied Physics*, vol. 30, p. 301-306, 1959.

Chapter 4 Photonically Sintered PZT Flexible Energy Harvester

4.1. Introduction

Wearable devices, such as biological signal monitors [1, 2], gesture or facial expression recognizers [3, 4], and wearable computers [5, 6], have been intensively researched. In order to operate these devices, a power source that can provide stable, reliable and continuous energy is indispensable. While most devices use a battery, this requires routine recharging or replacement. There is an opportunity to leverage the mechanical energy from human body motion or the environment to power these devices using a piezoelectric material, specifically PZT. To optimally scavenge human motion for power, the PZT should be fabricated on flexible and lightweight substrate materials that generally have a low melting point. Because of the mismatch of the PZT sintering temperature (> 800 °C) and the melting point of the substrate (< 300 °C), complicated PZT film transfer processes have traditionally been used to realize the desired device. For instance, Qi et al. transferred an array of sintered PZT ribbons from MnO substrate to pre-stretched PDMS substrate to realize a flexible and stretchable energy harvester [7]. To avoid the complex transfer process, photonic sintering technology of thin PZT films with broadband, sub-msec, high intensity pulses was explored. Yamakawa, et al. recently used a hot plate at 350 °C to preheat the substrate in combination with a photonic flash lamp with an energy of 27 J/cm^2 to successfully sinter PZT film [8]. This work developed photonic sintering method to sinter the PZT film while achieving low substrate temperature increase without substrate pre-heating, and demonstrated superior piezoelectric properties

can be obtained than conventional thermal sintered PZT film. This could eliminate the complicated PZT transfer processes. By employing this approach, a flexible energy harvester with the polyethylene terephthalate (PET) substrate (melting point = 260 °C) was realized. The electric characterization was performed and presented in this chapter.

4.2. PZT Photonic Sintering on PET Substrate

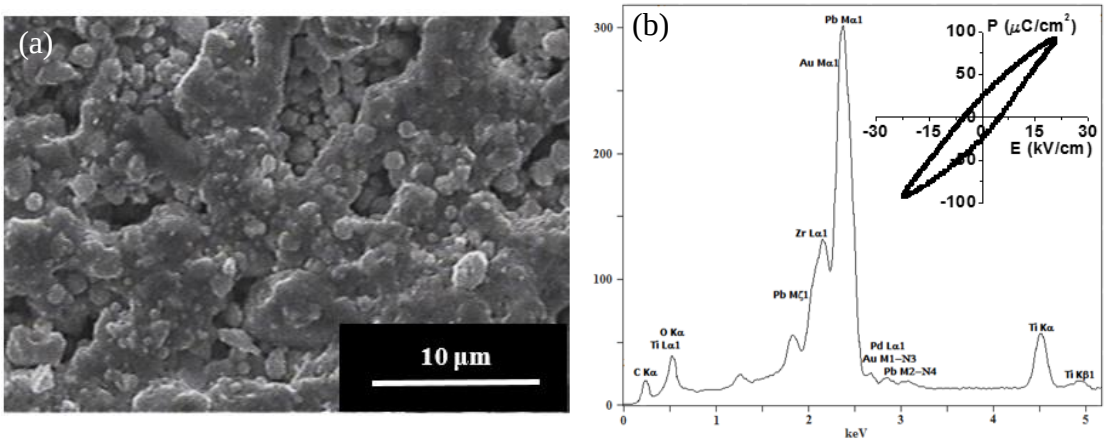

Figure 4-1. (a) The SEM image showing that the sintered particles are merged together as observed on the SS substrate. (b) The EDS spectrum shows the photonic sintered PZT film on an Al electrode and PET substrate. The spectrum shows the sintered film has low C content of approximately 15. The plot on the top right corner is hysteresis loop of PZT film on an Al electrode on PET substrate. The remanent polarization is 23.1 µC/cm^2 and the coercive field is 5.1 kV/cm. The ferroelectric test results demonstrate better performance than the thermally sintered PZT on SS.

Low temperature increase in the substrate material during photonic sintering has been demonstrated in the Chapter 3.3. Therefore, it provides the possibility of performing the photonic sintering of PZT directly on a low melting point substrate. To demonstrate the feasibility, a 70 µm thick polyethylene terephthalate (PET) substrate with a melting point of 260 °C was tested. The PET sheet was heat treated at 200 °C in an atmospheric oven for 30 minutes prior to PZT printing to relieve the stress introduced by the calendaring manufacture process. The sample was slowly cooled to room temperature within the oven. In order to create a bottom electrode for electrical characterization, a 500 nm Al film was sputtered on the PET using the CVC 601 sputtering system. The PZT film was Aerosol Jet printed on top of the deposited Al layer and photonically sintered as described for the stainless steel (SS) substrates using parameter combination: applied voltage (250 V), pulse duration (1300 µs), pulse frequency (2 Hz) and number of pulses (N=15). The resulting

SEM image and EDS are shown in Fig. 4-1 (a) and (b). The particle structure is similar to that obtained on the SS substrate presented in the Chapter 3. The low carbon content shown in the EDS spectrum, and merged particles shown in the SEM image indicate the PZT film sintering was successful. Inspection of the PET substrate after photonic sintering revealed no structural damage or indications of localized transitions in the substrate material. The resulting ferroelectric hysteresis loop is shown in Fig. 4-1 (b), with measured P_r and E_c of 23.1 μC/cm^2 and 5.1 kV/cm, respectively. The remanent polarization was improved over those observed for the thermally sintered films (17.1 μC/cm^2), likely due to the greater degree of surface particle consolidation at the film surface and weaker secondary phase. However, the remanent polarization is weaker than that photonically sintered group with the SS substrate (32.4 μC/cm^2). This may be attributed to the different thermal conductivity of the substrates: Al (~205 W/(m-K)) and SS (~ 26 W/(m-K)). The higher thermal conductivity of Al results in enhanced heat transferred from the PZT film to the underlying Al film and to the environment. Therefore, less energy was contributed to heating the PZT film leading to weaker sintering. The measured g_{33} and relative permittivity of the photonic sintered film were 17.3×10^{-3} V-m/N and 1395.4, respectively, which exceed those of the thermally sintered film (16.9×10^{-3} V-m/N and 1273.5, respectively) indicating superior sintering on this low melting point substrate. However, these differences may be within anticipated error due to processing and measurement as described in Chapter 3 for the SS substrate samples. Additionally, the PET substrate was slightly bent due to the intrinsic tensile stress of the deposited Al layer [9] and thermal stress induced from PZT drying and the sintering process. Therefore, bending of the PET may contribute a small amount of stress from punch of the piston. These factors may have resulted in a higher g_{33} measured value.

4.3. Flexible Energy Harvester Fabrication

The PZT was aerosol-jet printed and photonically sintered on a PET substrate using the process described in the Chapter 3.3. Silver electrodes were patterned on top of PZT using an Ink-Jet printer (DMP-2831, FUJIFILM Dimatix, Inc., USA) and photonically sintered, as well. Since for PZT the d_{33} mode is approximately twice as large as the d_{31} mode [8], an interdigitated electrode structure was utilized to maximize the output signal

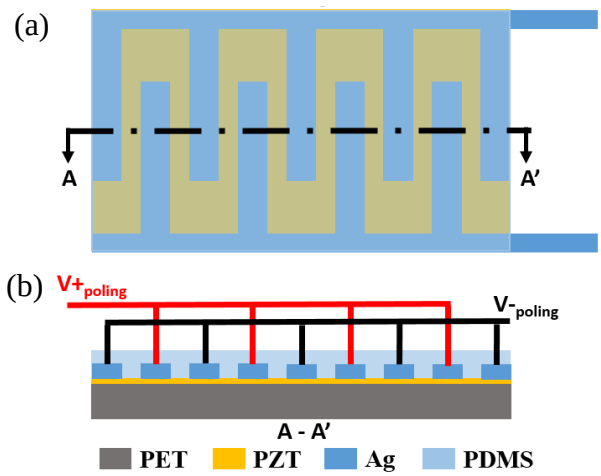

Figure 4-2. Schematic of top (a) and cross-sectional (b) views of the PZT energy harvester. The interdigitated electrode structure results in a poling direction parallel to the PZT surface.

obtained from the energy harvester. In order to protect the device, a layer of Polydimethylsiloxane (PDMS) (Dow Corning Co., USA) was coated the top surface. An illustration and optical image of the PZT energy harvester are shown in Fig. 4-2 and Fig. 4-3, respectively. The size (length × width × thickness) of the fabricated device was 15.5 mm × 13.5 mm × 0.2 mm. Silver epoxy (EJ2198, Epoxy Technology, Inc., USA) was used to connect the device to wires for poling and electric testing. The device was then poled with an electric field of 30 kV/cm at 180 °C in atmospheric environment for 2 hours before piezoelectric characterization measurements.

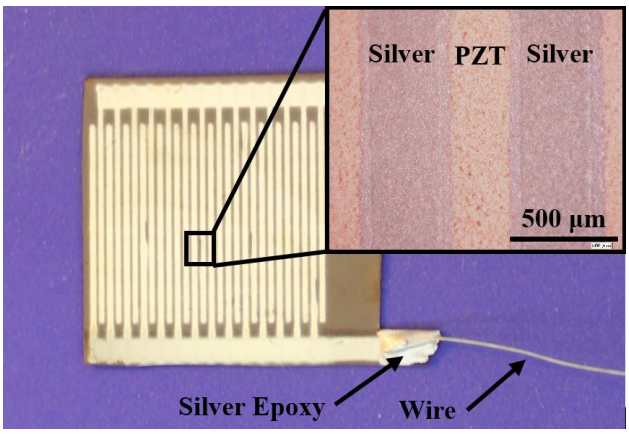

Figure 4-3. Optical image of the fabricated device (without coating PDMS layer). The PZT film was printed on transparent PET, and interdigitated silver electrodes were Ink-Jet printed on top of the PZT layer. The inset image shows the photonically sintered silver electrodes on the sintered PZT film.

4.4. Deforming Stress Simulation

Mechanical finite element simulation was carried out in COMSOL 4.3a to study the stress induced in the PZT film when the energy harvester was deformed. The material parameters used in the simulation are listed in Table 4-1.

Table 4-1. Material parameters used in COMSOL simulation.

Parameters	Value	Unit
Young's modulus of PET	1.41×10^{10}	Pa
Poisson's ratio of PET	0.44	
Young's modulus of PZT	5.1×10^{10}	Pa
Poisson's ratio of PZT	0.3	
Young's modulus of PDMS	7.5×10^{5}	Pa
Poisson's ratio of PDMS	0.49	

The COMSOL simulation model was built as a PZT layer (thickness = 18.7 μm) sandwiched between the bottom PET layer (thickness = 80 μm) and top PDMS layer (thickness = 100 μm). In the experiment, a stage with one moving side (right) and one fixed side (left) was used to apply displacement to bend the device. Therefore, in the simulation, one end of the device was fixed (left) while the other end (right) translated in the x-axis compressing the device and inducing central flexure in the y-axis as shown in Fig. 4-4 (a). The resulting stress in the PZT layer was estimated (Fig. 4-4 (b)), with up to 145 MPa tensile stress at the location of greatest deflection (*d*). Notice the greatest tensile stress at the top surface and the greatest compressed stress at the bottom surface in the PZT layer are not equal. This is because the PZT is sandwiched in between PET and PDMS. However,

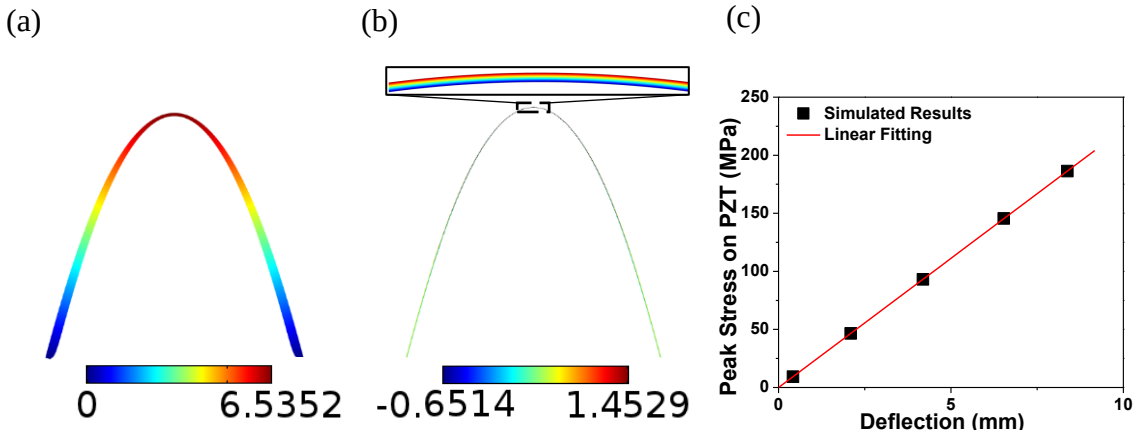

Figure 4-4. Mechanical finite element simulation results. Device deflection results in the positive y direction (a) with color indicating vertical displacement is 6.5 mm. The resulting stress in PZT film only is shown in (b) with the highest stress (145 MPa) at the location of greatest deflection. A linear relation between the highest tensile stress of the PZT layer and the deflection was obtained from the simulation (c). Based on this relation, the stress in the PZT film can be estimated by measuring the maximal deflection (*d*) of the device in the experiments.

PET is stiffer than PDMS. Therefore, the neutral axis (zero stress axis) of the entire device is not at the middle of the device thickness. Instead, it locates closer to the harder material (i.e. PET). The peak tensile stress increased linearly with *d* as shown in Fig. 4-4 (c). This result was used to estimate the tensile stress in PZT film based on measurement of the maximal deflection of the device (*d*).

4.5. Piezoelectric Experimental Results

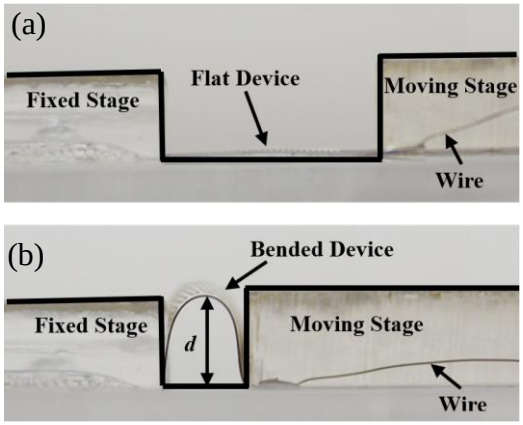

Figure 4-5. Photographs of the PZT energy harvester in the flat (a) and bended (b) states. The moving stages are highlighted with black lines for clarity. In this figure, the induced device deflection (*d*) was approximately 6.5 mm corresponding to approximately 145 MPa tensile stress at the greatest deflection location.

The piezoelectric response of the PZT energy harvester was characterized after poling by bending the device using a linear moving stage as shown in Fig. 4-5. An oscilloscope (TDS 2014B, Tektronix, Inc., USA) was used to record the output signal in all experiments. The position of the left side of the stage was fixed, with translation of the right side to induce flexure. The resulting open circuit voltage is plotted in Fig. 4-6.

Based on the simulation result, the highest tensile stress on the PZT layer was estimated by measuring the maximal deflection (*d*) of the device via ImageJ. The output open-circuit voltage corresponding to the peak tensile stress from the PZT film is shown in Fig. 4-7, with a positive linear relation between the output signal and stress obtained (R^2 = 0.88). The greatest voltage obtained was 2.4 V with an applied stress of approximately 145 MPa.

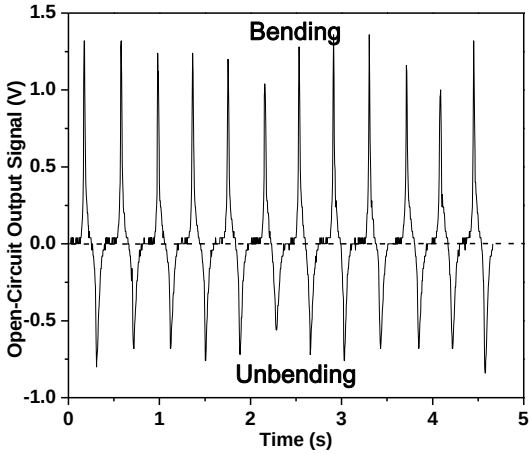

Figure 4-6. Open-circuit output signal in response to the reciprocated bending-unbending device deformation. Drive frequency was approximately 2.5 Hz.

Capacitance (C_{EH}) of the PZT energy harvester was measured using a simple RC circuit to analytically determine the optimal

load impedance (Z). A 10 kΩ resistor was connected with the device in series. A square wave generated from a signal generator (33120A, Agilent Technologies, USA) with 10 Hz frequency drove the circuit. The measured time constant (τ) of this RC circuit was approximately 60 μs. Therefore, the C_{EH} of the energy harvester can be calculated as 6 nF via Eq. 4-1.

$$\tau = RC_{EH} \qquad (4\text{-}1)$$

where R equals 10 kΩ. The load impedance for maximum power transferred from energy harvester to the load can be estimated by Eq. 4-2 [10]

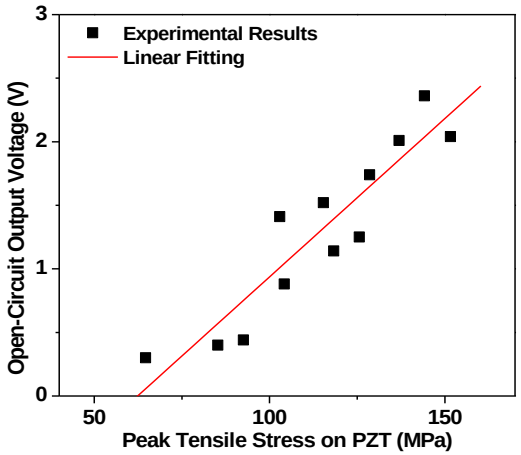

Figure 4-7. Open-circuit output voltage increases linearly with induced stress in the PZT film. Up to 2.4V was obtained with an applied stress of 145 MPa

$$\mathrm{Z} = \frac{1}{2\pi f C_{EH}} \qquad (4\text{-}2)$$

where f is the driving frequency (i.e. 2.5 Hz in this experiment). Therefore, the calculated load impedance for maximal power is 10.6 MΩ.

In order to investigate the effective power output of the PZT energy harvester, the device was connected with various series resistive loads ranging from 10 kΩ to 50 MΩ with a fixed stress of approximately 145 MPa (corresponding to ~ 6.5 mm deflection) using a rectifying circuit shown in Fig. 4-8 (a). By measuring the voltage on load, the power was calculated by Eq. 4-3.

$$\mathrm{P} = \frac{V^2}{R} \qquad (4\text{-}3)$$

where V is the RMS (Root Mean Square) value of the measured voltage signal on load. R is resistance of the load. P is the power generated from PZT energy harvester. The experimental results are plotted in Fig. 4-8 (b).

Consequently, 0.1 μW was generated when connected the PZT energy harvester to a 10 MΩ load. This matches well to the analytical load impedance result and has approximately equal performance to the proposed flexible PZT energy harvesters by Wu et al [11] (0.12 μW). However, it is lower than the device reported by Park et al [12] (12.25

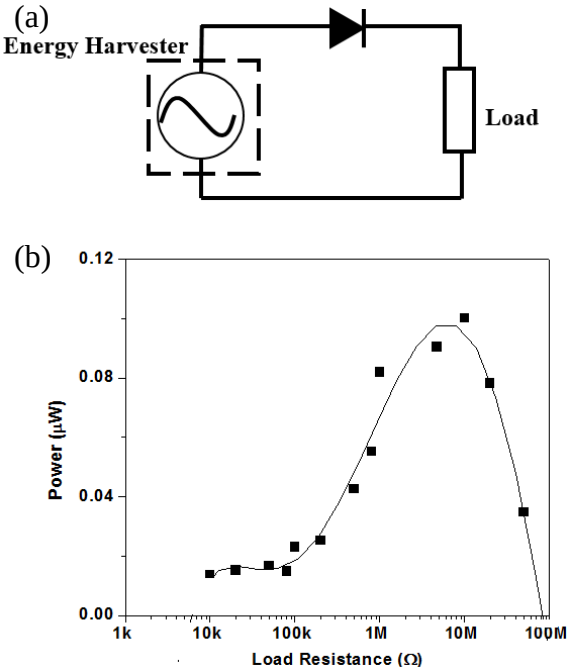

Figure 4-8. (A) Rectifying circuit used for determination of power delivered to different load resistors. (B) The measured output power delivered to different load resistances ranging from 10 kΩ to 50 MΩ with a peak stress of approximately 145 MPa. The output power is gradually building up with resistance increase. Up to 0.1 μW was generated when the energy harvester was connected to a 10 MΩ load.

μW). The possible reasons are: firstly, lower poling field was used in this experiment (30 kV/cm versus 100 kV/cm used in Park's work); secondly, the sintering energy was controlled to protect the substrate without burning. Therefore, it was not high enough to penetrate the entire PZT film, resulting in sintering quality gradient throughout the film thickness direction. The porous film at the interface can negatively affect the piezoelectric properties of the PZT film. Increasing the poling electric field strength and well optimizing the sintering parameters to achieve a superior sintered film offer opportunities to significantly improve piezoelectric performance. Moreover, sol-gel processed PZT film gives a more compacted film, which could also improve the generated energy. In addition, the ink-jet printed electrodes width has a variation of approximately 80 μm, which limited the sintering electric field to low strength. Using other electrodes patterning technology, such as photolithography and etch process [13], lift-off process [14] or microstamping [15], would achieve more uniform electrode width and further enhance the poling process and piezoelectric performance.

4.6. Conclusions

This chapter firstly demonstrates the feasibility of processing PZT directly on the low melting point substrate (PET). The measured piezoelectric and ferroelectric properties are superior to aforementioned thermally sintered PZT films. Then an Aerosol-Jet printed PZT energy harvester directly sintered on a low melting point substrate using photonic sintering

technology in less than 1 millisecond is reported. Interdigitated silver electrodes were Ink-Jet printed on top of the PZT film to leverage the more sensitive d_{33} mode to improve the output signal. The piezoelectric response was characterized by bending the device with the expected linear relation between open-circuit output voltage and applied stress obtained. Up to 2.4 V was measured at 145 MPa stress level. Using a fixed stress of approximately 145 MPa, the power versus load was determined by connecting the device with various series resistive loads. Higher power can be generated while connected with larger loads. Up to 0.1 μW was obtained while connected to a 10 MΩ load. Photonic sintering technology avoids complicated PZT transfer process to low melting and flexible substrate. Consequently, it dramatically expands the possible substrate materials for PZT energy harvesters and shortens the fabrication time.

References:

[1] M. Di Rienzo, F. Rizzo, G. Parati, G. Brambilla, M. Ferratini, and P. Castiglioni, "MagIC system: A new textile-based wearable device for biological signal monitoring. Applicability in daily life and clinical setting," in *Engineering in Medicine and Biology Society, 2005. IEEE-EMBS 2005. 27th Annual International Conference of the*, 2005, pp. 7167-7169.

[2] E. S. Winokur, M. K. Delano, and C. G. Sodini, "A wearable cardiac monitor for long-term data acquisition and analysis," *Biomedical Engineering, IEEE Transactions on*, vol. 60, pp. 189-192, 2013.

[3] J. Scheirer, R. Fernandez, and R. W. Picard, "Expression glasses: a wearable device for facial expression recognition," in *CHI'99 Extended Abstracts on Human Factors in Computing Systems*, 1999, pp. 262-263.

[4] T. Starner, J. Weaver, and A. Pentland, "A wearable computer based american sign language recognizer," in *Assistive Technology and Artificial Intelligence*, ed: Springer, 1998, pp. 84-96.

[5] A. Smailagic, D. Siewiorek, and D. Reilly, "CMU wearable computers for real-time speech translation," *Personal Communications, IEEE*, vol. 8, pp. 6-12, 2001.

[6] Y. Bai, C. Li, Y. Yue, W. Jia, J. Li, Z.-H. Mao, and M. Sun, "Designing a wearable computer for lifestyle evaluation," in *Bioengineering Conference (NEBEC), 2012 38th Annual Northeast*, 2012, pp. 93-94.

[7] Y. Qi, J. Kim, T. D. Nguyen, B. Lisko, P. K. Purohit, and M. C. McAlpine, "Enhanced piezoelectricity and stretchability in energy harvesting devices fabricated from buckled PZT ribbons," *Nano letters*, vol. 11, pp. 1331-1336, 2011.

[8] K. Yamakawa, K. Imai, O. Arisumi, T. Arikado, M. Yoshioka, T. Owada, and K. Okumura, "Novel Pb (Ti, Zr) O3 (PZT) crystallization technique using flash lamp for ferroelectric RAM (FeRAM) embedded LSIs and one transistor type FeRAM devices," *Japanese journal of applied physics*, vol. 41, p. 2630, 2002.

[9] E. Eiper, R. Resel, C. Eisenmenger-Sittner, M. Hafok, and J. Keckes, "Thermally-induced stresses in thin aluminum layers grown on silicon," *Powder Diffraction*, vol. 19, pp. 74-76, 2004.

[10] J. Park, D. Lee, J. Park, Y. Chang, and Y. Lee, "High performance piezoelectric MEMS energy harvester based on D33 mode of PZT thin film on buffer-layer with PBTIO3 inter-layer," in *Solid-State Sensors, Actuators and Microsystems Conference, 2009. TRANSDUCERS 2009. International*, 2009, pp. 517-520.

[11] W. Wu, S. Bai, M. Yuan, Y. Qin, Z. L. Wang, and T. Jing, "Lead zirconate titanate nanowire textile nanogenerator for wearable energy-harvesting and self-powered devices," *ACS nano*, vol. 6, pp. 6231-6235, 2012.

[12] K. I. Park, J. H. Son, G. T. Hwang, C. K. Jeong, J. Ryu, M. Koo, I. Choi, S. H. Lee, M. Byun, and Z. L. Wang, "Highly‐Efficient, Flexible Piezoelectric PZT Thin Film Nanogenerator on Plastic Substrates," *Advanced Materials*, vol. 26, pp. 2514-2520, 2014.

[13] H. G. Yu, L. Zou, K. Deng, R. Wolf, S. Tadigadapa, and S. Trolier-McKinstry, "Lead zirconate titanate MEMS accelerometer using interdigitated electrodes," *Sensors and Actuators A: Physical*, vol. 107, pp. 26-35, 2003.

[14] Y. Jeon, R. Sood, J.-H. Jeong, and S.-G. Kim, "MEMS power generator with transverse mode thin film PZT," *Sensors and Actuators A: Physical*, vol. 122, pp. 16-22, 2005.
[15] A. Takakuwa, M. Ikawa, M. Fujita, and K. Yase, "Micropatterning of electrodes by microcontact printing method and application to thin film transistor devices," *Japanese journal of applied physics*, vol. 46, p. 5960, 2007.

Chapter 5 Pulsed Flash Manipulation of Piezoelectric Properties of PZT Films

5.1. Introduction

Sintering and dipole reorientation (or poling) are two necessary steps of the fabrication of ferroelectric film devices to enhance the ferroelectric properties. Generally, these two steps are separately processed, which requires long processing duration and increases the complexity. The pulsed photonic sintering was demonstrated to create rapid temperature transients that were constrained to the target PZT film to achieve the high quality film sintering and piezoelectric properties enhancement [1]. The flash light used in this technique provided the optical condition for photo-assisted PZT poling, which has been demonstrated to enhance the piezoelectric property of the poled PZT films [2]. Moreover, with the application of the electric field, dipoles can form along more preferred orientation in the PZT film during the transition from cubic to tetragonal/orthorhombic while the temperature reduced from above to below Curie temperature due to the high mobility [3] and lower interdomain stress [4]. This can certainly enhance piezoelectric properties of the PZT film. The rapid temperature changes accomplish the cyclic temperature excursions in the PZT film to above and below the Curie temperature, which provides the aforementioned temperature condition for dipole reorientation and creates the opportunity for the simultaneous performance of poling during photonic sintering. Improved piezoelectric properties are expected via this technique.

This chapter is focused on the demonstration of performance of dipole reorientation during photonic sintering to further enhance the piezoelectric properties and shorten the procession duration. The film was characterized using g_{33} and relative permittivity.

Piezoelectric charge coefficient, d_{33}, was also calculated using Eq 1-9. The piezoelectric properties of 5 control PZT film groups prepared using different approaches were used for the comparison. The results and discussions are presented.

5.2. Experiment

In order to apply an electric field to the PZT film during photonic sintering without blocking the flash transfer, a transparent top electrode was required. Indium tin oxide (ITO) gives rise to high interest in semiconductor field as transparent ohmic contact, specifically for many optoelectronic applications, because of its relatively high transparency and low resistivity [5]. Therefore, ITO glass slide (ITO-111-25, Nanocs Inc., Boston, MA) with 0.5~0.7 μm ITO layer resulting in 10 Ω/sq sheet resistance was used to serve as the top electrode. However, as shown in the light absorption spectrum (Fig. 5-1), the ITO glass slide has the greatest absorbance in the ultraviolet region, which could interfere the flash energy transferred to the PZT film negatively affecting the PZT film sintering quality. Moreover, due to the light absorption of ITO layer, it also would be heated up and possibly be burned to lose the conductivity. Therefore, a re-optimization of sintering parameters was required for this specific application, so that lower photonic energy can be used to both protect the ITO layer from burning out to lose the function and to sinter PZT film throughout the entire film. The sintering parameters optimization DOE was performed on 7 mm × 7 mm× 0.006 mm PZT films (printed using the nano-scaled powder based ink) with SS substrates and

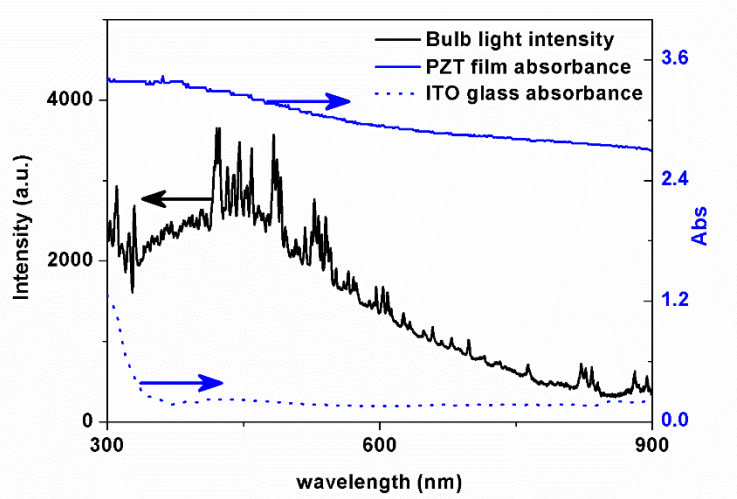

Figure 5-1. The light intensity spectrum of the Novacentrix bulb generated at 600 V level pulse setting (black), with a peak emission in the violet regime. The dried PZT film light absorbance spectral curve (blue) has significant overlap with bulb emission, with the greatest absorbance in the ultraviolet (< 400 nm). However, the ITO glass slide has the greatest absorbance in the ultraviolet region. This could affect the effective energy transferred to the PZT film.

described in the Appendix D. The optimized parameter combination yielded as applied voltage = 600 V, pulse duration = 130 μs, pulse frequency = 2 Hz, number of pulses = 23, and number of cycles = 2. This parameter combination resulted in an energy density of 2.75 J/cm^2 delivered out from the lamp. However, due to the light absorption of the ITO layer, the effective energy density transferred to the target PZT film for each pulse was only 1.90 J/cm^2 (total = 87.4 J/cm^2) measured by a pulsed light energy meter (BX-100, Novacentrix, USA). The light intensity spectrum of the photonic sintering bulb generated at 600 V pulse setting is shown in the Fig. 5-1. It has the peak emission in the violet regime, which has significant overlap with the dried PZT film light absorbance.

The 7 mm × 7 mm× 0.006 mm PZT films for the experiments were then prepared using aerosol jet printing on the SS and dried at 200 on the hotplate for 2 hours. The dried films were divided into six groups and were processed using different sintering and poling technique combinations. These six groups are introduced hereinafter in detail.

The piezoelectric properties manipulation system setup is shown in Fig. 5-2. The SS substrate of the PZT film was served as the bottom electrode for poling. The ITO glass slide was served as the top electrode with ITO layer facing down to cover the PZT film. In order to avoid electrodes contact, a Kapton tape (thickness = 60 μm, width = 12 mm) was used to serve as the insulator shown in the Fig. 5-2 to separate the top and bottom electrodes. A plain glass slide (thickness = 1 mm) (Thermo Fisher Scientific, Inc., USA) was placed between bottom stainless steel electrode and photonic sintering tool stage to avoid

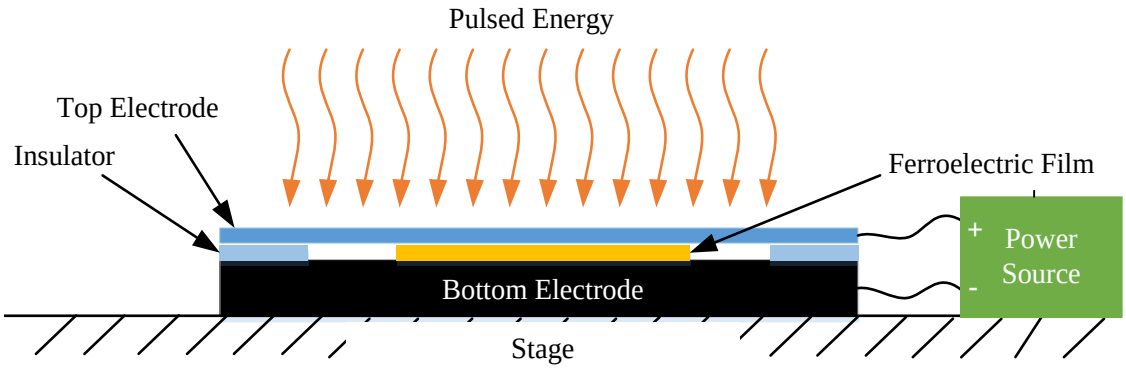

Figure 5-2. The setup for photonic sintering the PZT film with poling. The PZT film was sandwiched between top and bottom electrodes. Photonic flashes were transferred through the transparent top ITO glass electrode to create a rapid temperature transient in the film. Simultaneously, the electric field is continuously applied to the sample to reorient the electric dipoles in the PZT film.

electrical shorting. During photonic sintering, an electric field (20 kV/cm) was applied from the power source through the top and bottom electrodes to the PZT film to reorient the electric dipoles.

For the comparison purpose, few control groups were prepared using different sintering and poling technique combinations. In order to investigate the effect of the sintering techniques on the piezoelectric properties, thermal sintering technique (TS) and photonic sintering technique (PS) were studied. Conventional poling method (CP) was used to compare with the poling while photonic sintering technique (PP) to study the poling techniques effect on the piezoelectric properties:

1. **TS-CP-1hr**

   This group was thermally sintered (TS) at 1000℃ for 1 hour in the N_2 environment. After overnight resting at room temperature to relieve the stress, the films were coated with a layer of silver epoxy (EJ2189, Epoxy Technology, Inc, Billerica, MA) that served as the top electrode (5×5 mm^2). Then the films were poled at a temperature of 170℃ for 1 hour with an electric field of 20 kV/cm (CP-1hr).

2. **PS-CP-1hr**

   This group was sintered photonically (PS, without ITO glass on top) at the sintering condition: Voltage = 400 V; Pulse Duration = 650 μs; Frequency = 2 Hz; Number of Pulses = 20; Number of Cycles = 2. This parameter combination results in an energy density of 5.06 J/cm^2 (total energy = 202.4 J/cm^2) delivered to the PZT film for each pulse, which gave a good sintering quality as described in the Chapter 3.6. After overnight resting at room temperature, the films were coated with a layer of silver epoxy that served as the top electrode (5×5 mm^2). Then the films were poled at a temperature of 170℃ for 1 hour with an electric field of 20 kV/cm (CP-1hr).

3. **PS-PP**

   This group was prepared via the poling (PP) while pulsed sintering (PS) process. An electric filed (20 kV/cm) was applied from the power source through the top (ITO glass with ITO layer facing down) and bottom (stainless steel substrate) electrodes to the PZT film for the purpose of reorienting the electric dipoles during sintering. Then the device was sent to the photonic sintering system with the

sintering parameters: applied voltage (600 V), pulse duration (130 μs), pulse frequency (2 Hz), number of pulses (N = 23), and number of cycles (C = 2). The effective energy delivered to the film was 1.90 J/cm^2 (total energy = 87.4 J/cm^2). After photonic sintering, the electric field was not removed until the temperature of the film was reduced to room temperature. The entire duration of the electric field application was approximately 5 minutes. The films were then coated with a layer of silver epoxy that served as the top electrode for electrical characterization.

The conventional poling method was also performed at the time-scale (5 min) that used for poling while photonic sintering approach to study the sufficient poling duration for the conventional poling method:

4. **TS-CP-5min**

   This group was sintered thermally (TS) at 1000℃ for 1 hour in the N_2 environment. After overnight resting at room temperature to relieve the stress, the films were coated with a layer of silver epoxy that served as the top electrode (5 × 5 mm^2). Then the films were poled at a temperature of 170℃ for 5 minutes with an electric field of 20 kV/cm (CP-5min).

5. **PS-CP-5min**

   This group was sintered photonically (PS, without ITO glass on top) at the sintering condition: Voltage = 400 V; Pulse Duration = 650 μs; Frequency = 2 Hz; Number of Pulses = 20; Number of Cycles = 2. After overnight resting at room temperature to relieve the stress, the films were coated with a layer of silver epoxy that served as the top electrode (5 × 5 mm^2). Then the films were poled at a temperature of 170℃ for 5 minutes with an electric field of 20 kV/cm (CP-5min).

An exploration was carried out to study if the piezoelectric properties of PS-PP processed PZT film can be further enhanced via the conventional poling method:

6. **PS-PP-CP-1hr**

   This group was prepared to investigate whether the piezoelectric property of PS-PP prepared PZT can be further enhanced. The PS-PP prepared PZT samples were further poled using conventional poling method at a temperature of 170℃ for 1

hour with an electric field of 20 kV/cm (CP-1hr).

5.3. Results and Discussions

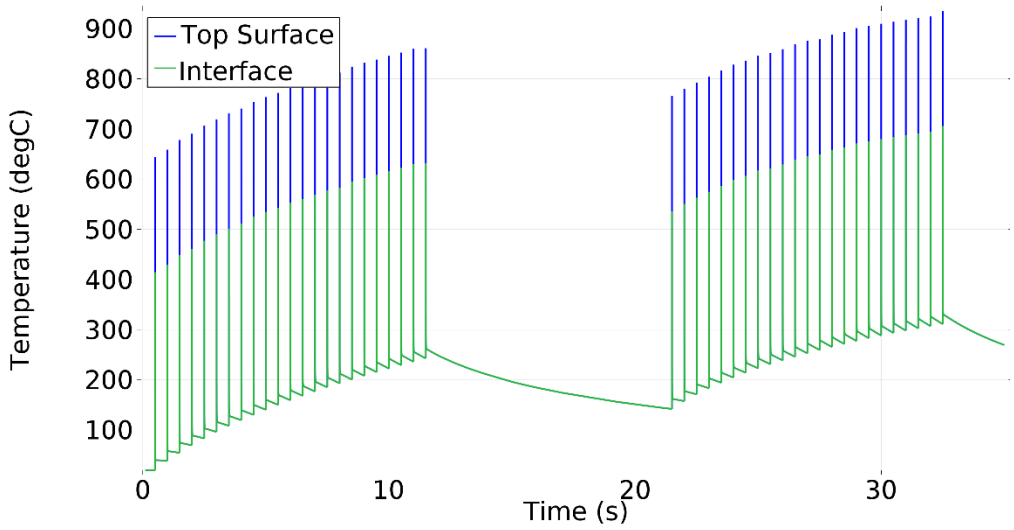

Figure 5-3. The COMSOL simulation to estimate the temperature change in the PZT film and substrate during the photonic sintering. The top surface of the PZT film reached ~ 950 °C, which is high enough to sinter the PZT powders. However, the film-substrate interface increased up to ~ 720 °C, which is lower than the required sintering temperature (~ 800 °C).

COMSOL simulation was carried out to estimate the temperature change in the PZT film and substrate during the photonic sintering. The module, material parameters, and settings used in the simulation were the same as Chapter 3. Effective sintering power, 1.9 J/cm^2 for each pulse, was used in this modeling. The result is shown in the Fig. 5-3. The top surface of the PZT film reached up to ~ 950 °C, which is high enough to sinter the PZT powders. However, the film-substrate interface increased to ~ 720 °C, which is lower than the required sintering temperature (~ 800 °C). Therefore, the sintering quality of this film was expected to be lower than the one without ITO glass. There also might be a very thin layer at the film-substrate interface that was not sintered well due to the low temperature increase.

SEM image was used to study the sintering quality of ITO glass covered PZT film as shown in the Fig. 5-5. Prior to sintering, an approximately 6 μm film was achieved with consistent thickness and uniformly distributed particles (Fig. 5-4 (a)). After the performance of photonic sintering using the updated optimal sintering parameters combination (applied voltage (600 V), pulse duration (130 μs), pulse frequency (2 Hz),

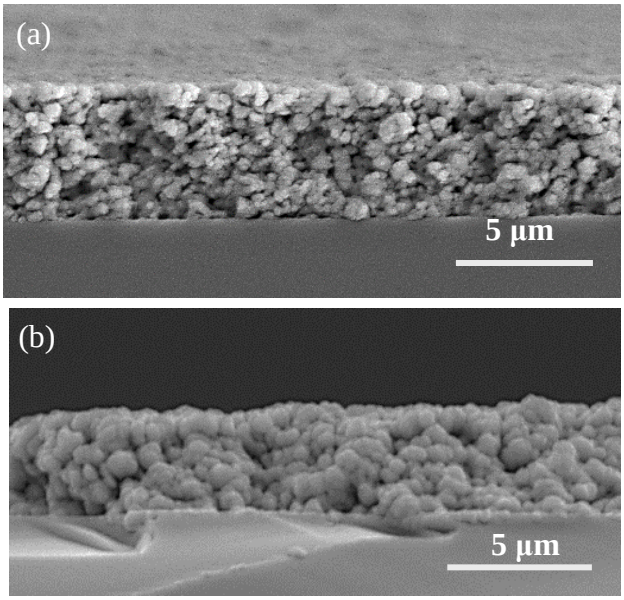

Figure 5-4. Before (a) and after (b) sintering with electric field poling. An approximately 6 µm thick PZT film was achieved prior to sintering. After the photonic sintering, a well sintered PZT thick film was obtained. Notice the particles size was increased due to the thermal expansion and powders merging.

number of pulses (N = 23), and number of cycles (C = 2). The effective energy delivered to the film was 1.90 J/cm^2 (total energy = 87.4 J/cm^2)), the particles were expanded and merged into larger sizes to densify the film (Fig. 5-4 (b)). The SEM image is revealing a well sintered film. However, in order to protect the ITO layer from burning to lose the electric conductivity and due to the light absorption of this layer, the effective sintering energy was much lower than that used without ITO glass. Therefore, the sintering quality was inferior to the one without ITO glass as described in the Chapter 3. Moreover, at the film-substrate interface, the pore size is larger than the one at the surface. This most likely is due to the temperature gradient along the thickness direction as shown in the Fig. 5-4.

The piezoelectric voltage coefficient (g_{33}) and relative permittivity (ε_r) of the six groups of sintered and poled PZT films were measured using a self-build cylinder system and an RC bridge circuit, respectively, after setting the samples aside at room temperature overnight to relieve the stress induced during poling process as mentioned in the Chapter 3.5. d_{33}, the piezoelectric charge coefficient that is the coefficient directly related to the film actuation capability (generation of the mechanical deflection in response to the electric field), was also calculated using Eq. 5-1 for the quantitative comparison.

$$d_{33} = g_{33}\varepsilon_r\varepsilon_0 \tag{5-1}$$

where ε_0 represents electric constant ($\varepsilon_0 \approx 8.854 \times 10^{-12}$ F/m). The g_{33} and ε_r used for the d_{33} calculation were averaged values.

The results of all six groups are summarized in the Table 5-1. It is noted that each result is from the average of 5 samples, and the one standard deviation is also included.

However, d_{33} values were calculated from the averaged g_{33} and ε_r. Therefore, in the table, no standard deviation is included for d_{33}. By comparing all six groups, the PS-PP prepared PZT yields the best piezoelectric properties. This demonstrates the enhancement of the piezoelectric property via performing poling during photonic sintering. The key to this enhancement is the cyclic high temperature poling. Kounga et al. already demonstrated that the saturated d_{33} value can be easily obtained via gradually reducing the temperature (6 °C/min) from well above the PZT film's Curie temperature to room temperature with the application of poling field [6]. This may be attributed to three reasons: firstly, the dipoles are formed during temperature dropped through the Curie temperature via the phase transition from paraelectric cubic to the ferroelectric tetragonal/orthorhombic. The orientations of the dipoles are so different that reach an electrically balanced state of the material while no electric field is applied during the phase transition. And then, the poling step is to provide sufficient energy to overcome the interdomain stress to reorient the dipoles along the poling direction [4]. However, with the application of the electric field, there is a preferred dipole direction built by the field. During the phase transition, dipoles will directly form along this direction without the need to overcome the interdomain stress. Therefore, higher piezoelectric properties can be obtained while using lower poling field. Secondly, the higher temperature, the higher mobility of the atoms, which facilitates the reorientation of the dipoles. Thirdly, as proposed in the [2], the UV light can induce an internal field in the PZT film to compensate the depolarization field. Therefore, high poling quality can be obtained. This poling during photonic sintering also provides the optical condition. Further enhanced piezoelectric properties were expected. Moreover, the high g_{33} (22.6×10^{-3} V-m/N) and d_{33} (626.0×10^{-12} m/V) values reveal that the PS-PP group is expecting to have the best sensing and actuation performances among all six groups. Moreover, due to lower sintering power delivered into the PZT film to protect the ITO layer, the sinteirng quality of the film along the thcikness direction was inferior to the groups without ITO glass (shown in the Chapter 3.4). An opportunity for the future is to explore alternative transparent and conductive top electrode to allow greater energy transfer into the PZT film for this proces. This could give rise to even higher piezoelectric properties as the comparison between the PS-PP processed PZT film and typical values of soft PZT [7]. By comparing the PS-PP-CP-L group ($g_{33} = 22.5 \times 10^{-3}$ V-m/N, $d_{33} = 597.2$

$\times 10^{-12}$ m/V) with the PS-PP group, it shows that both the g_{33} and d_{33} values obtained from PS-PP group cannot be further increased by post poling. This indicates the piezoelectric property achieved by PP-PS is sufficientaly high andcannot be further enhanced using conventional poling approach. More importantly, the piezoelectric coefficients were reduced after further conventional poling. This possibly can be attributed to the slight depolarization by the lower poling energy resulting from the conventional poling conditions. It should also be noted that the time dependent domain wall motion would cease to play a role at a high temperature (but below Curie temperature in order to have domains) because of extremely high mobility of the domain wall or instantaneous creation of new domain walls at such a high temperature [4]. Moreover, most of the dipoles were directly formed along the poling field direction during the phase transition, which is completed in nano second scale [8]. This is why at such a short sintering and poling duration ($\approx$ 5 min), the PS-PP group still can achieve high piezoelectric properties. However, if the temperature is not high enough, such a short poling duration is not sufficient to reorient the dipoles and to obtain high piezoelectric properties. This can be verified from that very weak piezoelectric properties (TS-CP-5min group: $g_{33} = 6.6 \times 10^{-3}$ V-m/N, $d_{33} = 21.6 \times 10^{-12}$ m/V; PS-CP-5min group: $g_{33} = 8.0 \times 10^{-3}$ V-m/N, $d_{33} = 26.4 \times 10^{-12}$ m/V) were obtined in those conventionally poled samples at the PS-PP time-scale. Lastly, as mentioned in the Chapter 3, for the given poling duration, photonically sintered samples show superior piezoelectric property to the thermally sintered samples due to the lower secondary phase (known as pyrochlore phase due to the lead loss at high sintering temperature).

Table 5-1. The piezoelectric property of six groups.

Methods	g_{33} (10^{-3} V-m/N)	d_{33} (10^{-12} m/V)	ε_r
Typical values of soft PZT [7]	23.0	660.0	3250
TS-CP-1hr	21.3 ± 1.4	341.2	1810 ± 246
PS-CP-1hr	22.1 ± 2.0	516.3	2640 ± 305
TS-CP-5min	6.6 ± 0.8	21.6	370 ± 57
PS-CP-5min	8.0 ± 1.0	26.4	373 ± 40
PS-PP	22.6 ± 1.9	626.0	3130 ± 242
PS-PP-CP-1hr	22.5 ± 2.0	597.2	2999 ± 261

5.4. Conclusions

This chapter demonstrates the feasibility of performing PZT thick film poling during photonic sintering, which results in a further enhancement of the piezoelectric property and reduction of the entire processing duration. The processing setup is presented and the sintering parameters are analyzed to obtain a dense sintered film. Six PZT film groups using different sintering and poling technique combinations are prepared. g_{33} and permittivity are measured, and d_{33} calculated to quantitatively investigate the piezoelectric properties of sintered and poled films. The PZT film prepared via poling while photonic sintering approach yields the best piezoelectric property, which cannot be further enhanced using conventional poling approach. However, at such a short poling time scale, high piezoelectric property cannot be obtained using the conventional poling method. Moreover, it demonstrates again that the PZT films using photonic sintering method is leading to higher piezoelectric property than those using thermal sintering.

References:

[1] J. Ouyang, D. Cormier, S. A. Williams, and D. A. Borkholder, "Photonic sintering of aerosol jet printed Lead Zirconate Titanate (PZT) thick films," *Journal of the American Ceramic Society*, vol. 99, pp. 2569-2577, 2016.

[2] A. L. Kholkin and N. Setter, "Photoinduced poling of lead titanate zirconate thin films," *Applied physics letters*, vol. 71, pp. 2854-2856, 1997.

[3] A. L. Kholkin, D. V. Taylor, and N. Setter, "Poling effect on the piezoelectric properties of lead zirconate titanate thin films," *Applications of Ferroelectrics, 1998. ISAF 98. Proceedings of the Eleventh IEEE International Symposium on*, IEEE, 1998.

[4] B. Jaffe, *Piezoelectric ceramics*. Elsevier, 2012.

[5] C. Coutal, A. Azéma, and J. –C. Roustan, "Fabrication and characterization of ITO thin films deposited by excimer laser evaporation," *Thin Solid Films*, vol. 288, pp. 248-253, 1996.

[6] A. B. Kounga, T. Granzow, E. Aulbach, M. Hinterstein, and J. Rődel, "High-temperature poling of ferroelectrics," *Journal of Applied Physics*, vol. 104, p. 024116, 2008.

[7] DONG IL TECHNOLOGY LTD., "Piezoelectric Materials" [online], Available: www.dongiltech.co.kr.

[8] D. Mao, B. E. Gnade, and M. A. Quevedo-Lopez, "Ferroelectric properties and polarization switching kinetic of poly(vinylidenefluoride-trifluoroethylene) copolymer," *Ferroelectrics-Physical Effects*, InTech, 2011.

Chapter 6 Conclusions and Future Work

6.1. Conclusions

This work developed processing techniques that enable piezoelectrics with superior properties to be fabricated directly on low-temperature substrates. Three photonic sintering based piezoelectric ceramic thick film fabrication processes were proposed and demonstrated with distinct benefits. The first process yields low substrate temperature increase with enhanced piezoelectric properties over the thermally sintered group due to the lower secondary phase. This allows the piezoelectric ceramic thick film be processed directly on the low temperature substrates, such as PET and Kapton. The second process provides high quality sintering throughout the entire piezoelectric ceramic thick film thickness to further improve the piezoelectric properties. However, the temperature of the film-substrate interface is high after sintering. The third process method allows performing poling during photonic sintering to further shorten the whole processing time. The piezoelectric properties are also further improved. The substrate temperature increase only reaches to ~ 700 °C, which permits employing this process to prepare the piezoelectric ceramic thick film on low melting point metal substrates, such as aluminum, magnesium, and aluminum alloy. Therefore, according to the different application requirements, proper process can be used to obtain high performance devices. This work extremely shortens the piezoelectric ceramic thick film processing time, highly expands the substrate material choice, and greatly improves the piezoelectric properties over the thermally sintered groups. Moreover, all of these high temperature sintering processes are performed in the atmospheric condition, which is not possible using conventional furnace sintering method due to the oxidation of the electrodes or substrates. This is accordingly simplifies the process.

For the process, the micro-powder based and nano-powder based PZT inks were formulated for the direct printing technique. The PZT film deposition was then realized by the aerosol jet printing. Thick PZT films were achieved by printing both micro-powder based and nano-powder based inks. The effect of the particle size and sintering aid on the PZT sintering temperature was studied. It turns out that the smaller particle size has the lower sintering temperature. And adding the sintering aid could further lower the sintering temperature. By adding the liquid phase sintering aid (Cu_2O + PbO) and using the nano-sized particle, the PZT sintering temperature was reduced to ~ 800 °C. Photonic sintering technique was used to sinter PZT film in < 1 min. After sintering, the PZT powders were fused and merged together to form a dense film. Finite element simulation was carried out to estimate the temperature change in the PZT film and the substrate. From both simulation and experiment, it was observed that the substrate temperature increase was low enough (< 200 °C). Nano-powder based film, due to the lower sintering temperature and usage of the optimized sintering parameters, obtained a high quality sintering throughout the entire thickness. Piezoelectric properties characterization systems were built to measure polarization-electric field hysteresis loop, permittivity, and piezoelectric voltage coefficient. The photonically sintered PZT films yielded the superior piezoelectric properties to the thermally sintered films. The reason can be attributed to lower pyrochlore phase observed in the photonic sintered PZT films.

Photonic sintering of PZT film opens several possibilities to realize the PZT fabrication due to the temperature gradient in the target film and extremely short processing duration: Firstly, photonic sintering of PZT film creates the opportunity to process PZT film directly on low melting point substrate. PET was used to demonstrate the PZT fabrication process on low melting point substrate. Pulse flashes successfully sintered PZT film without damage the PET substrate. After poling, the PZT film revealed enhanced piezoelectric properties, as well. By using this technique, a d_{33} mode flexible PZT energy harvester was fabricated. The bending stress in the device was modelled using COMSOL. A linear relation between the output open-circuit voltage and the maximum stress was obtained. By connecting the device with the resistive load using a rectifying circuit, the generated energy from the energy harvester was measured. Up to 0.1 μW generated energy was achieved when connected with 10 MΩ resistive load. Secondly, photonic sintering also

allows performing the PZT dipole reorientation while sintering. The feasibility of that reorient the PZT dipoles during photonic sintering was demonstrated. The comparison between this process and 5 control groups using different sintering and poling technique combination was carried out. The highest piezoelectric properties were observed in the group that was prepared using poling during photonic sintering method. This approach even further shortens the processing duration. Moreover, the substrate temperature increase (~700 °C) was still lower than those thermally sintered groups.

Photonic sintering facilitates the PZT fabrication and allows obtaining a high performance PZT film with low substrate increase. This could be helpful to the fabrication of both regular and flexible single layer PZT devices. Moreover, this also could be beneficial to the bimorph or multilayer PZT devices, because the choice of the electric conductive material that is served as the electrode layer between two PZT layers can be expanded.

6.2. Future Opportunity

The realization of performing a fully sintered PZT thick film on the low melting point substrate (Kapton or PET) is demanded for obtaining a superior flexible piezoelectric devices performance. The exploration of different flash exposure modes and pulse profiles that are available in the PulseForge is required to well control the temperature increase in the PZT film to realize a fully sintered PZT on the low temperature substrate. μPulse mode, a special mode in the PulseForge photonic sintering system, allows the users to divide each flash pulse into multiple micropulses, and control the rising and dropping time for each micropulse, enabling fine manipulation of the film temperature change with each pulse. However, over 10 separate exposure process variables have to be optimized if using this mode. And the different rising and dropping time for each micropulse would increase the difficulty and complexity of using the COMSOL simulation. SimPulse, a simulation application created and developed by NovaCentrix for modeling the PulseForge photonic curing system will be used to investigate the temperature change in the PZT film and substrate in response with different settings in the μPulse mode. Notice, a thin molten or glass transition layer of the low temperature substrate is allowed to enhance the PZT film adhesion to the substrate. A comparison of SimPulse simulated results between the

aforementioned optimized sintering parameters (i.e. voltage = 400 V; pulse duration = 650 μs; frequency = 2 Hz; number of pulses = 20) and one setting of the μPulse mode is shown in the Fig. 6-1 and Fig. 6-2 for a 6 μm thick PZT film built on a 20 μm thick Kapton substrate (melting temperature ≈ 500 °C). The PZT film temperature increases up to 2050 °C and the Kapton substrate temperature increases up to 1850°C while using the aforementioned optimized sintering parameters in only one cycle (Fig 6-1 (a)). Therefore, this parameter could certainly melt the substrate and possibly burn the PZT film. μPulse mode allows users manipulate the parameters of Voltage, μPulses (number of sub-pulses in a single flash), Envelope (exposure duration), Duty Cycle (the ramping time for the voltage (not flash energy) increases to the setting value), Fire Rate (frequency), Repeat Count (number of pulses). Fig. 6-2 (a) is showing an attempted sintering parameters used for the simulation of the μPulse mode. The power density profile resulted from this setting is shown in the Fig. 6-2 (b) for each pulse. The temperature changes at the PZT film top surface (red curve) and the PZT film-substrate interface (blue curve) for the entire exposure duration are shown in the Fig. 6-2 (c). The top surface of the PZT film temperature can increase up to >1010 °C, which is sufficiently high for the PZT film sintering. However, the PZT-substrate interface temperature increases only up to ~ 650 °C. This temperature would not only melt the substrate slightly to enhance the adhesion, but also be sufficiently high to fuse and merge the PZT particles. Experiments based on the simulation result should be carried out to verify the model. Notice that the maximal temperature increase in the both film and substrate are reached at the 10^{th} pulse and no changes after that when using the μPulse module. Therefore, one important information is needed, which is how many pulses are really required to obtain a quality sintering throughout the film. Qualitative observation using SEM images and quantitative investigation by the P-E hysteresis loop, permittivity and piezoelectric voltage coefficient are necessary to obtain the optimal number of pulses and cycles.

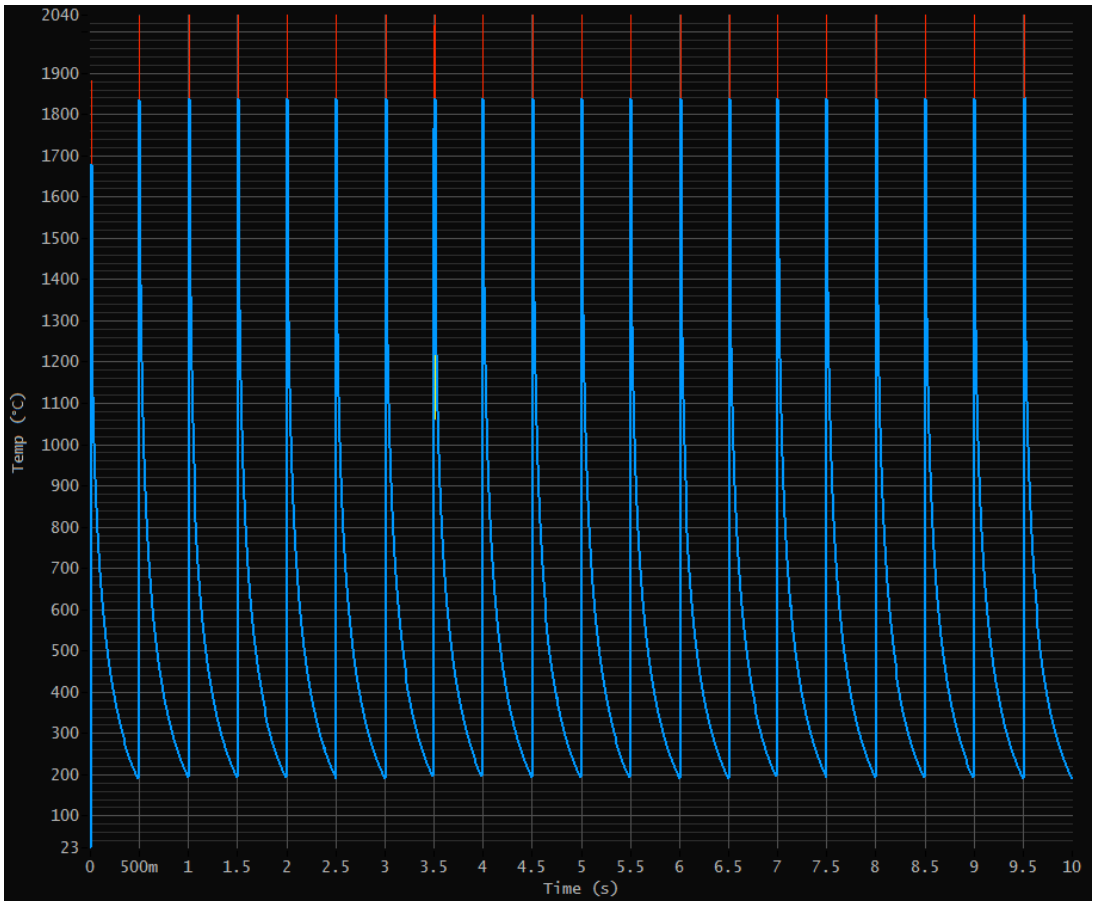

Figure 6-1. SimPulse modeling result of the temperature change for the simulation of 6 μm PZT film on the 20 μm Kapton substrate under the sintering condition: voltage = 400 V; pulse duration = 650 μs; frequency = 2 Hz; number of pulses = 20. The blue curve represents the temperature change at the Kapton substrate surface, and the red curve represents the temperatuer change at the PZT film surface. This is just a single cycle result while the optimized sintering parameters require two cycles. The temperature of the Kapton already increases up to 1850 °C, which could certainly burn the substrate. 2050 °C in the PZT film could also burn the PZT film. Therefore, an optimization for the sintering parameters is required to obtain a fully sintered PZT film throughout the thickness without damage the low temperature substrate.

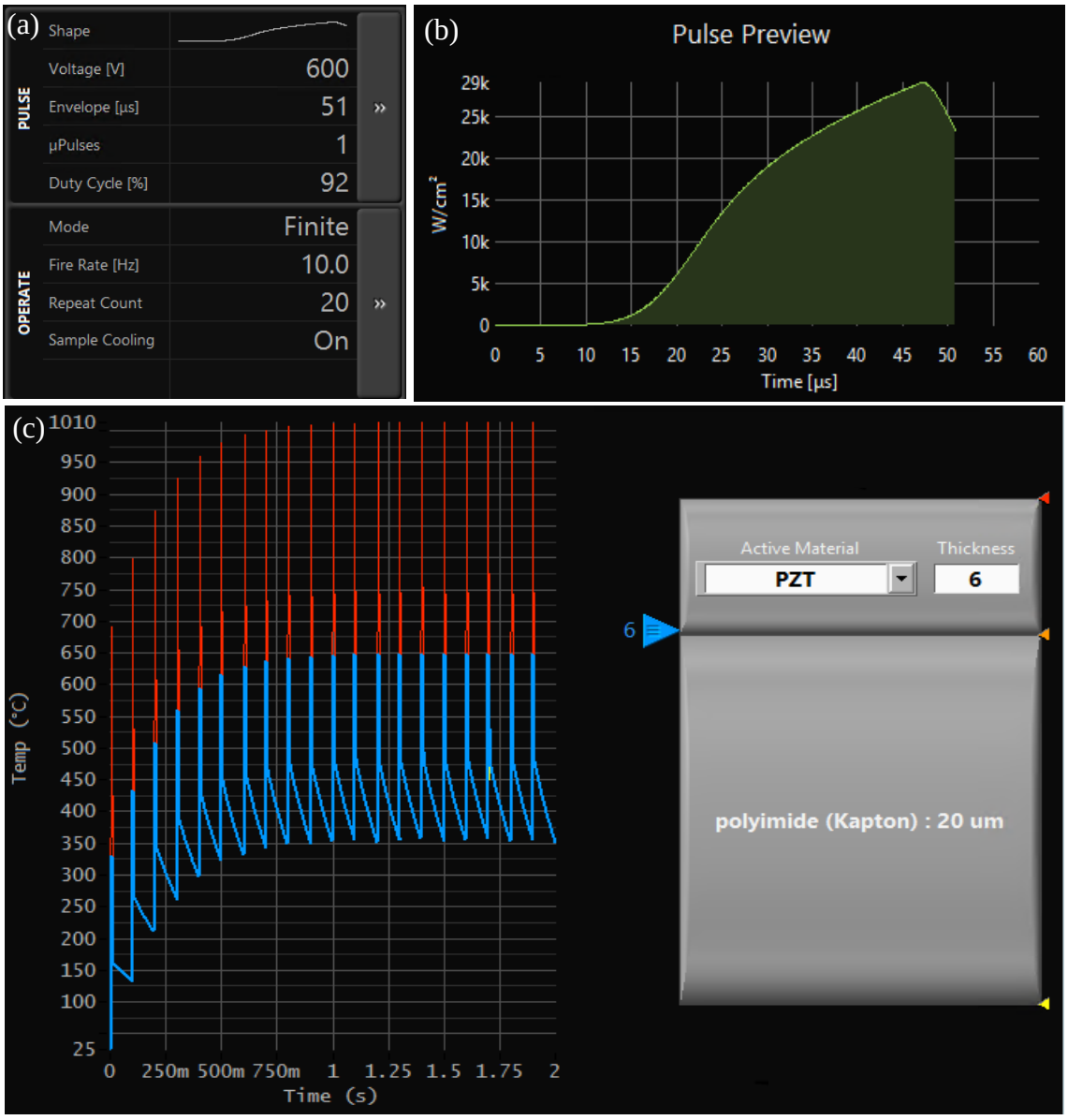

Figure 6-2. A SimPulse simulation on a µPulse mode setting (a) that results in a (b) up to 29k W/cm^2 power density for each pulse. The temperature change (c) in the PZT film and substrate indicates up to 1010 °C temperature can be generated at the film surface to obtain a well sintered PZT film. On the other hand, the substrate temperature is expected as low as 650 °C. This could melt the substrate slightly to enhance the film-substrate adhesion without damage it. This setting could allow that the PZT film directly sintered on the low temperature substrate.

Appendix A Process Description of Aerosol Jet Printer

The aerosol jet printer consists of three major parts: pneumatic atomizer, virtual impactor, and print head.

Atomization is the process of forming an aerosol stream from the ink in the atomization jar. Fig. A-1 illustrates the atomization process. Compresses gas (N_2 in this work) is transited through a tube to the atomization head (i.e. atomizer) with high velocity. Due to the Venturi Principle, the ink is drawn off the reservoir and sucked into the capillary tubing through a small orifice. Subsequently, as the ink travels to the top of the tubing, the high-velocity N_2 gas breaks the ink into small droplets and blown them to the flow. The amount of incoming N_2 gas is controlled by the flow controller, and hence further control the amount of the ink that is to be atomized. The atomized stream then is carried to the virtual impactor. [1]

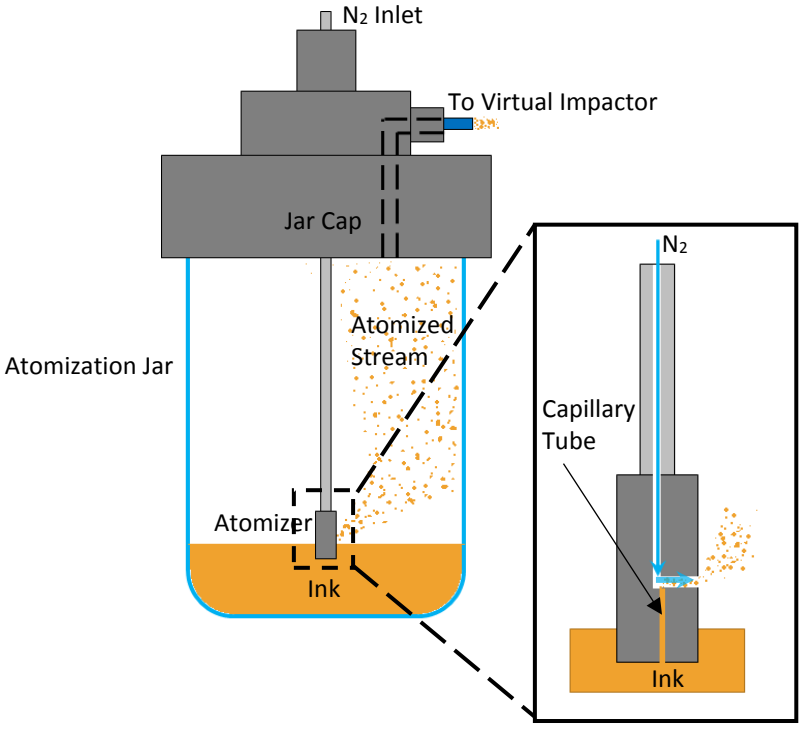

Figure A-1. The section view of the pneumatic atomization system to illustrate the working process of atomization.

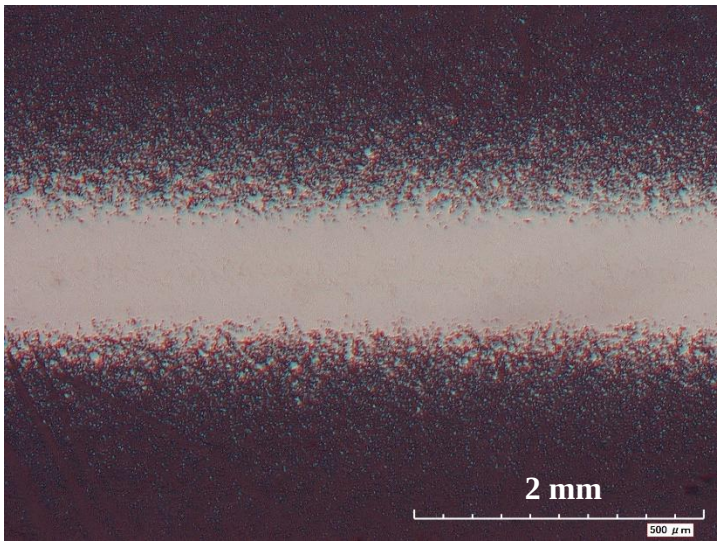

Figure A-2. The aerosol jet printed single PZT line. The over-sprayed splatters negatively affect printing resolution.

The ink stream that exits from the atomization jar contains high quantity of droplets with high flow rate and various droplet sizes. However, firstly, with high speed, the jetted stream would hit the substrate and bounce away to form splatters. Secondly, smaller size droplets, after leaving the print head, are more susceptible to the influence of air resistance and air flow, which would also results in satellite features on the substrate [2]. However, the splattered satellites affect the printed feature size and structure as shown in the Fig. A-2, which is not acceptable for functional printing. Virtual impactor is located after the

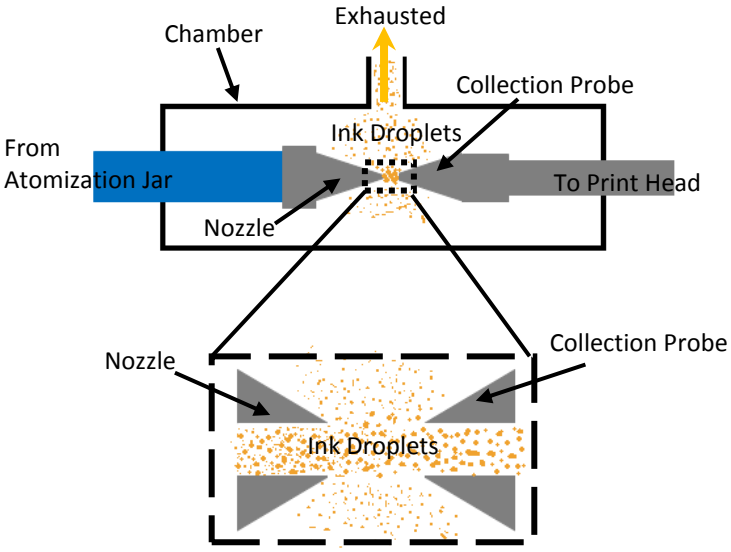

Figure A-3. Working principle of virtual impactor.

atomization jar to lower the stream flow rate and exhaust the smaller droplets (Fig. A-3). The stream from the atomization part arrives the nozzle and penetrates the collection probe. However, the droplets that have low momentum would deviate after leaving the nozzle and enter the chamber due to the extracting flow rate applied at the virtual impactor, which is controlled by the mass flow controller. These droplets are then exhausted from the stream. Provided the droplets are only PZT ink (i.e. same density, ideally), then the larger droplets have higher weight giving rise to higher momentum. Therefore, smaller particles are evacuated as shown in the Fig. A-3. The droplets remained in the collection probe are directed downstream to the print head for jetting out. The flow rate in the collection probe equals the difference between atomization flow rate and virtual impactor flow rate. [3]

The aerosol stream is carried from the virtual impactor to the ceramic deposition nozzle (the diameter of the orifice is typically 150, 200, or 300 μm) through a polypropylene tube with an internal diameter of 1/8 in. The specially designed deposition head is the key of the printing (Fig. A-4). The co-axial sheath gas is forming and surrounding the aerosol stream to avoid its contact to the nozzle tip which may lead to contamination of the nozzle head or clogging. In the meantime, the aerosol stream is also aerodynamically focused by this sheath gas to enhance the printing resolution. A shutter is used in the stream path between the ceramic nozzle and the substrate. It is used to obstruct the aerosol stream printing after leaving the print head for those moments when the printing requires to be stopped. [1]

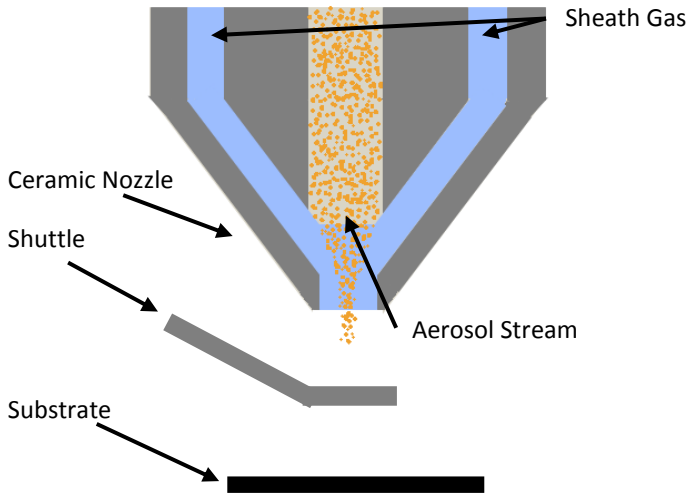

Figure A-4. The sectional view of the ceramic nozzle during printing. The sheath gas is used to aerodynamically focus the aerosol stream to avoid the clog at the nozzle head to negatively affect the printing.

References:

[1] A. Mette, P. L. Richter, M. Horteis, and S. W. Glunz, "Metal aerosol jet printing for solar cell metallization," *Progress in Photovoltaics: Research and Applications*, vol. 15 pp. 621-627, 2007.

[2] Y. Imahashi, and T. Inoue, "Inkjet printing apparatus and printhead driving method," *U.S. Patent No. 7794035*, issued September 14, 2010.

[3] M. J. Renn, B. H. King, M. Essien, and L. J. Hunter, "Apparatuses and method for maskless mesoscale material deposition," *U.S. Patent No. 7045015*, issued May 16, 2006.

Appendix B Elimination of the Pyrochlore Phase for Photonically Sintered PZT

The PZT pyrochlore phase observed in the sintered films is believed to be due to volatilization of PbO during sintering. Therefore, the addition of PbO (Sigma-Aldrich Co. LLC,) was explored to eliminate this secondary phase. Additionally, low concentrations of added PbO have been shown to lower PZT sintering temperature [1, 2]. The films are accordingly expected to have better quality and higher density than those sintered without added PbO. The updated ink composition is shown in Table A1.

Table B-1. Updated PZT ink composition

Material	Weight
PZT	30.0
DI Water	48.6
EG	12.4
DisperBYK-	5.0
PVP	3.0
PbO	1.0

Both SEM images (Fig. B-1) and XRD (Fig. B-2) were used to examine the sintering quality of two sintering approaches (thermal and photonic). The film quality for both sintering approaches has been improved as compared to the prior results of Fig. 8 (b) and (c), with the greatest improvement in secondary phase reduction achieved for the photonically sintered case. The measured densities of the sintered films were 85.2% (thermal sintering) and 84.3% (photonic sintering) of the theoretical APC 855, respectively. As with the prior formulation, the photonically sintered film had less effective fusing and merging of the particles deep within the film as shown in Fig. B-1 (d), due to the temperature gradient from the flash energy through the film thickness. The XRD results show pure crystalline perovskite structure in the photonically sintered films (Fig. B-2 (b)). However, the pyroclore phase was still observed in thermally sintered films (Fig. B-2 (a)).

The elimination of pyrochlore phase in the photonically sintered film is expected to enhance the piezoelectric properties.

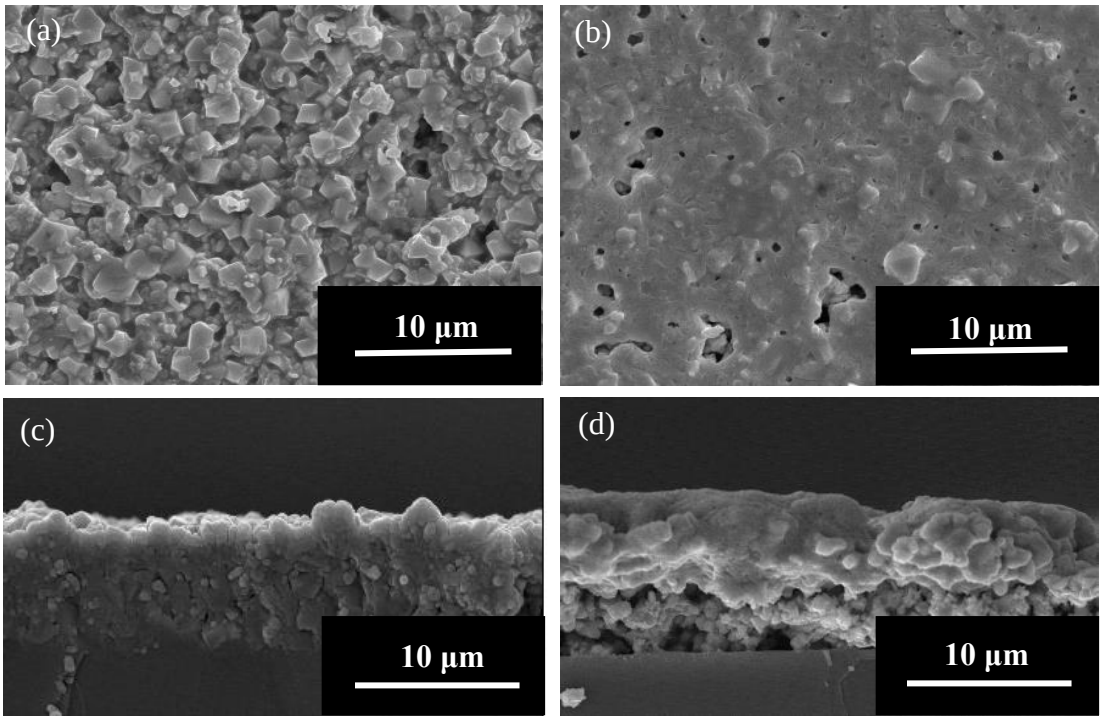

Figure B-2. SEM images of PZT films after thermal sintering (a), and after photonic sintering (b). While the surface density of the photonically sintered film appears higher, overall density through the film was slightly lower than the thermally sintered case. SEM images of (c) and (d) are cross-sectional micrographs of the thermally and photonically sintered films, respectively.

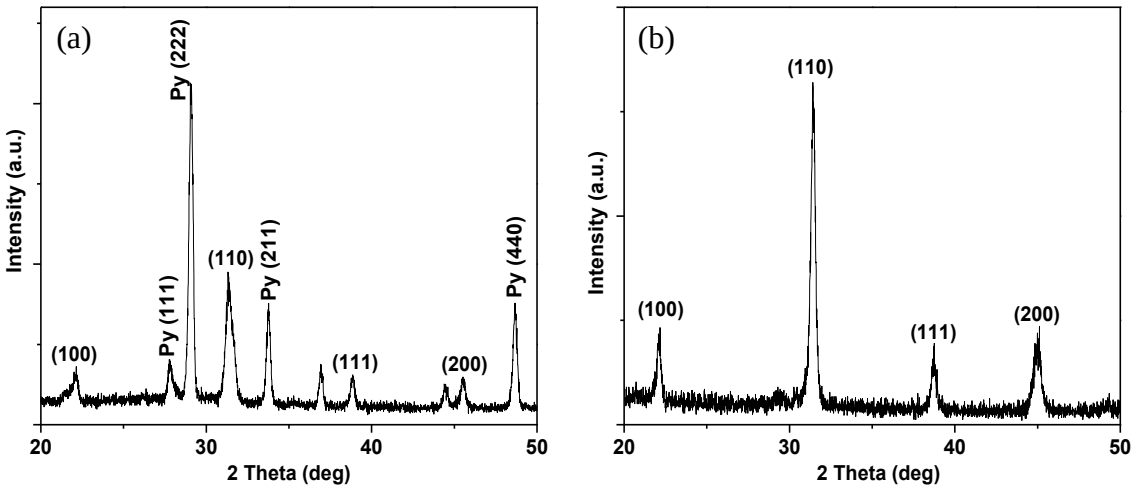

Figure B-1. XRD results for thermally (a) and photonically (b) sintered PZT films. Addition of 1 wt.% PbO to the PZT ink formulation yielded a slight reduction in the pyrochlore phase (marked as "Py") for the thermally sintered film. However, for the photonically sintered case, the pyrochlore phase has been completely eliminated, yielding a pure perovskite phase.

References:

[1] S. A. Bernard, V. K. Balla, S. Bose, and A. Bandyopadhyay, " Direct laser processing of bulk lead zirconate titanate ceramics," *Materials Science and Engineering: B*, vol. 172, pp. 85-88, 2010.

[2] T. Futakuchi, K. Nakano, and M. Adachi, " Low-temperature preparation of lead-based ferroelectric thick films by screen-printing," *Japanese Journal of Applied Physics*, vol. 39, pp. 5548-5551, 2000.

Appendix C Design of Experiment for Fully Sintered PZT Thick Films

In order to optimize the sintering parameters to obtain a fully sintered PZT thick film, a design of experiment (DOE) with 5 variables (voltage, pulse duration, frequency, number of pulses, and number of cycles), 2 levels, and 2 replicates was carried out in Minitab 17. The matrix is shown in the Table C-1. The response was estimated from the qualitative observation of the sintered PZT films with assistant of SEM images. It reflected the sintered quality of the film. 0 represents non-sintered yet, 1 represents either the film was already burned or the energy density resulted from the setting was too high to be processed by the equipment for the safety purpose. The closer to the 0.5 of the response, the better sintered quality obtained in the PZT film. For the equipment, the initial intensity of the xenon flash lamp is controlled through setting the charge voltage of the capacitor banks that will discharge through the xenon lamp during flashing. During the flashing, the capacitors are continuously being charged with a given rate. However, the equipment will stop working while the stored charge voltage is used out in the capacitor banks and the voltage usage rate exceeds the charging rate during the flashing. This limits the number of cycles and pulses. The main effects plots were generated and shown in the Fig. C-1. The ANOVA (analysis of variance) table was shown in the Table C-2. Notice that within the specified range of the factors, frequency had the least impact to the sintering quality due to the high p-value (> 0.05). Among all four significant factors, number of pulses shows the greatest impact. This is because two extreme levels were used for this factor (i.e. 1 and 20). Therefore, significant difference in the response was expected. In addition, by investigating the residual plots (Fig. C-2), the straight-line pattern in the normal probability plot, the random scatter around the horizontal “zero error line” and the constant spread, plus the normally distributed residual frequency plot show that there is no violations in using this ANOVA model. The best response was yielded when using the combination of voltage = 400, duration = 650, frequency = 1, number of pulses = 20, and number of cycles = 3.

However, the response for this combination was 0.55, indicating a slightly overexposure. A further optimization was performed based on this by fine tuning the least important parameters. The final optimized parameters were: voltage = 400, duration = 650, frequency = 2, number of pulses = 20, and number of cycles = 2.

Table C-1. Factor table and experimental response results for photonic sintering parameter optimization.

Std Order	Run Order	Voltage	Duration	Freq.	No. of P	No. of C	Response
20	1	400	650	1	1	3	0.05
24	2	400	650	2	1	3	0.05
45	3	300	400	2	20	1	0.20
41	4	300	400	1	20	1	0.15
14	5	400	400	2	20	1	0.2
36	6	400	650	1	1	1	0.00
27	7	300	650	1	20	3	0.40
57	8	300	400	1	20	3	0.25
26	9	400	400	1	20	3	0.30
34	10	400	400	1	1	1	0.00
39	11	300	650	2	1	1	0.00
29	12	300	400	2	20	3	0.20
15	13	300	650	2	20	1	0.15
33	14	300	400	1	1	1	0.00
9	15	300	400	1	20	1	0.10
23	16	300	650	2	1	3	0.05
1	17	300	400	1	1	1	0.00
22	18	400	400	2	1	3	0.05
3	19	300	650	1	1	1	0.00
58	20	400	400	1	20	3	0.35
56	21	400	650	2	1	3	0.05
50	22	400	400	1	1	3	0.00
13	23	300	400	2	20	1	0.10
55	24	300	650	2	1	3	0.00
28	25	400	650	1	20	3	0.55
11	26	300	650	1	20	1	0.15
8	27	400	650	2	1	1	0.00
42	28	400	400	1	20	1	0.05
32	29	400	650	2	20	3	0.70
18	30	400	400	1	1	3	0.00
35	31	300	650	1	1	1	0.00
30	32	400	400	2	20	3	0.30

Std Order	Run Order	Voltage	Duration	Freq.	No. of P	No. of C	Response
5	33	300	400	2	1	1	0.00
12	34	400	650	1	20	1	0.30
25	35	300	400	1	20	3	0.15
53	36	300	400	2	1	3	0.00
61	37	300	400	2	20	3	0.20
7	38	300	650	2	1	1	0.00
19	39	300	650	1	1	3	0.05
16	40	400	650	2	20	1	0.40
44	41	400	650	1	20	1	0.30
59	42	300	650	1	20	3	0.30
17	43	300	400	1	1	3	0.00
60	44	400	650	1	20	3	0.60
10	45	400	400	1	20	1	0.25
37	46	300	400	2	1	1	0.00
38	47	400	400	2	1	1	0.00
64	48	400	650	2	20	3	0.80
47	49	300	650	2	20	1	0.20
49	50	300	400	1	1	3	0.00
46	51	400	400	2	20	1	0.10
62	52	400	400	2	20	3	0.15
63	53	300	650	2	20	3	0.40
6	54	400	400	2	1	1	0.00
51	55	300	650	1	1	3	0.05
40	56	400	650	2	1	1	0.05
54	57	400	400	2	1	3	0.00
43	58	300	650	1	20	1	0.10
21	59	300	400	2	1	3	0.00
48	60	400	650	2	20	1	0.40
4	61	400	650	1	1	1	0.00
2	62	400	400	1	1	1	0.00
31	63	300	650	2	20	3	0.35
52	64	400	650	1	1	3	0.05

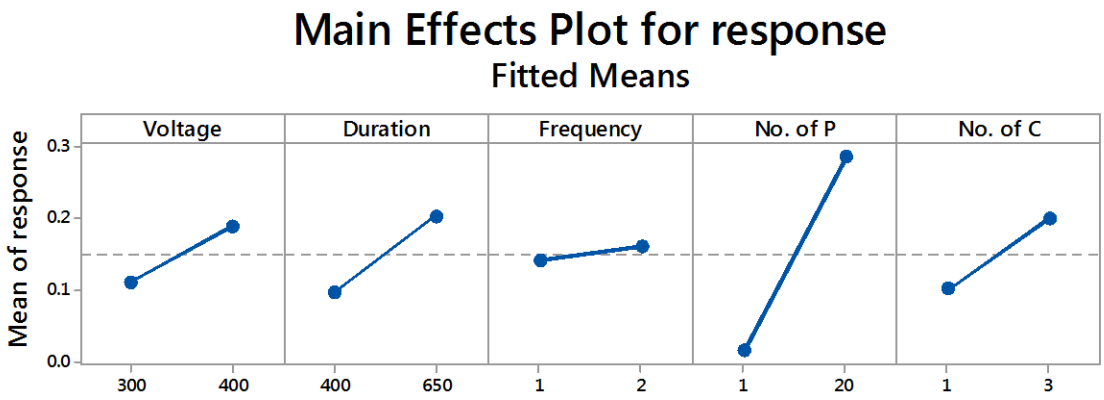

Figure C-1. The main effects plots of the response. The frequency shows insignificant impact to the sintering quality. Number of the pulses shows the greatest importance to the sintering. Practically, 20 pulses yielded better sintering quality.

Table C-2. ANOVA (analysis of variance) table for all five factors and two-factor interactions.

Source	DF	Adj SS	Adj MS	F- Value	P-Value
Model	15	8.60809	0.57387	20.67	0.000
Linear	5	7.21332	1.44266	51.97	0.000
Voltage	1	0.13141	0.13141	31.08	0.000
Duration	1	0.14062	0.14062	33.26	0.000
Frequency	1	0.00250	0.00250	0.59	0.446
No. of P	1	1.07641	1.07641	254.56	0.000
No. of C	1	0.15016	0.15016	35.51	0.000
2-Way	10	1.39477	0.13948	5.02	0.000
Voltage*Duration	1	0.06891	0.06891	16.30	0.000
Voltage*Frequency	1	0.00391	0.00391	0.92	0.341
Voltage*No. of P	1	0.10562	0.10562	24.98	0.000
Voltage*No. of C	1	0.01000	0.01000	2.36	0.131
Duration*Frequency	1	0.00563	0.00563	1.33	0.254
Duration*No. of P	1	0.08266	0.08266	19.55	0.000
Duration*No. of C	1	0.03516	0.03516	8.31	0.006
Frequency*No. of P	1	0.00141	0.00141	0.33	0.567
Frequency*No. of C	1	0.00016	0.00016	0.04	0.848
No. of P*No. of C	1	0.09000	0.09000	21.28	0.000
Error	48	0.20297	0.00423		
Total	63	2.10750			
S:	R-sq:	R-sq (adj):	R-sq (pred):		
0.0650270	90.37%	87.36%	82.88%		

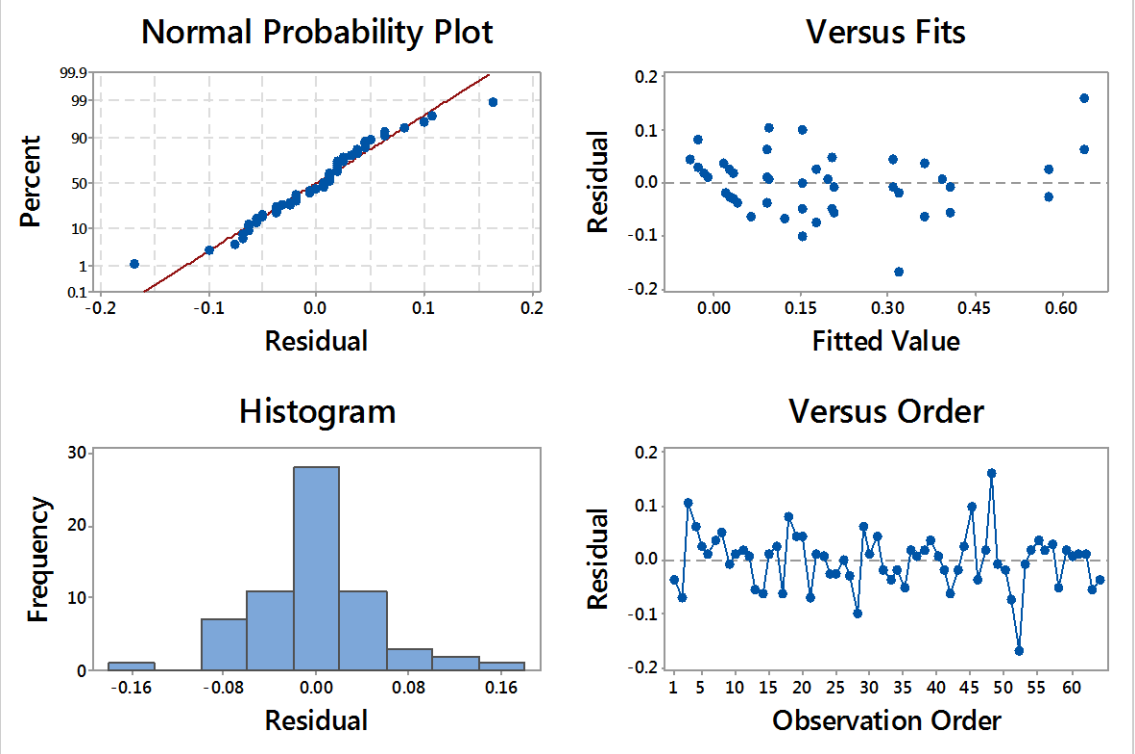

Figure C-2. Residual plots for response. The straight-line pattern in the normal probability plot, the random scatter around the horizontal "zero error line" and the constant spread, plus the normally distributed residual frequency plot show that there is no violations in using this ANOVA model.

Appendix D Design of Experiment for Photonic Sintering of PZT Thick Films with ITO Glass

In order to optimize the sintering parameters to obtain a fully sintered PZT thick film without damaging the ITO glass, a design of experiment (DOE) with 3 variables (voltage, pulse duration, and number of cycles), 2 levels, and 2 replicates was carried out in Minitab 17. According to aforementioned DOE result, frequency was the most insignificant factor for the sintering quality. Therefore, in this DOE, frequency was not considered as a variable and fixed the value to 2 Hz. 20 number of pulses gave the best sintering quality based on the empirical analysis. Therefore, for all DOE experiments in this section, the number of pulses was fixed to 20. The factor and level matrix is shown in the Table D-1. The response was estimated from the qualitative observation of the sintered PZT films with assistant of SEM images. The main effects plots were generated and shown in the Fig. D-1. The ANOVA table was shown in the Table D-2. It is indicated that within the specified range of the factors, voltage and duration had the greatest impact to the sintering quality, as well as the interaction between these two factors, due to the large slope in the Fig C-1 and low p-value (< 0.05) in the Table D-2. Although the residual frequency plot shown in the Fig. D-3 reveals a skewed normal distribution that is most likely due to the same response for all of the voltage = 600 V and duration = 500 μs variable combinations, high R-square (99.43 %) shown in the Table D-2 still indicates a good ANOVA model that is reliable. The best response was obtained when using the combination of voltage = 600, duration =130, frequency = 2, number of pulses = 20, and number of cycles = 2. However, the response for this combination was 0.45, indicating a slightly underexposure. A further optimization was performed based on this by fine tuning the least important parameters. The final optimized parameters were: voltage = 600, duration = 130, frequency = 2, number of pulses = 23, and number of cycles = 2.

Table D-1. Factor table and experimental response results for photonic sintering parameter optimization.

Std Order	Run Order	Voltage	Duration	No of C	Response
9	1	400	130	1	0.10
4	2	600	500	1	1.00*
6	3	600	130	2	0.45
1	4	400	130	1	0.15
5	5	400	130	2	0.15
2	6	600	130	1	0.30
3	7	400	500	1	0.25
14	8	600	130	2	0.45
15	9	400	500	2	0.40
11	10	400	500	1	0.35
12	11	600	500	1	1.00*
10	12	600	130	1	0.35
16	13	600	500	2	1.00*
8	14	600	500	2	1.00*
13	15	400	130	2	0.20
7	16	400	500	2	0.35

* The applied energy was too high to be allowed in the photonic sintering system.

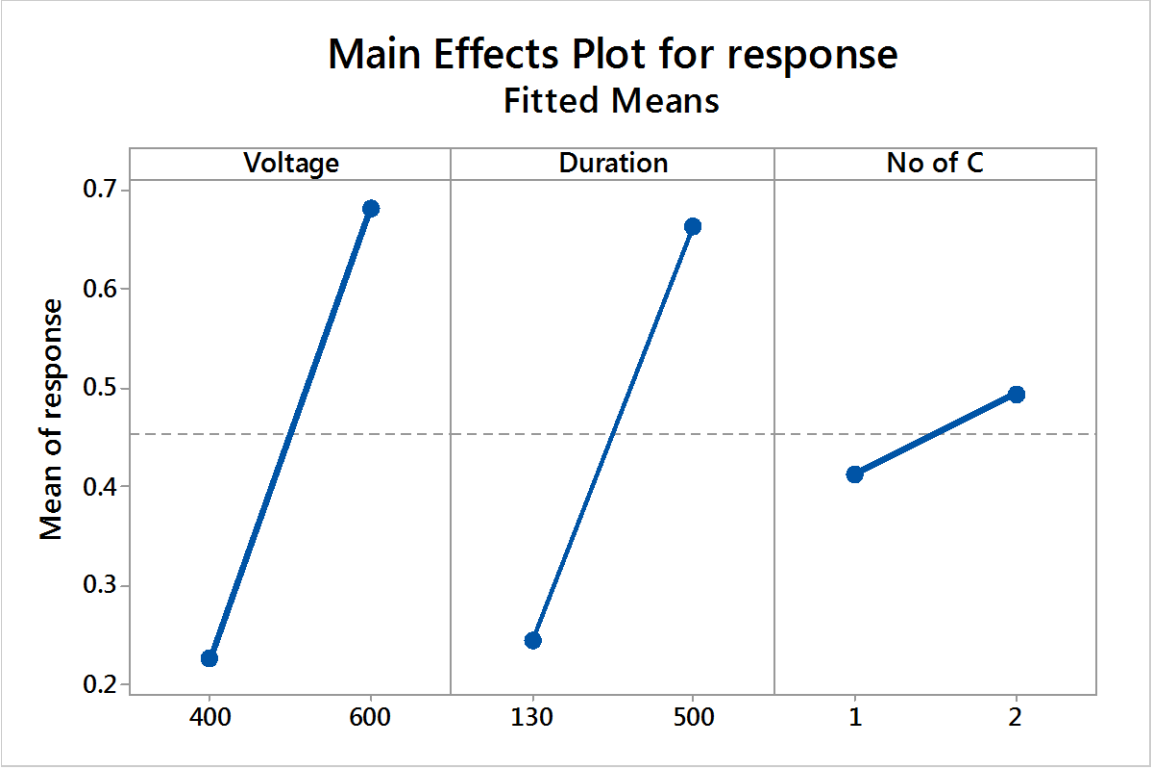

Figure D-1. The main effects plots of the response. The voltage and duration show significant impact to the sintering quality. Number of cycles was not as significant as voltage and duration.

Table D-2. ANOVA table for all three factors and two-factor interactions.

Source	DF	Adj SS	Adj MS	F-Value	P-Value
Model	6	1.75719	0.292865	259.52	0.000
Linear	3	1.56047	0.520156	460.94	0.000
Voltage	1	0.83266	0.832656	737.86	0.000
Duration	1	0.70141	0.701406	621.55	0.000
No. of C	1	0.02641	0.026406	23.40	0.001
2-Way	3	0.19672	0.065573	58.11	0.000
Voltage*Duration	1	0.19141	0.191406	169.62	0.000
Voltage*No. of C	1	0.00141	0.001406	1.25	0.293
Duration*No of C	1	0.00391	0.003906	3.46	0.096
Error	9	0.01016	0.001128		
Total	15	1.76734			
S: 0.0335927	R-Sq: 99.43%	R-sq (adj): 99.04%	R-sq (pred): 98.18%		

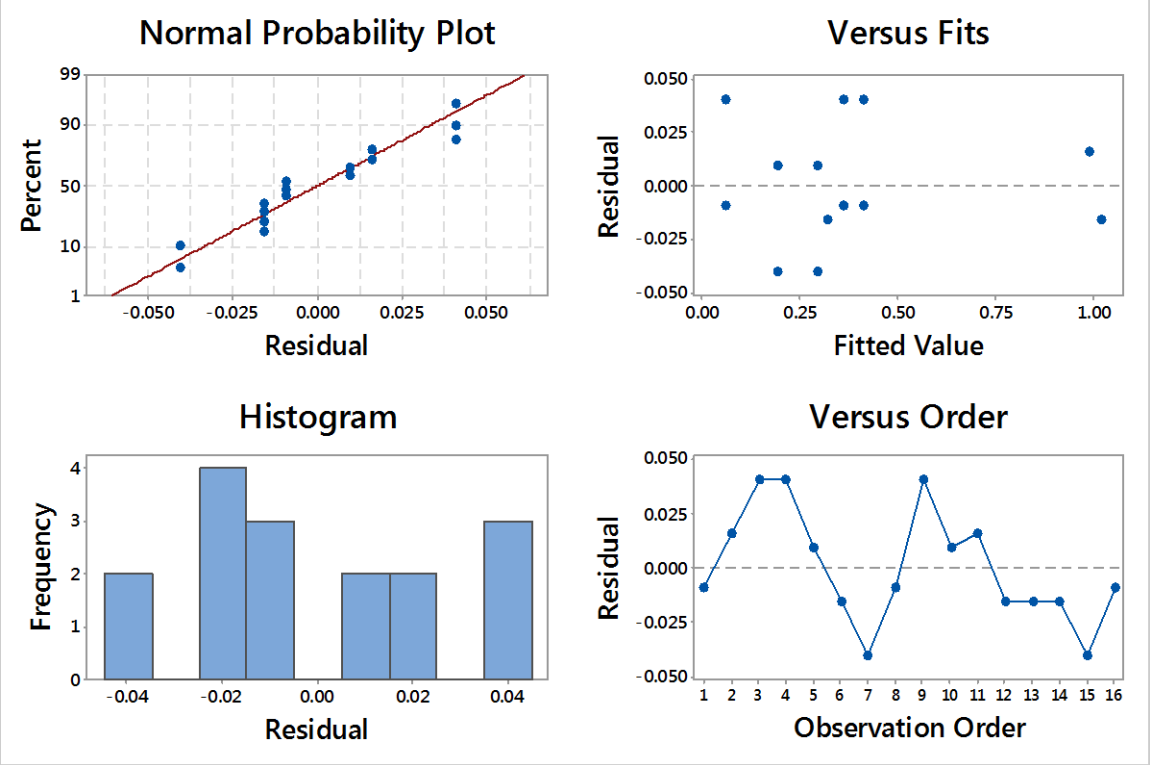

Figure D-2. Residual plots for response. Although the residual frequency histogram plot reveals a skewed normal distribution that is most likely due to the same response for all of the voltage = 600 V and duration = 500 µs variable combinations, high R-square (99.43 %) shown in the Table C-2 still indicates a good ANOVA model that is reliable.